

INCOHERENT AND COHERENT SCATTER RADAR
STUDIES OF THE EQUATORIAL *F* REGION

A Dissertation

Presented to the Faculty of the Graduate School

of Cornell University

in Partial Fulfillment of the Requirements for the Degree of

Doctor of Philosophy

by

Fabiano da Silveira Rodrigues

May 2008

© 2008 Fabiano da Silveira Rodrigues

ALL RIGHTS RESERVED

INCOHERENT AND COHERENT SCATTER RADAR STUDIES OF THE
EQUATORIAL F REGION

Fabiano da Silveira Rodrigues, Ph.D.

Cornell University 2008

Recent advances in the incoherent scatter (IS) theory for small ($< 6^\circ$) aspect angles motivated a reinvestigation of the IS radar cross section (RCS) calculation. A precise RCS is necessary to correct power profiles so as to properly represent the height variation of the ionospheric electron density. Improvements in the representation of density profiles by corrected power profiles were obtained with a RCS calculation that takes into account magnetic field and electron Coulomb collision effects. This improvement was confirmed by a comparison with density profiles measured simultaneously using the Double-Pulse/Faraday rotation radar mode at Jicamarca. This simple but important result solves the long-standing question of the proper RCS to be used at Jicamarca to correct power profiles.

For the first time since the early IS observations at Jicamarca in the 1960's, the proton gyroresonance predicted by IS theory was detected, and temperatures and the H^+ fraction were estimated from the measurements with an automated least-squares procedure. These observations show that, despite the pulse-to-pulse clutter, coherent echoes from spread F , reduced transmitter power, and increased satellite clutter compared to the earlier measurements, the proton gyroresonance can still be detected with reasonable confidence levels. On the other hand, the measurements also indicate the non-viability of the use of gyroresonance measurements as an operational/continuous radar technique for studies

of the topside equatorial ionosphere.

New in-beam radar imaging observations of bottom-type layers were made with a small coherent backscatter radar in Brazil. The observations have larger angular coverage than is currently possible at Jicamarca. The results are in agreement with previous measurements made with Jicamarca and ALTAIR radars and indicate that bottom-type layers can be organized in clusters of scatterers that are horizontally spaced. These clusters are associated with decakilometric plasma waves generated by a shear instability that was recently proposed. The waves modulate the bottomtype layers by having phases that are alternately unstable and stable to wind-driven gradient drift instabilities. The observations also captured the development of a radar plume over the region where the clusters were located. These observations serve as additional evidence of a possible connection between the large-scale waves and the triggering of spread F and suggest that the detection of bottom-type clusters can serve as a helpful diagnostic for spread F forecasts.

BIOGRAPHICAL SKETCH

Fabiano da Silveira Rodrigues was born and raised in the Brazilian Pampas. In 2001, Fabiano obtained his B.Sc. Degree in Electrical Engineering from *Universidade Federal de Santa Maria* (UFSM) in Brazil. In 2003, he received a M.Sc. Degree from the Brazilian National Institute for Space Research (*Instituto Nacional de Pesquisas Espaciais - INPE*). During the M.Sc. Program in INPE, Fabiano worked with GPS observations of equatorial F region irregularities. After finishing his M.Sc. and before coming to Cornell to start his Ph.D. studies, Fabiano worked as a Research Associate at the University of Nottingham in the UK. In Nottingham, he investigated the effects of ionospheric scintillations in satellite-based positioning and played “football”.

Esta dissertação é dedicada à memória do meu pai:

Danir S. S. Rodrigues (1941-2006)

ACKNOWLEDGEMENTS

I would like to especially thank the Chair of my Special Committee, Dr. Hysell for his guidance and exemplary professionalism. I would like to thank also the other two members of my Special Committee, Dr. Kelley and Dr. Cordes. I had the opportunity of taking courses taught by Dr. Kelley and appreciate his enthusiasm for the physics of the ionosphere. I also took courses taught by Dr. Cordes, who introduced me to various techniques for radio observations and data mining in Astronomy.

I would like to thank valuable discussions with and suggestions from Dr. Farley and Dr. Swartz. Thanks to Dr. Woodman and Dr. Chau for their help with the setup of experiments at Jicamarca and valuable discussions during my visit to Jicamarca Radio Observatory. The help from Jicamarca's engineering staff is also appreciated. The Jicamarca Radio Observatory is a facility of the Instituto Geofísico del Perú and is operated with support from the NSF Cooperative Agreement ATM-0432565 through Cornell University. Some of the experiments described in this dissertation were performed with partial support from Jicamarca's visiting program.

Thanks to Dr. de Paula, from INPE in Brazil. He kindly provided the coherent scatter radar data used in this dissertation. Also, I would like to thank Acácio Cunha Neto for continuous operation of the São Luís radar and Lázaro Camargo for pre-processing of interferometric radar data. The São Luís radar was partially supported by FAPESP Processes 99/00026-0 and 04/01065-0.

Thanks to Mike Nicolls, now at SRI International. Mike has been a great friend and colleague since we first met in Grad School. We went to Peru together where we ran a number of experiments at Jicamarca, including the observations of the ion gyroresonance discussed in this dissertation.

Thanks to Leandro Rêgo. Leandro is a fellow Brazilian and was my roommate during my first two years in Ithaca. He was a great source of support and encouragement during my first years at Cornell. I cannot forget to thank my friends in the Space Plasma Physics (SPP) Group and in the Luso-Brazilian Student Association (LUBRASA). My time at Cornell would not have been so enjoyable without them.

Finally, I would like to thank my wonderful wife, Danieli Rodrigues. Her love and support made everything easier.

TABLE OF CONTENTS

Biographical Sketch	iii
Dedication	iv
Acknowledgements	v
Table of Contents	vii
List of Tables	x
List of Figures	xi
1 Introduction	1
1.1 Motivation for the study of the ionosphere	1
1.2 Motivation for the IS radar studies in this dissertation	2
1.3 Motivation for the coherent scatter radar studies in this dissertation	4
1.4 Organization of this dissertation	5
2 The Earth's ionosphere	6
2.1 Introduction	6
2.2 The Earth's atmosphere	7
2.2.1 The lower atmosphere	8
2.2.2 Middle atmosphere	8
2.2.3 Upper atmosphere	9
2.2.4 Atmospheric composition	9
2.3 The ionosphere	10
2.3.1 Formation	10
2.3.2 The ionospheric profile	15
2.3.3 Temperatures	23
2.3.4 Ion composition	24
2.4 Dynamics of the ionospheric plasma	29
2.4.1 Magnetization of the ionospheric plasma	29
2.4.2 Velocity of the ionized species	32
2.4.3 Current density in the ionospheric plasma	35
2.4.4 Generation of electric fields	36
2.4.5 Atmospheric winds and tides	38
2.5 The low-latitude F region	39
2.5.1 Zonal plasma drifts	40
2.5.2 Vertical shear in the zonal plasma flow	41
2.5.3 Vertical plasma drifts	43
2.5.4 Pre-reversal enhancement of the zonal electric field	43
2.5.5 The equatorial fountain effect	45
2.5.6 Equatorial spread F	47

3	Radar remote sensing of the ionosphere	49
3.1	Introduction	49
3.2	Scattering of radio waves in the ionosphere	50
3.2.1	Scattering by a single electron	51
3.2.2	Scattering from a distribution of electrons	52
3.3	Signal statistics	54
3.4	Incoherent scatter of radio waves	57
3.4.1	The spectrum of thermal density fluctuations	58
3.4.2	Short and long wavelength regimes	60
3.4.3	Long wavelength regime: The ion and plasma lines	60
3.4.4	Estimation of plasma parameters	61
3.5	Coherent scatter of radio waves	63
3.6	Propagation of radio waves in the ionosphere	65
3.7	Faraday rotation	68
3.8	Instrumentation	71
3.8.1	Jicamarca radar	71
3.8.2	São Luís radar	72
4	On the proper radar cross section for Jicamarca oblique IS radar observations	74
4.1	Introduction	74
4.2	Magnetic field effects in the IS spectrum	75
4.3	Discrepancies in the IS radar observations at Jicamarca	76
4.4	Electron Coulomb collision effects in the IS spectrum	76
4.5	The calculation of the IS spectrum including electron Coulomb collisions	77
4.5.1	The Gordeyev integral for a collisional and magnetized plasma	78
4.5.2	Illustration of electron Coulomb collision effects	79
4.6	Standard IS radar pointing positions at Jicamarca	80
4.7	IS radar cross section	83
4.7.1	The efficiency factor η	84
4.8	Electron Coulomb collision effects in the IS RCS	86
4.9	Experimental setup	88
4.10	Validating RCS calculations and power corrections	91
4.11	On the estimation of T_e/T_i from power-density measurements	93
4.12	An approximate formula for the efficiency factor of a magnetized plasma	94
4.13	Summary	96
5	New observations of the proton gyroresonance at Jicamarca	98
5.1	Introduction	98
5.2	Topside observations at Jicamarca	99
5.3	The ion gyroresonance	100

5.4	Collisional effects on the gyroresonance	102
5.4.1	Gordeyev integral for a magnetized collisional plasma . .	103
5.4.2	Ion Coulomb collision frequency	104
5.4.3	Electron Coulomb collision frequency	105
5.5	The collisional IS spectrum	106
5.6	The proton gyroresonance	107
5.7	Experiment setup	110
5.7.1	ACF estimator	113
5.8	Experiment results	116
5.9	Temperature and composition estimates	117
5.10	Summary	120
6	Coherent backscatter radar imaging observations of large-scale waves at the onset of equatorial spread F	122
6.1	Introduction	122
6.1.1	Development of equatorial spread F	123
6.1.2	Local linear growth rate	124
6.1.3	Flux-tube integrated linear growth rate	126
6.1.4	Triggering mechanism	128
6.2	Experimental setup	130
6.3	Interferometric radar imaging	131
6.3.1	Inversion algorithm	133
6.3.2	In-beam radar images	136
6.4	Observations of October 25, 2005	137
6.5	Bottom-type layers	140
6.6	Vertical shear of the zonal plasma flow	145
6.7	Structures in the bottom-type layer	146
6.8	Previous observations	147
6.9	On the origin of the bottom-type clusters	148
6.10	Summary	151
7	Conclusions and future work	153
7.1	IS RCS at small aspect angles	153
7.2	The ion gyroresonance	154
7.3	Large-scale waves at the onset of ESF	155
7.4	Future work	157
7.4.1	Neutral temperatures and densities	157
7.4.2	Bottom-type layers	158
7.4.3	Vertical drifts	159

LIST OF TABLES

5.1	Values of C_{sj} for different ion mixtures (<i>Woodman, 1967</i>).	105
6.1	Radar parameters for equatorial spread F imaging observations. Jicamarca parameters are also shown for comparison purposes (<i>Hysell et al., 2004a</i>).	133

LIST OF FIGURES

1.1	Example of density fluctuations and ionospheric scintillations observed in the low latitude ionosphere with a dual-frequency GPS receiver. Panel (a) shows the relative total electron content (TEC) estimated from the travel time difference between two signals with different frequencies. The signals were transmitted by a GPS satellite and received by a ground receiver. Panel (b) shows the fluctuations in the signal amplitude associated with fluctuations in the TEC. Panel (c) shows the elevation angle of the GPS satellite from which the signals were transmitted.	3
2.1	(a) Height variation of neutral temperature. (b) Vertical distribution of neutral components. (c) Vertical variation of the mean molecular mass. These profiles were generated using results from the Mass Spectrometer - Incoherent Scatter (MSIS) model of the atmosphere (<i>Picone et al., 2002</i>).	7
2.2	Solar radiation and photoionization of the atmosphere.	12
2.3	Normalized production rate $P_{\lambda}/P_{\lambda 0}$ for different values of zenith angle.	14
2.4	(a) Typical mid-latitude ionospheric density profile. (b) Expanded view of the <i>E</i> and <i>F</i> regions.	16
2.5	Normalized electron density versus reduced height $\zeta = \frac{h-h_0}{H}$. The solid line is the α -Chapman profile (Eq. 2.19), and the dashed line shows the density profile described by Eq. 2.21.	22
2.6	Daytime profiles obtained from the International Reference Ionosphere - IRI empirical model (<i>Bilitza, 2001</i>) for a mid-latitude ionosphere: (a) electron density, (b) temperatures and (c) ion composition.	25
2.7	He^+ fraction (%) measured during an orbital cycle by the ROCSAT-1 satellite on March 13, 2001 between 15:47 UT and 17:30 UT. Dashed lines indicate solar zenith angles calculated for 16:37 UT.	28
2.8	Illustration of Earth's magnetic field.	30
2.9	IGRF values of magnetic inclination for 2005. The magnetic inclination is the angle between the magnetic field vector and a local horizontal vector.	32
2.10	Typical conductivity profiles for an equatorial location during sunset hours in the equinox and high solar flux conditions. . . .	37
2.11	Quiet-time zonal plasma drifts measured at Jicamarca for different seasons and solar flux conditions. After <i>Fejer et al. (2005)</i> . Reproduced by permission of American Geophysical Union. . .	42

2.12	Averages of vertical plasma drifts measured by the AE-E satellite for different seasons and longitude sectors. After <i>Fejer et al.</i> (1995). Reproduced by permission of American Geophysical Union.	44
2.13	Global map of the maximum density of the ionospheric F_2 region (NmF2). Values of NmF2 were calculated using the International Reference Ionosphere (IRI) model.	46
3.1	Scattering geometry for a bistatic radar. The location \mathbf{r}_p of a particular electron is indicated.	55
3.2	Ion line computed for different values of electron-to-ion temperature ratio (top panel) and different ion compositions (single ion species considered in all cases).	62
3.3	Examples of IS spectra for short and long wavelength regimes. The calculations were made for an UHF radar. The plasma line is the narrow spectral line around 2 MHz.	63
3.4	(a) Example of an equatorial daytime ionospheric profile from the IRI model, (b) magnetic field intensity and (c) the angle between the wavevector \mathbf{k} and the magnetic field calculated for Jicamarca's on-axis position (for 2005), and (d) the corresponding ratio R as defined in Eq. 3.29.	68
3.5	Location of the two radar facilities where observations presented in this dissertation were made. Contours of magnetic inclination are also shown (IGRF values for 2005). Incoherent scatter observations were made with the Jicamarca radar, while coherent scatter observations were made with the São Luís radar.	72
4.1	Sketch illustrating how the electron motion affects the phase of the radar signal.	77
4.2	Incoherent scatter spectra calculated for different aspect angles (α) for an unmagnetized plasma, a collisionless magnetized plasma, and magnetized plasma with electron Coulomb collision effects included (O^+ plasma, $T_e = T_i = 1000$ K and $n_e = 10^{12}$ m^{-3}).	81
4.3	Same as Fig. 4.2 but for $n_e = 5 \times 10^{10}$ m^{-3}	82
4.4	Height variation of the aspect angle (α) for the three standard pointing positions at Jicamarca. Calculations used geomagnetic field values from the IGRF model (April 2006).	83
4.5	Results of numerical calculation of the IS RCS (Eq. 4.7) for an unmagnetized plasma and comparison with the approximation $\sigma_T \approx \frac{4\pi r_e^2 N_e}{1+T_e/T_i}$ found by <i>Farley</i> (1966b). The results are for Jicamarca frequency (50 MHz), an O^+ plasma, $T_i = 1000$ K and $N_e = 10^{12}$ m^{-3}	87

4.6	Efficiency factors for different aspect angles. Results are for a magnetized plasma with and without electron Coulomb collisions effects included and for a unmagnetized plasma (O^+ plasma with $T_i = 1000^\circ$ and $N_e = 10^{12} m^{-3}$).	88
4.7	Example of (a) backscattered power and Faraday rotation measurements, (b) electron and ion temperature measurements, and (c) efficiency factor calculated using known values (from IGRF) of aspect angles and measured values of n_e , T_e and T_i	90
4.8	Examples of power (dashed line), corrected power (solid line), and Faraday rotation (thick solid line) for three different times on April 20, 2006. Predicted efficiency factors used in the power correction are also shown in the panels on the right.	92
4.9	Efficiency factors for different aspect angles. Dashed lines show $\eta = (1/(1 + T_e/T_i))$. Square marks show the values of the η computed with full IS theory including electron Coulomb collisions. The solid line shows the results of the proposed new expression.	95
5.1	IS spectrum calculated for a magnetized collisionless plasma O^+ (top panel) and the corresponding IS ACF (bottom panel). The dashed lines indicate multiples of the O^+ gyroperiod (T_{O^+}) for the magnetic field used in the calculation (20,000 nT).	101
5.2	Examples of incoherent scatter spectra calculated for a collisional (thick line) and collisionless (thin line) O^+ plasma and for different values of electron density.	107
5.3	Same as Fig. 5.2 but for a H^+ plasma.	108
5.4	Aspect angle effects: First gyroresonance peak in the IS ACF calculated for a collisionless H^+ plasma at different aspect angles ($n_e = 10^{12} m^{-3}$, $T_e = T_i = 1000$ K, $ \mathbf{B} = 20,000$ nT). The vertical dashed lines indicate the proton gyrorotation period.	110
5.5	Composition effects: First gyroresonance peak in the IS ACF calculated for a collisionless plasma with different composition fractions ($\alpha = 1.5^\circ$, $n_e = 10^{11} m^{-3}$, $T_e = T_i = 1000$ K, $ \mathbf{B} = 20,000$ nT). The vertical dashed lines indicate the proton gyrorotation period.	111
5.6	Density effects: First gyroresonance peak in the IS ACF calculated for a H^+ plasma with with different density values ($\alpha = 1.5^\circ$, $T_e = T_i = 1000$ K, $ \mathbf{B} = 20,000$ nT). The vertical dashed lines indicate the proton gyrorotation period.	112
5.7	Temperature effects: First gyroresonance peak in the IS ACF calculated for a H^+ plasma at different temperatures ($T = T_e = T_i$, $\alpha = 1.5^\circ$, $n_e = 10^{11} m^{-3}$, $ \mathbf{B} = 20,000$ nT). The vertical dashed lines indicate the proton gyrorotation period.	113

5.8	Geomagnetic field intensity, gyroperiod and aspect angle as a function of range along the radar line-of-sight for the pointing position used in the gyroresonance experiment	114
5.9	Range-time diagram for the single-polarization double-pulse experiment used for the gyroresonance observations.	114
5.10	(a) Incoherent scatter autocorrelation functions measured on October 9, 2006 (1940-2020 LT). The solid diagonal line shows the values of the gyroperiod based on IGRF. The vertical spacing between dashed lines correspond to a correlation of 0.5. (b) Same except for 2020-2100 LT.	118
5.11	(a) Examples of the least-squares best fits (solid lines) for a set of gyroresonance measurements (square marks) on October 9 2006, 1940-2100 LT (see scale on the top right side of the panel). Inverted H^+ fractions and temperatures are shown in panels (b) and (c), respectively.	120
6.1	Amplitude scintillations measured with GPS-based scintillation monitors in Brazil. The S_4 is a widely used scintillation index defined as the power variance normalized by the average power. Scintillation is particularly strong near the Appleton Anomaly region where F region densities are higher. GPS signal tracking can be lost by the receiver during strong scintillation events. . .	123
6.2	Illustration of density perturbations in the bottomside F region and the generation of polarization electric fields causing the convection of low density plasma upward.	125
6.3	Diagram showing the disposition of the four (A, B, C and D) antenna modules. The modules are aligned in the magnetic east-west direction.	132
6.4	Antenna arrays at the São Luís radar in Brazil.	132
6.5	Range-Time-Intensity (RTI) map for the São Luís (30 MHz) radar observations made on October 25, 2005 (UT \approx LT+3)	140
6.6	Sequence of in-beam radar images showing a bottom-type layer. The images shows that the layer is created to the East of the radar location and moves in westward direction entering the radar field-of-view.	141
6.7	Sequence of in-beam radar images showing two clusters of scattering waves within the radar field-of-view.	142
6.8	Sequence of in-beam radar images showing the development of a radar plume.	143
6.9	Diagram illustrating electron density perturbations caused by the large-scale waves and the geometry for the generation of the irregularity clusters. Regions where horizontal wind (U) is large in the plasma rest frame and parallel to a component of the density gradient (∇n) are gradient drift unstable.	147

6.10 Altair radar scans prior to, during, and after a rocket launch on August 15, 2004 during the EQUIS II observation campaign. The white arc is the instrumented rocket trajectory. The rightmost panels depict electron density profiles at zenith. Times shown are UT (LT \approx UT + 11). After (*Hysell et al.*, 2005b). Reproduced by permission of American Geophysical Union. 149

CHAPTER 1

INTRODUCTION

Radio waves are weakly scattered by thermal fluctuations in the quasi-equilibrium ionospheric plasma. Coherent scatter echoes, meanwhile, are caused by non-thermal electron density fluctuations generated by plasma instabilities and are much stronger than incoherent scatter (IS) echoes. The spectra of IS echoes provide information about parameters of the background plasma such as electron density, temperatures, and ion composition. On the other hand, coherent scatter echoes provide an indication of the turbulent state of the ionospheric plasma. This dissertation describes coherent and incoherent backscatter radar observations of the F region ionosphere in the magnetic equatorial region using the Jicamarca IS radar in Peru and the São Luís coherent backscatter radar in Brazil. The possibility of an alternative IS radar technique for topside ionosphere observations was investigated, and traditional IS techniques were revisited in an attempt to improve electron density observations made at the Jicamarca Radio Observatory. Also, new measurements made with the radar in Brazil are presented which provide additional evidence of plasma waves predicted by a recently proposed theory. Overall, the results in this dissertation provide additional, more accurate information about the equatorial ionosphere in its equilibrium and turbulent states.

1.1 Motivation for the study of the ionosphere

The ionosphere is a natural laboratory for the study of plasmas, and it provides the opportunity for studies of basic plasma phenomena without the difficulties involving plasma confinement. Nevertheless, scientific efforts are necessary for

the development of the appropriate tools for in-situ and remote sensing measurements. Ionospheric plasma studies are also important from an engineering point of view. Electron density irregularities in the ionosphere are generated by a number of different plasma instabilities. Small-scale plasma irregularities can cause fluctuations in the amplitude and phase of transionospheric radio signals. These fluctuations are called ionospheric scintillations and can be strong enough to cause the disruption of satellite-based communication and navigation systems (e.g. *Yeh and Liu, 1982; Aarons, 1982; Basu et al., 1988; Groves et al., 1997; Kintner and Ledvina, 2005*).

The ionosphere is also responsible for additional propagation time delays in signals from satellite-based positioning systems (e.g. *Klobuchar, 1996; Klobuchar et al., 2002*). These delays must be accurately taken into account for precise position estimation. Therefore, a good knowledge on the variability of the ionospheric electron content is necessary, especially in life-critical applications like GPS-aided aviation (*Kintner et al., 2007*). It is well known that the ionosphere at low and high latitudes is variable and unstable, requiring a greater deal of investigation (*Aarons, 1982*). Fig. 1.1 shows an example of typical ionospheric density variability and associated transionospheric signal power fluctuations measured with a GPS receiver.

1.2 Motivation for the IS radar studies in this dissertation

The IS radar studies in this dissertation are motivated by recent advances in the understanding of electron Coulomb collision effects at small aspect angles (*Sulzer and González, 1999; Woodman, 2004; Kudeki and Milla, 2006*). Both ion and

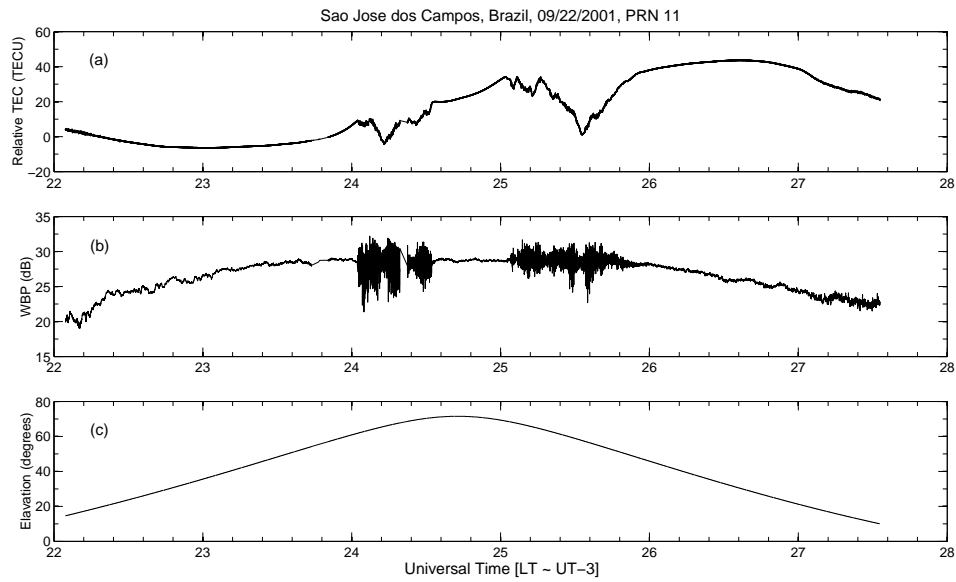


Figure 1.1: Example of density fluctuations and ionospheric scintillations observed in the low latitude ionosphere with a dual-frequency GPS receiver. Panel (a) shows the relative total electron content (TEC) estimated from the travel time difference between two signals with different frequencies. The signals were transmitted by a GPS satellite and received by a ground receiver. Panel (b) shows the fluctuations in the signal amplitude associated with fluctuations in the TEC. Panel (c) shows the elevation angle of the GPS satellite from which the signals were transmitted.

electron Coulomb collisions have effects on the IS spectra at small aspect angles with consequences for the estimation of ionospheric parameters from IS radar measurements. The magnetic field and electron Coulomb collisions also have a strong effect on the IS radar cross section (RCS) at small aspect angles. A precise knowledge of the RCS is required to correct backscatter power profiles as to accurately represent electron density profiles.

Another motivation for the IS radar studies is the necessity of accurate elec-

tron density measurements for investigating the dynamics of the equatorial ionosphere and for providing absolute density profiles for calibration and validation of satellite observations (e.g. DMSP, C/NOFS, and COSMIC) (e.g. Venkattraman *et al.*, 2005; Lei *et al.*, 2007). Finally, the lack of information about temperatures and ion composition in the equatorial topside ionosphere and the possibility of estimating information about the neutral atmosphere when accurate ionospheric measurements are available also serve as motivations for this study (e.g. Aponte *et al.*, 1999).

1.3 Motivation for the coherent scatter radar studies in this dissertation

This dissertation also describes a study of large-scale waves in the bottomside F region using a small coherent backscatter radar in Brazil (*de Paula and Hysell, 2004a*). This study is motivated by the ability of this radar to produce interferometric radar images of scattering structures with a wider field of view than is currently possible at Jicamarca. This feature makes it more appropriate for the study of structures with scale-sizes of a few tens of km. Decakilometric waves have been detected previously at the onset of fully developed F region radar plumes during equatorial spread F events, and a causal relationship between these waves and spread F was suggested (*Hysell et al., 2004a*). The density irregularities causing radar plume echoes share their origin with the irregularities causing ionospheric scintillation. Coherent backscatter radar imaging observations can provide additional information that may help our understanding of the generation and dynamics of equatorial spread F .

1.4 Organization of this dissertation

Chapter 2 gives introductory information about the ionosphere with a few more details pertaining to the ionospheric F region at low magnetic latitudes, the main subject of this dissertation. Chapter 3 gives information about remote sensing of the ionosphere using radars. The IS technique used to estimate electron density, temperatures, and ion composition is explained in some detail in this chapter. A description of the coherent backscatter technique used to investigate non-thermal magnetic field-aligned density irregularities is explained as well. Chapter 4 describes a study of the IS radar cross section at small aspect angles with implications in the electron density measurements made at Jicamarca Radio Observatory. Chapter 5 describes observations of the proton gyroresonance. Simultaneous measurement of the temperature and ion composition in the topside ionosphere was attempted in this experiment. Chapter 6 describes a study of large-scale plasma waves in the bottomside of the equatorial F region and equatorial spread F using coherent backscatter radar imaging and observations made by the São Luís radar in Brazil. Finally, main results and suggestions for future work are summarized in Chapter 7.

CHAPTER 2

THE EARTH'S IONOSPHERE

2.1 Introduction

This dissertation discusses new techniques and results related to radar remote sensing of the Earth's ionosphere. This chapter reviews fundamental concepts in ionospheric composition, dynamics, and energetics. The material presented here is a compilation of well-known results found in various textbooks (e.g. *Banks and Kockarts, 1973a,b; Baumjohann and Treumann, 1997; Davies, 1990; Giraud and Petit, 1978; Hargreaves, 1995; Kelley, 1989; Rishbeth and Garriot, 1969; Schunk and Nagy, 2000*). Readers who are familiar with this material may wish to skip to the next chapter.

The chapter starts with a brief description of the Earth's atmosphere. The formation of the ionosphere in the upper atmosphere is then explained through the derivation of a typical ionospheric density profile. This discussion helps motivate the results presented in Chapter 4 which pertain to improvements in radar measurements of electron density profiles. Next, the thermal structure and composition of the ionosphere are reviewed. Relevant radar measurements of ionospheric temperatures and ion composition will be presented in Chapters 4 and 5. Subsequent sections of the chapter review the dynamics of the ionosphere at low latitudes. The treatment here begins by introducing the concept of the ionosphere as a magnetized plasma. Mathematical expressions for the velocity of the ionized species forming the ionospheric plasma are derived and used to develop an expression for the current density in the ionosphere. Next, the generation of electric fields and the role of atmospheric neutral winds in

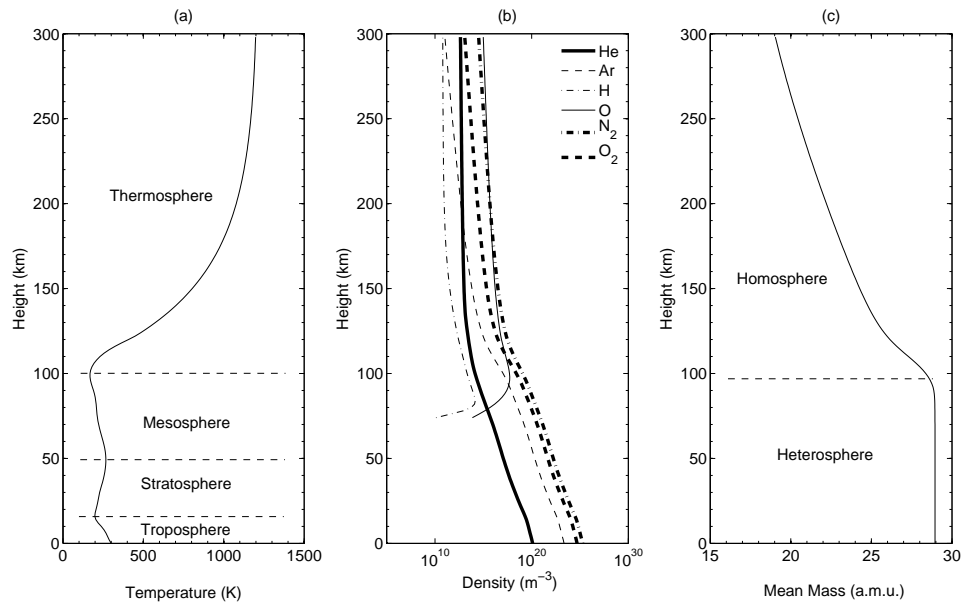


Figure 2.1: (a) Height variation of neutral temperature. (b) Vertical distribution of neutral components. (c) Vertical variation of the mean molecular mass. These profiles were generated using results from the Mass Spectrometer - Incoherent Scatter (MSIS) model of the atmosphere (*Picone et al., 2002*).

the upper atmosphere are discussed. The focus will be on the ionosphere at low magnetic latitudes. Here, the magnetic field is almost horizontal, and the ionosphere consequently takes on a few unique properties. Some of these are explained in detail since they are connected with equatorial spread F, the subject of Chapter 6.

2.2 The Earth's atmosphere

The Earth's atmosphere is composed of a number of different gases. It is usually divided into regions (or layers) according to the height variation of the tem-

perature or composition. Classification according to the temperature profile is used more frequently. The vertical temperature profile has a number of inflection points that are used to define the boundaries between atmospheric regions. Panel (a) of Fig 2.1 shows a typical vertical profile of the temperature in the Earth's atmosphere with the different atmospheric regions indicated. These regions are described in the following sections.

2.2.1 The lower atmosphere

The lower atmosphere is formed by the troposphere. All the weather phenomena occur within this atmospheric region. The temperature in this region decreases with altitude as a result of surface warming by solar radiation. The tropopause is the first minimum in the temperature profile and defines the upper boundary between the troposphere and the middle atmosphere. The tropopause ranges from approximately 8 km at high latitudes to 18 km at the equator and also varies with season.

2.2.2 Middle atmosphere

The stratosphere and mesosphere form the middle atmosphere. The middle atmosphere has a "bump" in the temperature profile due to absorption of solar ultra-violet (UV) radiation by the ozone layer. This maximum in the temperature profile indicates the mesopause, the boundary between stratosphere and mesosphere. Commercial airplanes usually fly in the lower reaches of stratosphere (≈ 10 km) to avoid stronger turbulent atmospheric convection in the tro-

posphere. The ozone layer, responsible for absorption of the solar UV radiation, can be found at the stratopause. In the mesosphere, the temperature starts to decrease with altitude again. The lowest atmospheric temperatures occur at the mesopause and can be as low as 130 K during the summer in the polar region (e.g. *Von Zahn and Meyer, 1987*).

2.2.3 Upper atmosphere

The upper atmosphere is composed of the thermosphere and exosphere. The thermosphere is the next atmospheric region above the mesosphere. In the thermosphere, the temperature gradually increases with altitude until it reaches an approximately constant value, usually referred to as the exospheric temperature. The exosphere is the uppermost atmospheric layer. In the exosphere, the free mean-path is long enough to allow particles to follow ballistic trajectories, and those with sufficient energy can escape from the Earth's gravitational field.

2.2.4 Atmospheric composition

The origin and composition of the Earth's atmosphere have been attributed to crustal outgassing (N_2 , H_2O , CO_2), nuclear radioactive decay (Ar, He), and biophotosynthesis (O_2) over the past billions of years (*Giraud and Petit, 1978*). Panel (b) of Fig. 2.1 shows the composition of the neutral atmosphere as a function of height. The mean molecular mass is approximately constant until 100 km. This region of constant mean mass is referred to as the homosphere. Above 100 km, the mean mass decreases with height, and this region is known as the

heterosphere. The transition height between the homosphere and heterosphere is called turbopause. As an illustration, Panel (c) of Fig. 2.1 shows the height variation of the mean molecular mass. In the heterosphere, hydrostatic equilibrium is a good approximation for the vertical distribution of the atmospheric constituents, since the overwhelming forces are gravity and vertical pressure gradients (*Giraud and Petit, 1978*). It will be shown in the following sections that the formation of the ionosphere strongly depends on the density profile of the atmospheric constituents. Therefore, a good knowledge about the neutral atmosphere is crucial for accurate modelling of the ionosphere.

2.3 The ionosphere

The ionosphere can be defined in a number of different ways. Following the classic work of *Rishbeth and Garriot (1969)* and within the context of this dissertation, the ionosphere is defined as a part of the upper atmosphere where ions and electrons are present in quantities sufficient to affect the propagation of radio waves. The ionosphere can start at a height as low as 50 km and extend over a few thousand kilometers.

2.3.1 Formation

The ionosphere is formed mainly by ionization of neutral constituents by solar radiation, especially in the extreme ultra-violet (EUV), ultra-violet (UV) and X-ray ranges. A secondary source of ionization is the precipitation of energetic particles. Ionization is produced when the energy of the ionizing photons ($h\nu$)

or particles (kinetic) exceeds the ionization potential of an atom or molecule in the atmosphere. Ionization caused by photons is called photoionization, and ionization caused by particle precipitation is called impact ionization.

Photoionization

The production rate of ion-electron pairs is easily derived for a one-component atmosphere that is illuminated by solar monochromatic radiation and whose neutral density variation with height ($n(h)$) follows the barometric law:

$$n_n(h) = n_o e^{-h/H} \quad (2.1)$$

where $H = k_B T_n / m_n g$ is the scale height for an isothermal atmosphere with atoms of mass m_n and temperature T_n , g is the gravitational acceleration, k_B is the Boltzmann constant, and n_o is the density at $h = 0$. The solar radiation reaches the Earth's atmosphere at a zenith angle χ , as illustrated in Fig. 2.2. In this figure and in the derivation that follows, the atmosphere is considered plane and horizontally stratified.

The local production of electron-ion pairs at height h is the photoionization rate per unit volume $P_\lambda(h)$ [electrons/m³s]. The photoionization rate is proportional to the product of the four quantities: the radiation absorption cross section σ_λ [m²], which is assumed to be constant with height in this analysis, the neutral density number $n_n(h)$ [m⁻³], the radiation intensity $I(h)$ [eV/m²s], and the photoionization efficiency κ_λ [~ 1 ion pair per 35 eV in air]. Therefore:

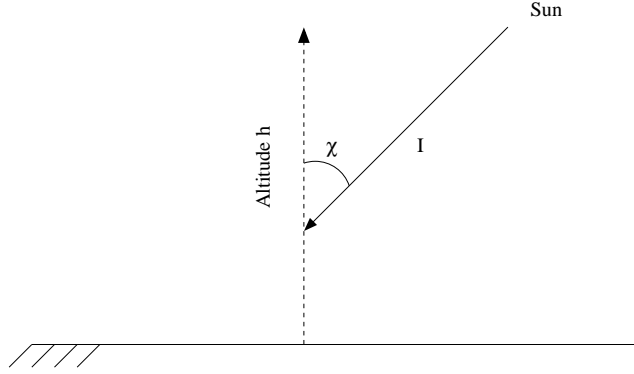


Figure 2.2: Solar radiation and photoionization of the atmosphere.

$$P_{\lambda}(h) = \kappa_{\lambda} \sigma_{\lambda} n_n(h) I_{\lambda}(h) \quad (2.2)$$

where the subscript λ indicates that monochromatic radiation is considered. Since a model for the height variation of the neutral density is given, it is necessary to find an expression that describes the height variation of the radiation intensity. The attenuation of radiation $dI(s)$ along the oblique ray path ds is given by:

$$dI_{\lambda}(s) = -\sigma_{\lambda} n_n(s) I_{\lambda}(s) ds \quad (2.3)$$

Noting that $dh = -ds \cos \chi$, where χ is the zenith angle, and integrating both sides of Eq. 2.3, the height variation of the radiation intensity can be found:

$$I(h) = I(\infty) \exp \left[-\frac{\sigma_{\lambda} n_o H}{\cos \chi} \exp \left(-\frac{h}{H} \right) \right] \quad (2.4)$$

where, $I(\infty)$ is the incident radiation intensity on the top of (or outside) the atmosphere. Eq. 2.4 shows that, as expected, the intensity of the solar radiation decreases with altitude. The production rate can now be written as:

$$P_{\lambda}(h) = \kappa_{\lambda} \sigma_{\lambda} n_o I(\infty) \exp \left[-\frac{h}{H} - \frac{\sigma_{\lambda} n_o H}{\cos \chi} \exp \left(-\frac{h}{H} \right) \right] \quad (2.5)$$

A change of variables yields a cleaner expression known as the *Chapman production function*:

$$P_{\lambda}(h) = P_{\lambda 0} \exp \left[1 - \zeta - \frac{\exp(-\zeta)}{\cos \chi} \right] \quad (2.6)$$

where,

$$\zeta = \frac{h - h_0}{H} \quad (2.7)$$

and $h_0 = H \ln(\sigma_{\lambda} n_o H)$ is the height of maximum ionization rate $P_{\lambda 0}$ for vertical incidence ($\chi = 0$) of the solar radiation:

$$P_{\lambda 0} = \frac{\kappa_{\lambda} I(\infty)}{eH} \quad (2.8)$$

Despite its mathematical simplicity, the Chapman production function can explain some of the characteristics observed in a real ionospheric profile. For instance, the decrease of the maximum density and the upward motion of the

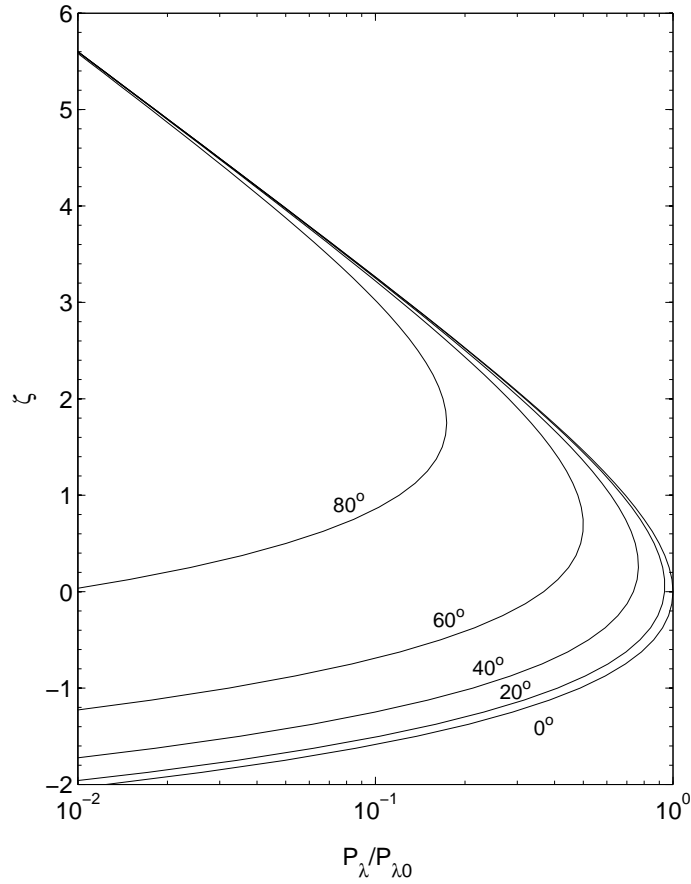


Figure 2.3: Normalized production rate $P_\lambda/P_{\lambda 0}$ for different values of zenith angle.

peak density with the increase of zenith angle. To illustrate this, Fig. 2.3 shows normalized production rate profiles (Eq. 2.6) for different zenith angles.

A more realistic description of the ionospheric density profile can be obtained by considering an atmosphere with multiple constituents and absorption cross sections that are radiation wavelength dependent. Such an expression can be written as (*Schunk and Nagy, 2000*):

$$P(\chi, h) = \sum_s n_s(h) \int_0^{\lambda_{si}} I_\infty(\lambda) e^{-\tau(\lambda, \chi, h)} \sigma_s^i(\lambda) d\lambda \quad (2.9)$$

where $\tau(\lambda, \chi, h)$ is the wavelength-dependent optical depth for the ionizing radiation, $\sigma_s^i(\lambda)$ is the wavelength-dependent ionization cross section, and λ_{si} is the ionization threshold wavelength for neutral species s . The summation is carried out over all the neutral species s .

2.3.2 The ionospheric profile

The previous section described how free electrons and ions can be produced by solar photoionization. A few more details about the ionospheric density profile is given in this section. Fig. 2.4 shows an ionospheric profile representative of typical daytime observations. Multiple observations with in-situ rocket and satellite measurements combined with radio remote sensing of the ionosphere have shown structures within the ionospheric density profile. These substructures are defined as ionospheric layers or regions. The major ionospheric regions are: the D region, below ~ 90 km, the E region, between ~ 90 and ~ 130 km, and the F region, above ~ 130 km. The F region is usually divided into the F_1 and F_2 regions during the day.

It will be shown that the basic shape of the ionospheric density profile at E and F region heights can be explained if one considers the photochemical and diffusive equilibrium solutions for the electron continuity equation:

$$\frac{\partial N_e}{\partial t} = P - L - \nabla \cdot (N_e \mathbf{V}) \quad (2.10)$$

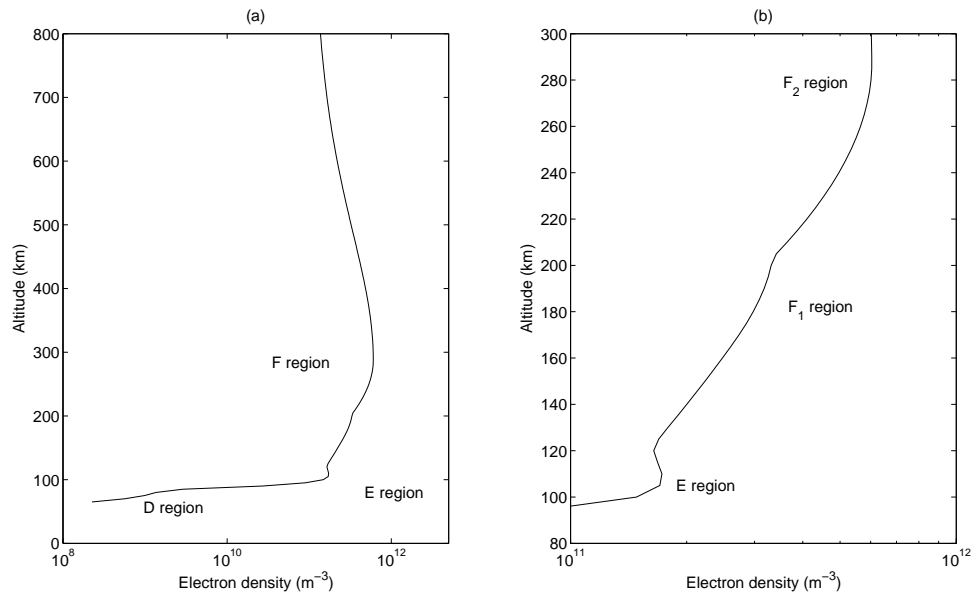


Figure 2.4: (a) Typical mid-latitude ionospheric density profile. (b) Expanded view of the E and F regions.

Where, N_e is the electron density, P and L are the electron production and loss rates, respectively, and $\nabla \cdot (N_e \mathbf{V})$ is the rate of change of density due to transport. In the ionosphere below 200 km, the transport term can be neglected when compared to production and loss terms. Additionally, the left-hand side term ($\frac{\partial N_e}{\partial t}$) is small when compared with the other terms and can be neglected as well (e.g. *Rishbeth and Garriot, 1969; Giraud and Petit, 1978; Hargreaves, 1995*). Consequently, a condition of photochemical equilibrium state ($P = L$) is found at D , E and F_1 heights. Above 250 km, the transport term becomes more important than the the photochemical terms (P and L) and diffusion takes place. The photochemical processes in the D region are relatively complicated, loss process are poorly understood and finding a D layer equilibrium profile is not an easy

task (Luhmann, 1995). Therefore, the D region will not be addressed in this brief discussion and focus will be given on the E and F regions. The photochemical processes at E and F_1 heights less complex and will be examined next.

Chemistry of the E and F_1 regions

It was mentined in the previous paragraphs that a photochemical equilibrium state is found in the lower ionosphere. Here, a solution for the electron density distribution at these heights is examined. It is anticipated that negative ions are absent in the E and F_1 regions (e.g. Hargreaves, 1995; Luhmann, 1995; Rishbeth and Garriot, 1969). Negative ions can be found, however, in the lower D region. Therefore, only production/loss of electron and positive ions need to be considered in this analysis.

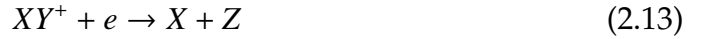
Atomic ions and free electrons are mainly produced by direct solar photoionization (P), while production of molecular ions by photoionization can be neglected. This assumption is justified by the fact the O_2 is a minor constituent at E and F region heights and N_2^+ is quickly lost by dissociative recombination (Rishbeth and Garriot, 1969). To simplify this analysis, the possibility of N_2^+ to produce other ions is also neglected. Molecular ions are mainly produced by ion-atom interchange reactions:



Atomic ions can be lost through radiative recombination:



However, this is a slow process and it is only the fastest process at upper ionospheric heights (> 250 km). As mentioned earlier, transport processes are dominant at these heights and losses by radiative recombination can be neglected. Molecular ions and electrons are lost through dissociative recombination at heights below approximately 200 km (*Rishbeth and Garriot, 1969*):



Therefore, one can write the following set of continuity equations for electrons, atomic and molecular ions:

$$\frac{d}{dt}N_e = P - \alpha N_e N_{M^+} \quad (2.14)$$

$$\frac{d}{dt}N_{A^+} = P - \gamma N_M N_{A^+} \quad (2.15)$$

$$\frac{d}{dt}N_{M^+} = \gamma N_M N_{A^+} - \alpha N_e N_{M^+} \quad (2.16)$$

where, N_e , N_{A^+} , N_{M^+} , and N_M are the concentrations of electrons, atomic ions, molecular ions and molecular species, respectively, α is the rate coefficient of molecular recombination and γ is the rate coefficient of ion-atom interchange. Assuming equilibrium conditions, one can obtain from Eq. 2.16 the following relationship for the ratio of atomic-to-molecular ion densities:

$$\frac{N_{A^+}}{N_{M^+}} = \frac{\alpha N_e}{\beta} \quad (2.17)$$

where, $\beta = \gamma N_M$. Assuming charge neutrality ($N_e = N_{M^+} + N_{A^+}$) and making use of Eq. 2.14 and Eq. 2.15, one finds the following relationship:

$$\frac{1}{P} = \frac{1}{\beta N_e} + \frac{1}{\alpha N_e^2} \quad (2.18)$$

Two important limiting cases of Eq. 2.18 can be considered: $\beta \ll \alpha N_e$ and $\beta \gg \alpha N_e$. The case where $\beta \gg \alpha N_e$ leads to a dominance of molecular ions species (see Eq. 2.17), and the so-called α -Chapman function for the electron density:

$$N_e = \left(\frac{P}{\alpha} \right)^{1/2} \quad (2.19)$$

The other case, where $\beta \ll \alpha N_e$ suggests a dominance of atomic ion species, and one finds the so-called β -Chapman function:

$$N_e = \frac{P}{\beta} \quad (2.20)$$

A realistic ionospheric profile cannot be fully represented by the α or β Chapman functions alone. These functions, however, can explain the shape of some of the regions found in a typical ionospheric profile.

The coefficient α may vary with temperature but, otherwise is height independent. On the other hand, the coefficient β depends on the density of the

molecular neutral constituents and decreases rapidly with height.

***E* region**

At *E* region heights, the $\beta \gg \alpha N_e$ regime dominates and the density distribution can be represented by the α -Chapman function. The electron distribution in the *E* region is obtained when considering solar radiation in the 0.8–14.0 nm (X-ray) and 79.6–102.7 nm (UV) ranges. These two ranges of radiation result in production rate profiles with maxima around 105 and 115 km. When the contribution from these two ionizing sources are combined, a maximum production rate is found around 110 km. (e.g. *Rishbeth and Garriot, 1969*). Fig. 2.4 shows that the *E* layer is a well-defined layer that can be approximated by an α -Chapman function with density peak (h_0) around 110 km. Recently, (*Shume et al., 2005*) found a good agreement between *E* density profiles measured by radar and the α -Chapman function.

***F* region**

The maximum of electron production rates for ionizing radiation in the 14.0–79.6 nm range occurs around 150–170 km, and the transition between the $\beta \gg \alpha N_e$ and $\beta \ll \alpha N_e$ regimes occurs around 170–200 km (*Rishbeth and Garriot, 1969*). This height of maximum production is well below the height of maximum density found in typical ionospheric profiles (see Fig. 2.4(a) for instance). Therefore, the *F* region density profile cannot be fully explained in terms of photochemistry only. Additionally, Fig. 2.4 shows that the *F* region splits into the F_1 “ledge” and the F_2 region.

Above the peak of maximum F region production, the production rate decreases exponentially with altitude according to the Chapman production function. The coefficient β also decreases with altitude. Therefore, given the right conditions, the resulting electron density described by the β -Chapman function can increase with height. To illustrate this, an expression for the electron density distribution as a function of the production P and of the height profiles for β and α is obtained from the positive root of Eq. 2.18:

$$N_e = \frac{P}{2\alpha} \left[1 + \left(1 + \frac{4\beta^2}{\alpha P} \right)^{1/2} \right] \quad (2.21)$$

Next, following *Rishbeth and Garriot* (1969), the β profile is modelled as $\beta(\zeta) = \beta_0 e^{-1.75\zeta}$, where ζ is the reduced height and the α profile is assumed to be constant with height. Fig. 2.5 shows the result density distribution obtained from Eq. 2.21 for $\frac{\beta_0^2}{\alpha P_0} = 9$. The α -Chapman profile is also shown for comparison. This simple calculation is able to reproduce the F_1 “ledge” in a typical profile as shown in Fig. 2.4.

Fig. 2.5 also shows that, above the height of maximum production ($\zeta = 0$), the electron density increases with altitude. This is because the transport term was not taken into consideration in this simple analysis. Considering only vertical motions, which are important at F_2 heights, the continuity equation (assuming steady-state equilibrium) for the electrons can be written as:

$$0 = P - \beta N_e - \frac{\partial}{\partial z} (N_e V_z) \quad (2.22)$$

A full solution for the density distribution from the equation above requires a

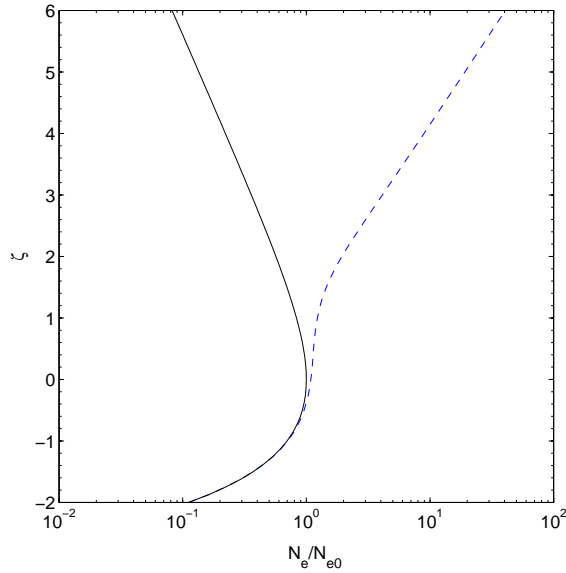


Figure 2.5: Normalized electron density versus reduced height $\zeta = \frac{h-h_0}{H}$. The solid line is the α -Chapman profile (Eq. 2.19), and the dashed line shows the density profile described by Eq. 2.21.

complete description of the vertical velocity V_z , which would include the effects of thermospheric neutral winds, pressure gradient, gravity and electric fields (e.g. *Schunk and Nagy, 2000*).

In the simplest case, the vertical component of the velocity driven by pressure gradient and gravity forces acting on electron and ions is considered. This will lead to the “ambipolar” diffusion equation (e.g. *Giraud and Petit, 1978; Schunk and Nagy, 2000*). This velocity equation takes into account the ambipolar electric field that will naturally arise from the differences in the diffusivity rates for electrons and ions and the necessity to maintain charge neutrality.

The solution for the electron density profile from the continuity equation at heights well above the maximum production peak (topside F region) shows that

the electron density decreases with height with an ambipolar scale height that is inversely proportional to the mass of the major ion and directly proportional to both electron and ion temperatures (e.g. *Giraud and Petit, 1978; Rishbeth and Garriot, 1969; Schunk and Nagy, 2000*). This is called the ambipolar diffusive equilibrium. As it will be shown later in this chapter, O^+ and light ions (H^+ and He^+) are found in the topside ionosphere. Light ions have a larger ambipolar scale height than O^+ ions and, consequently, they become the dominant ions at higher altitudes. The F_2 peak occurs at a height where diffusion and loss are of comparable importance (e.g. *Giraud and Petit, 1978; Rishbeth and Garriot, 1969*).

2.3.3 Temperatures

Electron and ion temperatures can be estimated from ionospheric radar observations as it will be shown in the next chapter. Here, a few details about the thermal structure of the ionosphere are given. Fig. 2.6 shows typical profiles of electron density, temperature, and ion composition for the ionospheric plasma at a mid-latitude location during daytime hours. Characteristics of the electron density profile were discussed previously. Panel (b) of Fig. 2.6 shows the temperature profiles for neutrals, electrons, and ions. Until the sixties, ions and neutrals were thought to be in thermal equilibrium in the upper atmosphere (*Banks and Kockarts, 1973b*). In situ and radio remote sensing measurements showed that, under most circumstances, this is not the case. It was shown that the temperature of electrons is higher than the temperature of ions, which in turn exceeds the neutral temperature.

The basic reason for the lack of thermal equilibrium is that the ionizing pho-

tons or charged particles have energies that exceed the energy required for ionization. Much of the excess energy is passed to the photoelectrons and is subsequently passed to the other species. The temperatures of the different species is determined by the competition between various heating, cooling, and energy flow processes. Although the heat input to the neutral atmosphere is about an order of magnitude greater than the heat input to the electron gas, the heat capacity per unit volume of the electrons is several orders of magnitude smaller than that of neutral atmosphere. Efficient heat transfer by Coulomb collisions between ions and electrons keeps the ion temperature above the neutral temperature.

In general, the ion gas exhibits a smaller thermal variability than the electron gas. The ion temperature profile is determined by the balance of heat gained from the electrons and lost to the neutrals. Thus, the ion temperature converges towards the neutral temperature in the dense lower thermosphere and towards the electron temperature in the topside ionosphere. Thermal equilibrium among neutrals and charged constituents is usually assumed below approximately 120 km altitude as a result of the high neutral density and large collision frequencies.

2.3.4 Ion composition

Estimation of ionospheric ion composition from radar observations is also discussed in this dissertation. This section gives an overview of the vertical ion distribution in the ionospheric F region. Panel (c) of Fig. 2.6 shows the IRI model prediction for the densities of positive ions forming the ionosphere. As

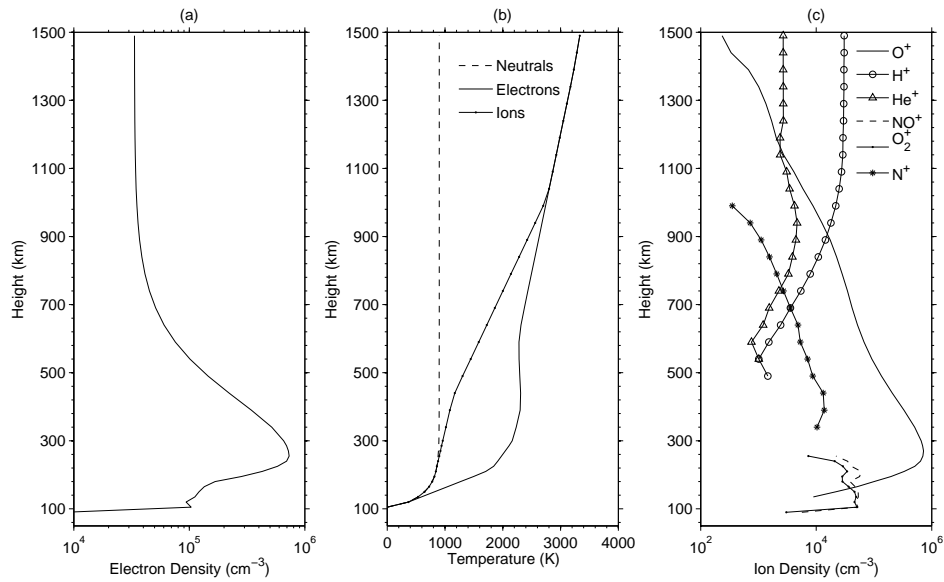


Figure 2.6: Daytime profiles obtained from the International Reference Ionosphere - IRI empirical model (Bilitza, 2001) for a mid-latitude ionosphere: (a) electron density, (b) temperatures and (c) ion composition.

a first approximation, ions in the mid-latitude ionosphere seem to distribute themselves along magnetic field lines according to an ambipolar diffusive equilibrium, with the heaviest ions found at lower ionospheric heights and the lightest ions in the topside ionosphere. Ion composition measurements are difficult and rare. New measurement techniques need to be developed and predictions of numerical models still need to be validated. That said, the profiles shown in Fig. 2.6 (c) should be taken just as a qualitative representation of the ion composition rather than an accurate quantitative description.

The main F region

The F region is formed mainly by atomic oxygen ions and a small fraction of nitrogen ions that is generally neglected in radar studies. In some practical applications, a purely O^+ ionospheric plasma is assumed. This is the case for some assimilative numerical models of the ionospheric electron density used for the estimation of the ionospheric delay in GPS signals (e.g. *Wang et al.*, 2004). When a more precise shape of the density profile is required, the molecular ions in the bottomside F region and light ions in the topside ionosphere must be taken into consideration.

The bottomside ionosphere

Most of the ion species in the ionosphere can be produced by direct photoionization of neutral constituents. This, however, does not imply that photoionization is the only source of these ions. Other processes such as charge exchange can be important as well. In fact, photoionization might not be the main ionization source for some ion species. In the bottomside F region, for instance, NO^+ is a result of chemical reactions between neutral and ionized species. Molecular ions exist at heights that are too low for satellite measurements. These heights can be probed by rockets, but this type of measurement is relatively expensive and provides a limited data set. Incoherent scatter radars could provide the main source of information for observations of molecular ions. However, the small mass ratio between molecular ions and O^+ is responsible for ambiguities in the estimation of the ion composition/temperatures from the radar measurements, and independent information is required for estimation of the fraction of molecular ions (e.g. *Aponte et al.*, 2007). A brief discussion on a possible ad-

ditional source of information regarding molecular ion fraction at Jicamarca is presented in Chapter 4.

The topside ionosphere

The topside ionosphere is formed by a mixture of O^+ and light ions (H^+ and He^+). H^+ can be produced by direct ionization of the atomic hydrogen, but production of H^+ can also occur through the fast charge exchange mechanism with oxygen ions:



where \rightleftharpoons indicates a reversible reaction. The height at which the O^+ ionosphere turns into a H^+ dominated ionosphere is usually referred to as the O^+ - H^+ transition height. H^+ produced by photoionization and charge exchange flows upwards into the protonosphere during the day. At night, when photoionization stops, a downward flow of H^+ is observed back into the ionosphere, and reverse charge exchange occurs, producing O^+ . This downward flow of H^+ is the main source of the ionospheric O^+ at night and plays an important role in the maintenance of the nighttime ionosphere.

Until the fifties, the topside ionosphere was believed to be formed by an H^+ plasma. In the early sixties, however, the hypothesis that Helium could be an important constituent of the exosphere also indicated the possibility that He^+ be part of the topside ion composition (*Nicolet, 1961; Hanson, 1962*). Also in the early sixties, the first experimental evidence was obtained of a mixture of O^+ , H^+

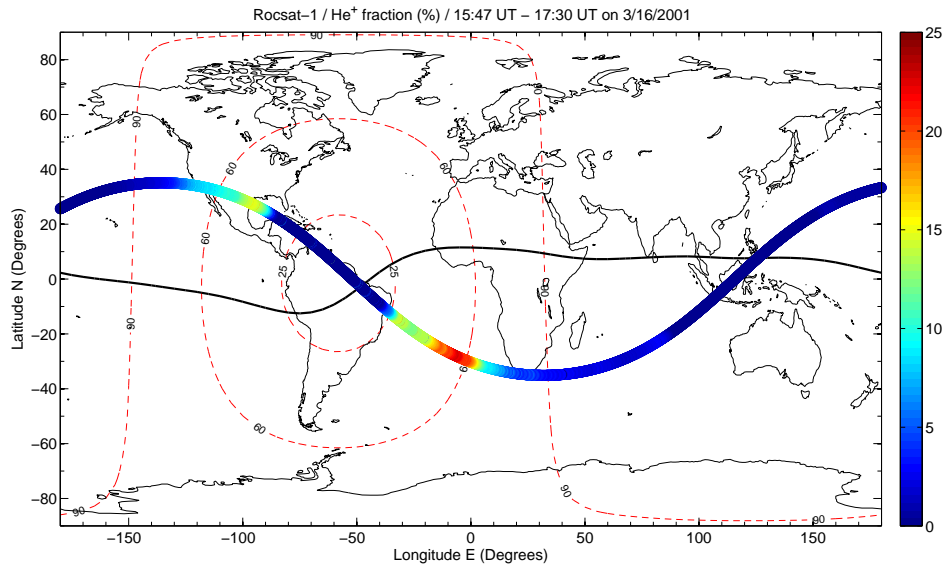


Figure 2.7: He^+ fraction (%) measured during an orbital cycle by the ROCSAT-1 satellite on March 13, 2001 between 15:47 UT and 17:30 UT. Dashed lines indicate solar zenith angles calculated for 16:37 UT.

and He^+ ions in the topside ionosphere (e.g. *Bourdeau et al.*, 1962). A number of initial observations indicated that the fraction of He^+ in the topside to be small (e.g. *Carlson and Gordon*, 1966). These studies, however, were representative of low solar flux conditions. More recent studies using incoherent scatter radar observations at Arecibo showed that the fraction of He^+ can be as large as 30% of the total ion content at night during high solar flux conditions (*Erickson and Swartz*, 1994). Further studies at Arecibo showed the presence of a nighttime He^+ layer located around the O^+ - H^+ transition height (*González and Sulzer*, 1996). Satellite observations indicate a minimum in the He^+ concentration at equatorial latitudes, in contrast with mid-latitude observations indicating that He^+ can be a dominant ion during high solar flux years (*Heelis et al.*, 1990).

Fig. 2.7 presents an example of ion fraction measurements made by the ROCSAT-1 satellite. ROCSAT-1 had a low inclination (35°), circular orbit (600 km). Among other instruments, ROCSAT-1 had a retarding potential analyzer (RPA) for ion (O^+ , H^+ and He^+) fraction measurements. The satellite was launched on January 27, 1999, and the mission officially ended on June 16, 2004. Fig. 2.7 shows an interesting pass of ROCSAT-1 when the orbit was approximately aligned with the magnetic meridian for longitudes between 0° and -100° E (daytime hours). The measurements showed a larger fraction of He^+ at low-to-mid latitudes and a minimum around the magnetic equator.

2.4 Dynamics of the ionospheric plasma

The previous sections provided a general and qualitative description of the ionosphere. The ionosphere can be treated as a magnetized plasma. In the following section, the magnetization source and its importance will be discussed, and the velocity of the ionized species due to different forces will be derived. The results will be used to obtain the electric current density in the ionosphere. Next, the generation of ionospheric electric fields will be discussed. These electric fields are the main drivers of plasma transport in the magnetic equatorial region.

2.4.1 Magnetization of the ionospheric plasma

The ionosphere can be treated as a weakly ionized, magnetized (low β) plasma (e.g *Chen*, 1984). Magnetization is created by the Earth's magnetic (ge-

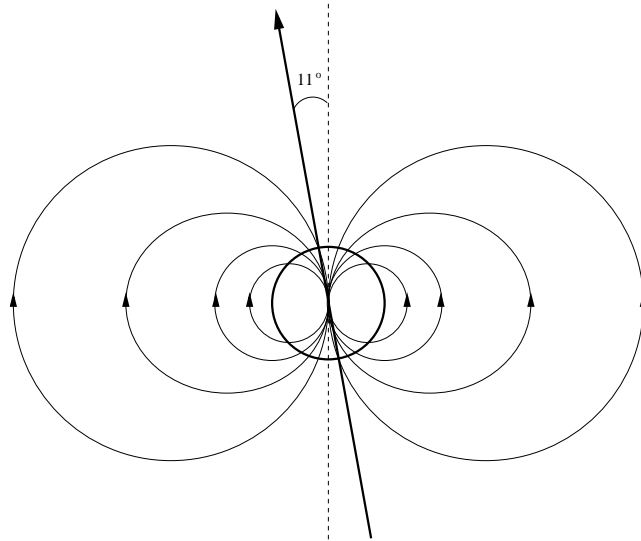


Figure 2.8: Illustration of Earth's magnetic field.

omagnetic) field. The geomagnetic field is believed to be created by electric currents in its liquid metallic outer core with possible influences from the inner solid core (*Jacobs, 1995*). A dynamo theory has been invoked to explain the generation and maintenance of the electric currents. Despite being one of oldest problems in science, details about the generation of Earth's magnetic field are still unknown. To a first order, the geomagnetic field near Earth can be approximated by that generated by a current loop centered in the Earth's core and tilted 11° from its rotation axis as illustrated in Fig. 2.8.

A more accurate mathematical description of Earth's magnetic field is given by the International Geomagnetic Reference Field (IGRF) model. The IGRF is an empirical model that accounts for deviations from the simple dipole model. It also takes into account secular variations in the magnetic field. Small amplitude magnetic field variations due to electric currents in the ionosphere and due magnetospheric disturbances are not considered. In source-free regions at the Earth's surface and above, the main field, with sources internal to the Earth,

is the negative gradient of a scalar potential V , which can be represented by a truncated series expansion:

$$V(r, \theta, \lambda, t) = R \sum_{n=1}^{n_{max}} \left(\frac{R}{r}\right)^{n+1} \sum_{m=0}^n [g_n^m(t) \cos m\lambda + h_n^m(t) \sin m\lambda] P_n^m(\theta) \quad (2.24)$$

where r, θ, λ are geocentric coordinates (r is the distance from the center of the Earth, θ is the colatitude, and λ is the longitude), R is a reference radius (6371.2 km); $g_n^m(t)$ and $h_n^m(t)$ are the coefficients at time t and $P_n^m(\theta)$ are the Schmidt semi-normalized associated Legendre functions of degree n and order m . The main field coefficients are functions of time, and for the IGRF, changes are assumed to be linear over five-year intervals (Maus *et al.*, 2005). The IGRF has been widely used to estimate the angle between the magnetic field and the wavevector of the transmitted signal in radar remote sensing studies. It is used in this dissertation as well.

At high latitudes, the geomagnetic field is almost vertical, while at low latitudes, the geomagnetic field is approximately horizontal, as shown in Fig. 2.9. The direction of the magnetic field has effects on the plasma motion. The magnetic field also has implications for the propagation of radio waves in the ionosphere. The conductivity and the dielectric constant for electromagnetic waves in a magnetized plasma is anisotropic. Ionospheric phenomena are better organized in a coordinate system based on the geomagnetic field than in geographic coordinates. Often, the ionosphere is divided into low, middle, and high magnetic latitudes according to the inclination of the geomagnetic field. Chapters 4, 5 and 6 discuss radar observations of the equatorial ionosphere, where the inclination of the geomagnetic field is zero (see Fig. 2.9).

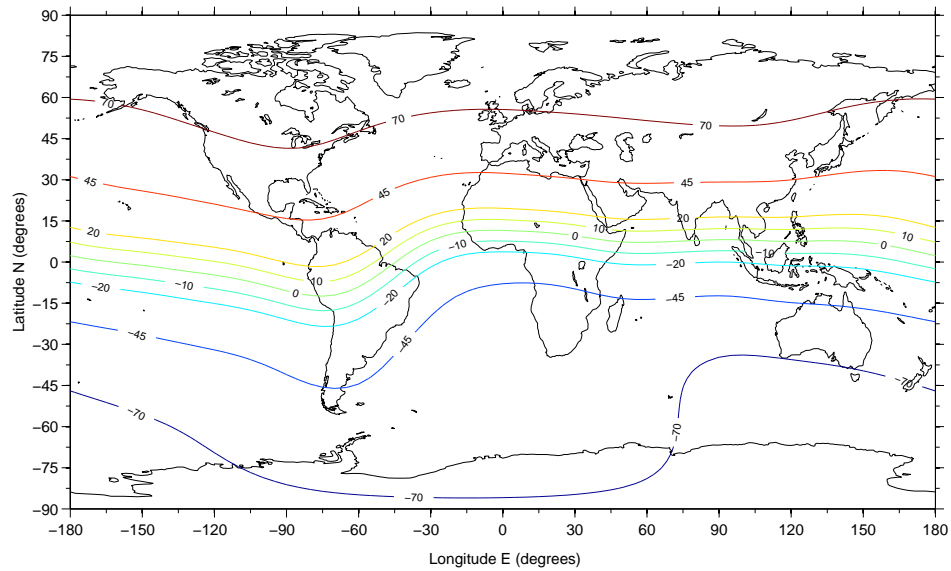


Figure 2.9: IGRF values of magnetic inclination for 2005. The magnetic inclination is the angle between the magnetic field vector and a local horizontal vector.

The following sections will treat the ionosphere as a magnetized plasma and develop mathematical expressions that will help the reader to understand the dynamics of the ionospheric plasma at low magnetic latitudes.

2.4.2 Velocity of the ionized species

The ionospheric plasma will be modelled as three mixed fluids, with electrons and ions immersed in the neutral gas. These fluids are coupled by collisions. Electrons and ions are coupled by their self-generated electric fields. For mathematical simplicity, the following description will treat the plasma as being formed by one neutral constituent, electrons, one ion species, and collisions between ionized species will be neglected. The momentum equation for ions and

electrons in an Earth-fixed coordinate system is given by:

$$\rho_j \frac{d\mathbf{V}_j}{dt} = -\nabla p_j + \rho_j \mathbf{g} + q_j n_j (\mathbf{E} + \mathbf{V}_j \times \mathbf{B}) - \rho_j \nu_{jn} (\mathbf{V}_j - \mathbf{U}) \quad (2.25)$$

where the subscript j denotes ions or electrons, $\rho_j = nm_j$ is the mass density, m_j is the mass, $n = n_i = n_e$ is the number density, V_j is the velocity, p_j is pressure, q_j is the electrical charge, ν_{jn} is the collision frequency between species j and neutrals, and \mathbf{U} is the velocity of the neutral species. From the momentum equation, it will be possible to derive expressions for the velocity of the ionized species.

In the case of an unmagnetized plasma with collisions between ionized species neglected in the momentum equation (Eq. 2.25), the steady state velocity \mathbf{W}_j of each specie is given by (e.g. *Kelley, 1989*):

$$\mathbf{W}'_j = -D_j \frac{\nabla n}{n} + b_j \mathbf{E}' + \frac{D_j}{H_j} \hat{\mathbf{g}} \quad (2.26)$$

where the primed vectors are given in the reference frame moving with the neutral wind, $\hat{\mathbf{g}} = \frac{\mathbf{g}}{|\mathbf{g}|}$, $D_j = \frac{k_B T_j}{m_j \nu_{jn}}$ is the diffusion coefficient, $b_j = \frac{q_j}{m_j \nu_{jn}}$ is the mobility, and $H_j = \frac{k_B T_j}{m_j g}$ is the scale height.

The transformation between the earth-fixed and moving frame coordinates is given by: $\mathbf{V}'_j = \mathbf{V}_j - \mathbf{U}$, $\mathbf{E}' \approx \mathbf{E} + \mathbf{U} \times \mathbf{B}$, and $\mathbf{B}' \approx \mathbf{B}$. The electric and magnetic field transformations take into consideration a wind velocity that is much smaller than the speed of light ($|\mathbf{U}| \ll c$). In a magnetized plasma, the velocity of ions and electrons can be divided in two components, one parallel ($\mathbf{V}'_{j\parallel}$) and another perpendicular ($\mathbf{V}'_{j\perp}$) with respect to the background magnetic field. The parallel

component velocity is given by:

$$\mathbf{V}'_{j\parallel} = \mathbf{W}'_{j\parallel} \quad (2.27)$$

where $\mathbf{W}' = \mathbf{W}'_{j\parallel} + \mathbf{W}'_{j\perp}$. Eq. 2.27 states that forces (gravity, pressure gradient and electric field) parallel to magnetic field would cause ions and electrons to move as if the magnetic field did not exist. The velocity of the ionized species perpendicular to magnetic field is given by:

$$\mathbf{V}'_{j\perp} = \frac{1}{1 + \kappa_j^2} \mathbf{W}'_{j\perp} + \frac{\kappa_j}{1 + \kappa_j^2} \mathbf{W}'_j \times \hat{\mathbf{b}} \quad (2.28)$$

where $\kappa_j = \frac{q_j B}{m_j \nu_{jn}}$ is the ratio of gyrofrequency to collision frequency, and $\hat{\mathbf{b}}$ is a unit vector in the direction of the magnetic field. Eq. 2.28 states that the velocity of ions and electrons is dictated by their collisional or magnetized state. In the collisional regime ($\kappa_j \ll 1$), the species will move in the direction of the applied forces. In the magnetized regime ($\kappa_j \gg 1$), however, electrons and ions will move in a direction perpendicular to both the applied forces and background magnetic field.

In the ionospheric F region, ions and electrons are strongly magnetized ($\kappa_e \gg 1$ and $\kappa_i \gg 1$). Therefore, the perpendicular velocity for ionized species reduces to:

$$\mathbf{V}'_{j\perp} = \frac{1}{B^2} \left[\mathbf{E}' - \frac{\kappa_B T_j}{q_j} \frac{\nabla n}{n} + \frac{m_j}{q_j} \mathbf{g} \right] \times \mathbf{B} \quad (2.29)$$

If the background electric field is strong enough so that pressure gradient and gravity forces can be neglected, a well known result is obtained:

$$\mathbf{V}_{j\perp} = \frac{1}{B^2} \mathbf{E} \times \mathbf{B} \quad (2.30)$$

This result is independent of the reference frame, and states that in a collisionless plasma, ions and electrons move with the same velocity given the action of an electric field perpendicular to the magnetic field.

2.4.3 Current density in the ionospheric plasma

Expressions for the velocity of the ionized species in the ionospheric plasma were presented in the previous section. These equations can now be used to obtain an expression for the current density from the definition:

$$\mathbf{J}' = ne(\mathbf{V}'_i - \mathbf{V}'_e) \quad (2.31)$$

where \mathbf{V}'_e and \mathbf{V}'_i are the electron and ion velocities, respectively. After rearranging various terms, one obtains the following expression for the current density:

$$\mathbf{J} = \sigma_P(\mathbf{E}_\perp + \mathbf{U} \times \mathbf{B}) - \sigma_H(\mathbf{E} + \mathbf{U} \times \mathbf{B}) \times \hat{\mathbf{b}} + \sigma_\circ \mathbf{E}_\parallel \quad (2.32)$$

where σ_P is the Pedersen conductivity, σ_H is the Hall conductivity, and σ_\circ is the longitudinal (or direct) conductivity. In Eq. 2.32, pressure driven and gravity

driven terms were neglected for clarity. Keeping these terms would lead to diamagnetic and gravity-driven current terms. The conductivities are given by:

$$\sigma_0 = ne(b_i - b_e) \quad (2.33)$$

$$\sigma_P = ne \left[\frac{b_i}{1 + \kappa_i^2} - \frac{b_e}{1 + \kappa_e^2} \right] \quad (2.34)$$

$$\sigma_H = ne \left[\frac{b_i \kappa_i}{1 + \kappa_i^2} - \frac{b_e \kappa_e}{1 + \kappa_e^2} \right] \quad (2.35)$$

where subscripts i and e refer to ions and electrons, respectively.

Eq. 2.32 shows that currents in the ionosphere can be driven by electric fields and by the neutral wind moving across the magnetic field lines. It also shows that the electrical conductivity is anisotropic due to the presence of the geomagnetic field. Fig. 2.10 shows typical height profiles of conductivities for an equatorial location around sunset. The direct conductivity is very large and the electric potential can be considered approximately constant along magnetic field lines. This leads to the concept of mapping of transverse electric fields along magnetic field lines (*Farley, 1959; Farley, 1960*) useful to understand a variety of phenomena in the low-latitude ionosphere.

2.4.4 Generation of electric fields

The previous section showed that currents in the ionosphere can be driven by background electric fields and by thermospheric neutral winds moving across magnetic field lines. Here, a brief overview of how electric fields are generated in the ionosphere is presented. More details about electric fields and their effects

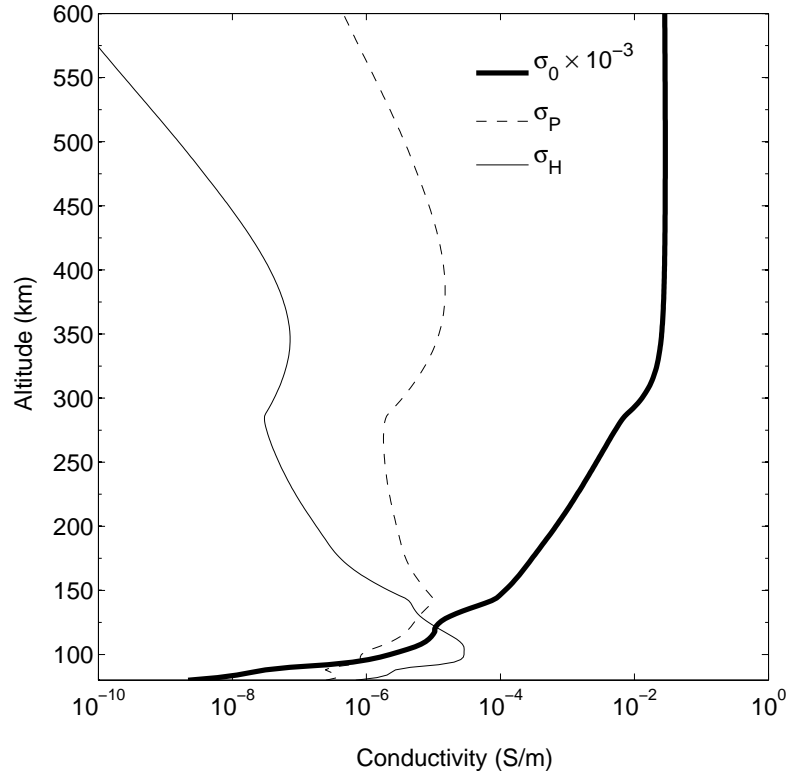


Figure 2.10: Typical conductivity profiles for an equatorial location during sunset hours in the equinox and high solar flux conditions.

in the low-latitude ionosphere are given in later sections in this chapter.

Using Maxwell's equations, one can write an expression for the divergence of current that will prove to be very useful for the understanding of electric field generation in the ionosphere:

$$\nabla \cdot \mathbf{J} = -\frac{\partial \rho_c}{\partial t} \quad (2.36)$$

where ρ_c is the charge density. Another fact of great importance for the understanding of the ionospheric electrodynamics is that the plasma is quasi-neutral,

meaning that, from a macroscopic point of view, there is no charge accumulation in the ionospheric plasma. Therefore, currents in the ionospheric plasma must be divergent-free:

$$\nabla \cdot \mathbf{J} = 0 \quad (2.37)$$

The generation of large-scale electric fields in the ionosphere is attributed to the dynamo-like action of winds in the upper atmosphere. Neutral winds drive electrical currents that must be kept divergence-free. However, it should not be surprising that spatial gradients in the conductivity exist in the ionosphere. Fig. 2.10 indicates that, at least in the vertical direction, these gradients do appear. The gradients in conductivity would cause divergence in the electrical current. To maintain the quasi-neutrality of the plasma, polarization electric fields are generated so that electric field driven currents balance the original neutral wind driven current reestablishing $\nabla \cdot \mathbf{J} = 0$. Next, the origin of atmospheric winds and tides in the upper atmosphere is explained.

2.4.5 Atmospheric winds and tides

Differential solar heating of the atmosphere causes pressure and temperature differences between the day and night hemispheres. The pressure gradient sets up waves and winds which result in air motion that is primarily horizontal. The air motions in the lower and upper thermosphere are both caused by solar heating. Air motions in the lower thermosphere are called tides, while air motions in the upper thermosphere are known as winds. The difference is that

tidal motions in the lower thermosphere are produced mainly by the heating of the ozone layer and propagate upward. The winds in the upper atmosphere are driven by absorption of solar heating by the upper atmosphere itself, and their propagation is mainly horizontal. Neutral winds play an important role in the low latitude equatorial electrodynamics. The following sections will explain how ionospheric electric fields are created by the action of the neutral winds blowing across magnetic field lines.

2.5 The low-latitude F region

The following sections describe some of main features of the low-latitude ionospheric F region, main subject of the research presented in this dissertation (see Chapters 4, 5 and 6). It illustrates the complexity and variability of the low-latitude F region. The low-latitude ionosphere is strongly controlled by the equatorial background electric field whose day-to-day variability is still a subject of investigation.

Most of our knowledge about the dynamics of the ionospheric plasma in the equatorial and low-latitude regions come from the ionospheric plasma drift measurements made at the Jicamarca Radio Observatory. Measurements of drifts are made routinely at Jicamarca using incoherent backscatter radar techniques. The incoherent scatter radar technique used for remote sensing of the ionosphere will be explained in the next chapter. For now, it is sufficient to know that zonal and vertical components of the plasma motion are obtained from the line-of-sight velocities measured by two separate beams, one pointing in the East direction and another point to the West.

2.5.1 Zonal plasma drifts

Fig. 2.11 shows the results of a climatological study of the zonal F region plasma drifts measured at Jicamarca. The zonal drifts are driven by vertical electric fields as described in section 2.4 (see Eq. 2.30). Drifts (electric fields) are westward (upward) during the day and eastward (downward) at night (e.g. *Fejer, 1981*). The magnitude of the zonal drift increases with solar flux. Also, the amplitude of the drifts is larger at night than they are during the day.

The zonal plasma flow pattern is similar to that of the zonal thermospheric wind. The speed of the plasma drift during the day, however, is smaller than the speed of the zonal neutral wind. The zonal plasma flow pattern can be explained by the so-called F region dynamo. Looking at Fig. 2.10, one can see a region of increased Pedersen conductivity between 300 and 600 km altitude. As a first order approximation, one can consider a zonal eastward wind whose magnitude is height independent and a discrete layer of Pedersen conductivity at F region heights. The eastward wind would drive an upward Pedersen current within the Pedersen conductivity layer. Positive (negative) charges would accumulate in the upper (lower) boundaries of the Pedersen layer, and a downward polarization electric field would be created. A polarization electric field in the opposite direction (upward) would then be generated during the day when the zonal wind is eastward. The magnitude of the vertical electric field would be $|\mathbf{E}_p| = |\mathbf{U}_z||\mathbf{B}|$, and the zonal plasma drift speed would be $|\mathbf{V}_e| = |\mathbf{V}_i| = \frac{|\mathbf{E}_p|}{|\mathbf{B}|} = |\mathbf{U}_z|$, where \mathbf{U}_z is the zonal neutral wind velocity.

This simple scenario explains the overall pattern of the zonal plasma flow in the F region, but not entirely. The plasma velocity is significantly slower than the neutral velocity during daytime. This is primarily because the simple model

assumed only a conducting F region. A conducting E region exists during the day and the vertical currents generated by winds in the equatorial F region are partially shorted out by this layer. Considering a conducting E layer in the conjugate points of the magnetic field line that passes at an altitude z in the magnetic equator leads to the following expression for the magnitude of the upward electric field at the magnetic equator:

$$|\mathbf{E}_p(z)| = -\frac{\sum_P^F(z)}{\sum_P^F(z) + 2 \sum_P^E(z)} |\mathbf{B}| |\mathbf{U}_z(z)| \quad (2.38)$$

where $\sum_P^F(z)$ and $\sum_P^E(z)$ are the F and E region Pedersen conductivities, respectively, integrated along the magnetic field line. At night, the E region conductivity is negligible compared to F region values. Therefore, $|\mathbf{V}_p| \approx |\mathbf{U}_z|$. During the day, the E region conductivity is not negligible, and the plasma velocity is significantly slower than the wind velocity.

2.5.2 Vertical shear in the zonal plasma flow

The magnitude of the zonal plasma drift in the equatorial ionosphere is approximately constant with height for most of the day, except around sunset hours (Fejer, 1981). Around this time, numerical models of the ionosphere and measurements show that the plasma moves in the westward direction in the bottom-side F-region, while an eastward plasma motion is observed around the F peak. The configuration described in the previous section explains the main features of the zonal plasma flow. This configuration, however, is not complete enough to explain all the dynamic features observed in the equatorial plasma flow.

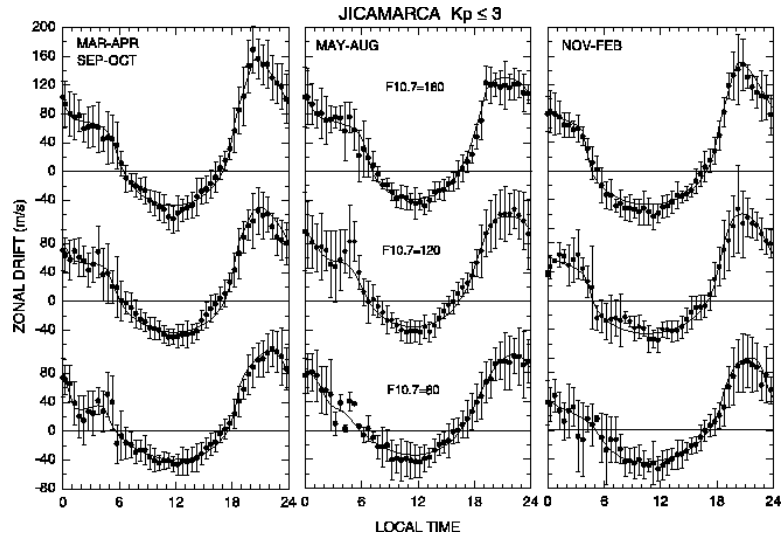


Figure 2.11: Quiet-time zonal plasma drifts measured at Jicamarca for different seasons and solar flux conditions. After *Fejer et al. (2005)*. Reproduced by permission of American Geophysical Union.

The results of *Haerendel et al. (1992)* from a time-dependent model of electric fields in the equatorial ionosphere shows vortex-like motion of the plasma around sunset hours. Advanced radar observations of plasma drifts have confirmed the numerical simulations (*Kudeki and Bhattacharyya, 1999*). The plasma vortex is formed by the enhanced vertical motion of the plasma starting before sunset, a shear in the zonal plasma flow around sunset time, and the downward plasma flow during post-sunset hours. This vortex motion suggests a divergent electric field at F region heights similar to what would be produced by an accumulation of negative charges. Chapter 6 describes radar imaging observations of F region density irregularities whose generation is associated with the vertical shear in the zonal plasma flow.

2.5.3 Vertical plasma drifts

It was assumed in the previous sections that neutral winds were primarily horizontal. However, a small but important vertical component exists due to the thermal expansion of the neutral gas heated by solar radiation in the dayside hemisphere. This diurnal upward component of neutral motion drives a westward Pedersen current in both E and F regions. This current would create negative (positive) charge accumulation in the dawn (dusk) terminator. Again, an eastward (westward) polarization electric field will be created in the dayside (nighttime) hemisphere driving a Pedersen current that will oppose charge accumulation. This dawn-to-dusk electric field is weaker than the vertical F region electric field but it is very important for the plasma transport in the low-latitude ionosphere.

Fig. 2.12 shows the results of a statistical study of the vertical plasma drifts using radar and satellite observations for four longitude sectors. The drifts are upward during the day and downward at night, indicating an eastward (westward) electric field in the dayside (nightside) hemisphere. The daily variation pattern is similar for all the longitude sectors and seasons, but the magnitude of the drifts is longitude as well as season dependent. The magnitude of vertical drifts is also highly dependent on the solar activity. Larger drifts are observed during periods of high solar flux (e.g. *Fejer, 1991*).

2.5.4 Pre-reversal enhancement of the zonal electric field

Fig. 2.12 shows that the vertical plasma drift is enhanced before its reversal around sunset hours. This enhancement in the vertical drift is caused by the

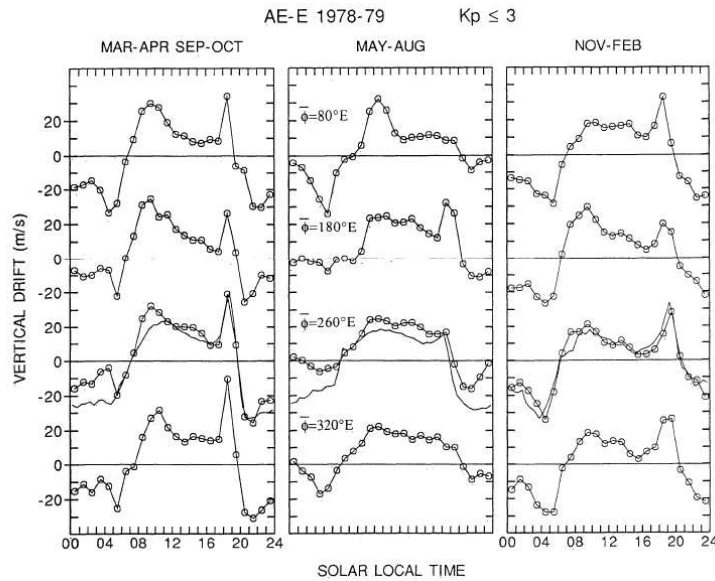


Figure 2.12: Averages of vertical plasma drifts measured by the AE-E satellite for different seasons and longitude sectors. After *Fejer et al. (1995)*. Reproduced by permission of American Geophysical Union.

enhancement in the zonal electric field. It is a well known phenomenon of the equatorial ionosphere and it is usually referred to as the pre-reversal enhancement (PRE).

An enhancement in the vertical electric field in the evening was first suggested by *Rishbeth (1971)*. *Rishbeth (1971)* also offered the first explanation for the PRE. He suggested that the PRE would be a direct result of the large eastward neutral winds and large vertical electric fields around sunset. Large horizontal electric fields would appear to maintain the $\nabla \times \mathbf{E} = 0$ condition in the evening equatorial ionosphere. This suggests a connection between large PRE and strong vertical shears in zonal plasma flow in the equatorial ionosphere. A positive correlation between the PRE and the shear has been pointed out by *Kudeki et al. (1999)*.

The mechanism for the generation of the PRE that is more widely referenced was proposed by *Farley et al.* (1986). The eastward neutral winds in the equatorial F region drive a downward Pedersen current. No winds in the E region or meridional winds were assumed. Due to vertical gradients in the Pedersen conductivity, an upward electric field is set up in the F region and maps along magnetic field lines to the E region of low latitudes. After sunset, the density of the E region is very low, and so is the Hall conductivity. This creates a strong westward gradient in the conductivity across the terminator in E region. Consequently, negative charges are accumulated in the terminator causing an enhancement of the zonal electric field just before sunset.

More recently, *Haerendel and Eccles* (1992) proposed that the equatorial electrojet current system plays an important role in the PRE. The equatorial electrojet is a strong eastward current system in the equatorial E region. They suggested that the vertical current demand created by the F region neutral wind dynamo after sunset hours would be supplied by the dayside electrojet. In order to meet the demand of vertical currents in the nightside F region, enhanced horizontal electric fields would be required to draw this current from the day-side.

2.5.5 The equatorial fountain effect

At the equator, the zonal electric field moves the ionospheric plasma upward during the day. At some point in altitude, gravity and pressure gradient forces start to dominate and the plasma starts to diffuse along geomagnetic field lines. This causes the transport of equatorial plasma to low magnetic latitudes known

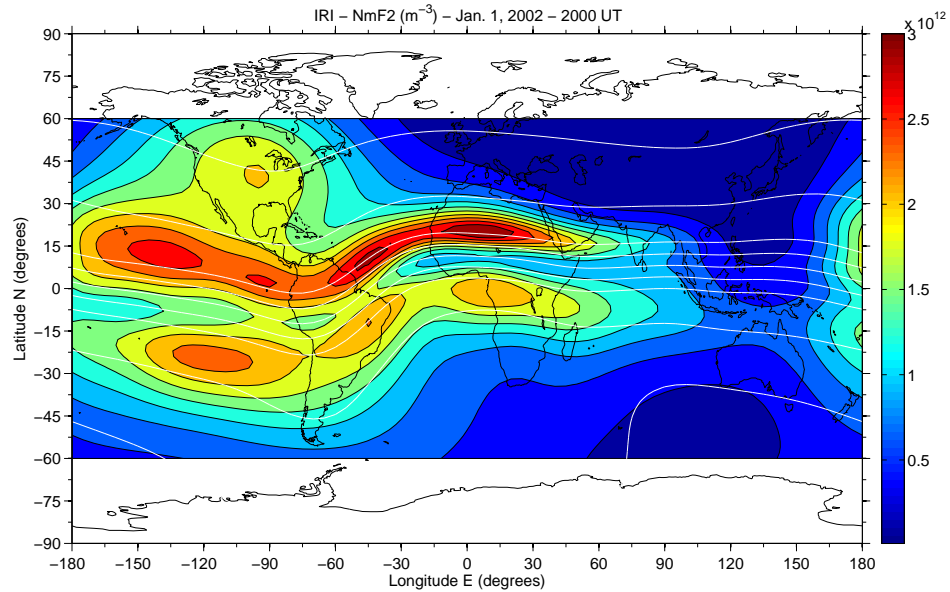


Figure 2.13: Global map of the maximum density of the ionospheric F_2 region (NmF2). Values of NmF2 were calculated using the International Reference Ionosphere (IRI) model.

as the *fountain effect*. The fountain effect is responsible for the large values of electron density observed around $\pm 30^\circ$ magnetic latitude ($\sim 15^\circ$ dip latitude). Fig. 2.13 shows a global map of peak density of the F_2 layer (NmF2), obtained from a numerical model (IRI 2005). It is possible to observe two regions of increased density around the magnetic equator. The northern density crests are larger due to the action of neutral wind towards the North during the south hemisphere summer months. These density crests are known as the Equatorial or Appleton anomaly. The large horizontal density gradients in Equatorial Anomaly are difficult to model. Also, the strongest ionospheric (amplitude) scintillations are observed near the peak of the Anomaly (e.g. *Aarons, 1982*).

2.5.6 Equatorial spread F

The large nighttime uplifts driven by the PRE cause an additional transport of plasma from the magnetic equator to low-latitude regions which enhances the Appleton Anomaly and the latitudinal density gradients in the low-latitude ionosphere. Besides these latitudinal gradients, sharp plasma depletions aligned with the magnetic meridian have also been observed in the low-latitude ionosphere. Irregularities in the ionospheric plasma density were first noticed in vertical radio soundings of the ionosphere using the so-called ionosondes (*Booker and Wells, 1938*). The presence of large-scale density irregularities in the ionosphere causes spreading in ionogram traces. Spread in the traces around F region heights gave origin to the general name “equatorial spread F ”, which is now used to indicate a class of F region irregularities.

The plasma depletions observed at low latitudes are also referred to as ionospheric “plasma bubbles”. Signatures of plasma bubbles in coherent scatter radar observations are also known as radar plumes. Observations based on radio soundings of the ionosphere indicate that the plasma depletions start in the bottomside F region, develop vertically, and can reach the topside F region. As these depletions develop vertically at the magnetic equator, they also diffuse along geomagnetic field lines reaching low latitudes. Observations have shown that plasma bubbles can extend over several hundreds of km in the magnetic East-West direction and can easily exceed 1000 km in altitude. During their generation, plasma bubbles rise upwards with large velocities, generating a broad range of smaller scale size irregularities through nonlinear processes. Irregularities with scale sizes as short as only a few cm can be observed during spread F events (e.g. *Tsunoda, 1980*).

Spread F has been extensively studied both experimentally and theoretically. Spread F density irregularities are a result of plasma instabilities in the ionosphere. These irregularities can cause rapid and sharp changes in the index of refraction of the ionospheric medium, which in turn cause scattering, diffraction and/or multiple reflection of transionospheric radio waves. Therefore, signatures of spread F irregularities can be seen in measurements made by radio-based instruments for ionospheric sounding (e.g. *Woodman and LaHoz, 1976; Abdu et al., 1998; Hysell and Burcham, 1998a*) and in-situ measurements by plasma sensors onboard satellites (e.g. *Kil and Heelis, 1998; Gentile et al., 2006*) and rockets (e.g. *Abdu et al., 1991; Jahn and LaBelle, 1997*). Spread F is responsible for strong amplitude scintillation of satellite signals observed at low latitudes.

Spread F can also be observed by optical instruments capable of measuring spontaneous emissions (airglow) from metastable oxygen atoms at ionospheric heights (e.g. *Mendillo and Baumgardner, 1982; Sobral et al., 2002; Makela and Kelley, 2003*). More recently, global observations of ionospheric plasma bubbles were made possible through measurements of naturally-occurring optical emissions detected by an ultra-violet sensor (Global Ultra-Violet Instrument - GUVI) onboard of the TIMED (Thermosphere Ionosphere Mesosphere Energetics and Dynamics) satellite (e.g. *Christensen et al., 2003*). In general, the intensity of the optical emission is proportional to electron density and plasma bubble signatures appear as regions of low emission in the optical observations. A study on the generation of large-scale waves in the bottomside F region and observations suggesting their causal relationship with spread F is presented in Chapter 6.

CHAPTER 3

RADAR REMOTE SENSING OF THE IONOSPHERE

3.1 Introduction

The scattering of radio waves by electrons has been used to study the ionosphere for over 50 years. The quiescent ionosphere is a soft, overspread target, and active radar (Radio Detection and Ranging) systems are generally used for its remote sensing. More recently, passive radar systems were developed and are now used in ionospheric studies (e.g. *Sahr et al.*, 2001). Radars are convenient instruments for ionospheric observations. They can be operated continuously and, in some cases, remotely. They can provide height profiles of ionospheric parameters as a function of time and have obvious advantages over satellite and rocket measurements. In some cases, radars can be equipped with steerable antennas or multiple antenna baselines and can provide two-or-three dimensional information about the ionosphere. In this dissertation, ionospheric observations made with the Jicamarca incoherent backscatter radar in Peru (Chapters 4 and 5) and with the coherent backscatter radar in São Luís in Brazil (Chapter 6) are presented and discussed. This chapter gives a short introduction about these two distinct radar techniques and it is based on various articles describing the scattering of radio waves from the ionosphere (e.g. *Doughery and Farley*, 1960; *Woodman and Hagfors*, 1969; *Bauer*, 1975; *Beynon and Williams*, 1978; *Farley and Hagfors*, 2005). The reader familiar with incoherent and coherent scatter radar techniques is encouraged to skip this chapter.

3.2 Scattering of radio waves in the ionosphere

Thomson (1906) described the scattering mechanism of electromagnetic radiation by free electrons. Two decades later, *Fabry* (1928) suggested that ionospheric electrons could cause significant scattering of radio waves. In the late 50s, *Gordon* (1958) figured out that contemporary radar systems were sufficiently technologically advanced to be able to detect the scattering of radio waves by electrons in the ionosphere. At that time, only radio sounding of the ionospheric region below the F peak was possible by ionosondes.

Gordon's idea would allow the measurement of the entire ionospheric density profile. Gordon assumed that electrons would be independent scatterers, and his radio sounding technique became known as *incoherent scattering*. Backscattered power profiles would be proportional to electron density profiles. Also, based on the assumption that the electron scattering was completely random, Gordon predicted that the spectral width of the echoes would be proportional to the electron temperature.

The first observations made by *Bowles* (1958) showed that detection of incoherent scatter was possible. However, the spectral width of the echoes was much narrower than expected. The narrowing is due to Coulomb interactions between ions and electrons. The unexpected narrowing of the incoherent scattering spectrum was explained in the following years by a number of investigators working independently (e.g. *Dougherty and Farley*, 1960; *Salpeter*, 1961; *Fejer*, 1961; *Hagfors*, 1961).

3.2.1 Scattering by a single electron

An oscillating electron will radiate electromagnetic radiation at the frequency of its oscillation. The electric field of an incident radio wave, transmitted by a radar for instance, will cause oscillatory motion in the electron, and part of the wave energy will be transferred to the electron and subsequently radiated by the particle. This is the basis of scattering electromagnetic radiation by free electrons. The momentum equation for an electron under the action of an electric field $\mathbf{E}_i(r, t)$ of an incident electromagnetic wave is:

$$\dot{\mathbf{u}}_e = -\frac{e}{m_e}\mathbf{E}_i(r, t) \quad (3.1)$$

where $\dot{\mathbf{u}}_e$ is the electron acceleration, m_e is the electron mass, and e is the modulus of the electron charge. For a non-relativistic electron motion, the scattered electric field \mathbf{E}_s at a point \mathbf{r}_s far from the origin is given by:

$$\mathbf{E}_s(\mathbf{r}_s, t) = -\frac{e\mu_0}{4\pi r_s^3}\mathbf{r}_s \times [\mathbf{r}_s \times \dot{\mathbf{u}}_e(t')] \quad (3.2)$$

where, μ_0 is the permeability of free space, $t' = t - |\mathbf{r}_s|/c$ is a retarded time, and c is the speed of light. The magnitude of the scattered field at a given position can be written in terms of the incident electric field:

$$E_s(\mathbf{r}_s, t) = \frac{r_e}{r_s} \sin \chi E_i(0, t') \quad (3.3)$$

where, $r_e = e^2\mu_0/4\pi m_e$ is the classical electron radius and χ is a polarization

angle.

3.2.2 Scattering from a distribution of electrons

The electric field resulting from scattering by a distribution of electrons can be obtained by summing the scattering contributions of individual electrons. Fig. 3.1 shows the geometry for this calculation, which is generalized for the case of a bistatic radar experiment. The transmitter and receiver are represented by Tx and Rx, respectively. The scattering volume is represented by the shaded area in the figure.

The origin of the coordinate system for this calculation is chosen to be in the center of the scattering volume. The scattering volume is defined by the beam shape of the transmitting and receiving antennas and by the transmitted pulse length. The position of a given scattering electron within the volume is given by the vector \mathbf{r}_p . The transmitter and receiver are located at positions $-\mathbf{R}_i$ and \mathbf{R}_s , respectively.

Considering the scattering volume to be small compared to $|\mathbf{R}_i|$ and $|\mathbf{R}_s|$, the amplitude of the incident electric field can be assumed to be constant within the volume and equal to E_0 . The distance of the scattering volume is far enough that the incident field can be modelled as that of a plane wave ($E_0 e^{-i(\omega_0 t - \mathbf{k}_i \cdot \mathbf{r}_i)}$). The complex amplitude of the electric field scattered by a single electron located at a position \mathbf{r}_p within the volume will be given by:

$$E_s(\mathbf{r}_s, t) = \frac{r_e}{|\mathbf{R}_s - \mathbf{r}_p|} \sin \chi E_0 e^{-i(\omega_0 t' - \mathbf{k}_i \cdot \mathbf{r}_i)} \quad (3.4)$$

The total phase of the wave scattered by an electron at the position \mathbf{r}_p and received at \mathbf{R}_s can be written as:

$$\phi(t') = [\omega_0 t' - (\mathbf{k}_i - \mathbf{k}_s) \cdot \mathbf{r}_p] - (\mathbf{k}_i \cdot \mathbf{R}_i + \mathbf{k}_s \cdot \mathbf{R}_s) \quad (3.5)$$

The last term in the above equation is a constant and does not have implications for the description of the total scattered electric field. To make the equations more readable, this term will be dropped in the following text. Also, the dimensions of the scattering volume are considered small compared to the distance to the receiving system ($V^{1/3} \ll |\mathbf{R}_s|$) making it possible to write $|\mathbf{R}_s - \mathbf{r}_p| \sim R_s$. The scattered electric field is then described by:

$$E_s(\mathbf{r}_s, t) = \frac{r_e}{R_s} \sin \chi E_0 e^{-i[\omega_0 t' - (\mathbf{k}_i - \mathbf{k}_s) \cdot \mathbf{r}_p]} \quad (3.6)$$

Defining the Bragg wavevector to be $\mathbf{k} = \mathbf{k}_s - \mathbf{k}_i$, the total electric field scattered by the electron distribution within the volume V can then be computed from:

$$E_s(\mathbf{r}_s, t) = \frac{r_e}{R_s} \sin \chi E_0 e^{-i\omega_0 t} \int_V N(\mathbf{r}, t) e^{-i\mathbf{k} \cdot \mathbf{r}} d^3 \mathbf{r} \quad (3.7)$$

where the integral is over the scattering volume and the small time difference $t - t'$ has been neglected.

The electron number density $N(\mathbf{r}, t)$ in the illuminated volume can be seen as a quantity that fluctuates with respect to a mean value:

$$N(\mathbf{r}, t) = \langle N \rangle + \Delta N(\mathbf{r}, t) \quad (3.8)$$

The mean value $\langle N \rangle$ contributes to the integral in Eq. 3.7 only for the case of $\mathbf{k} = 0$. Since \mathbf{k} is a non-zero quantity, the mean value term can be dropped, and Eq. 3.7 becomes:

$$E_s(\mathbf{r}_s, t) = \frac{r_e}{R_s} \sin \chi E_0 e^{-i\omega_0 t} \int_V \Delta N(\mathbf{r}, t) e^{-i\mathbf{k}\cdot\mathbf{r}} d^3\mathbf{r} \quad (3.9)$$

The integral acts as a spatial Fourier transform of the density fluctuations within the volume, and an expression for the scattered electric field can be written as:

$$E_s(\mathbf{r}_s, t) = \frac{r_e}{R_s} \sin \chi E_0 e^{-i\omega_0 t} \Delta N(\mathbf{k}, t) \quad (3.10)$$

3.3 Signal statistics

The product of the scattered electric field at two distinct times spaced by τ seconds can be written as:

$$E_s(\mathbf{k}, t) E_s^*(\mathbf{k}, t + \tau) = \left(\frac{E_0 r_e \sin \chi}{R_s} \right)^2 e^{-i\omega_0 \tau} \int_V \int_V \Delta N(\mathbf{r}, t) \Delta N^*(\mathbf{r}', t + \tau) e^{-i\mathbf{k}\cdot(\mathbf{r}-\mathbf{r}')} d\mathbf{r}^3 d\mathbf{r}'^3 \quad (3.11)$$

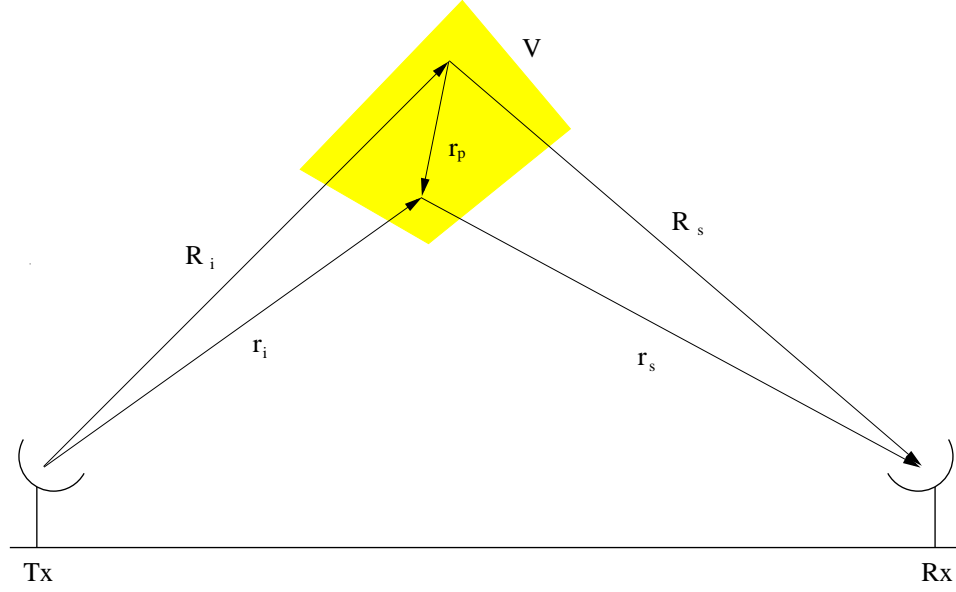


Figure 3.1: Scattering geometry for a bistatic radar. The location \mathbf{r}_p of a particular electron is indicated.

A small change of variables $\mathbf{r}' = \mathbf{r} + \mathbf{r}''$ yields:

$$E_s(\mathbf{k}, t)E_s^*(\mathbf{k}, t + \tau) = \left(\frac{E_0 r_e \sin \chi}{R_s} \right)^2 e^{-i\omega_0 \tau} \int_V \int_V \Delta N(\mathbf{r}, t) \Delta N^*(\mathbf{r} + \mathbf{r}'', t + \tau) e^{-i\mathbf{k} \cdot (\mathbf{r}'')} d\mathbf{r}^3 d\mathbf{r}''^3 \quad (3.12)$$

The density fluctuations are random in space and time, and the measured electric fields will be random variables. Therefore, an unique realization of the electric field product is not useful. The ensemble average of this product, on the other hand, is a useful statistical measure. In practice, the ensemble average is approximated by a time average with a large number of samples.

$$\begin{aligned} \langle E_s(\mathbf{k}, t) E_s^*(\mathbf{k}, t + \tau) \rangle = & \\ \left(\frac{E_0 r_e \sin \chi}{R_s} \right)^2 e^{-i\omega_0 \tau} \int_V \int_V \langle \Delta N(\mathbf{r}, t) \Delta N^*(\mathbf{r} + \mathbf{r}'', t + \tau) \rangle e^{-i\mathbf{k} \cdot \mathbf{r}''} d\mathbf{r}^3 d\mathbf{r}''^3 & \end{aligned} \quad (3.13)$$

where,

$$R_N(\mathbf{r}, t; \mathbf{r}'', \tau) = \langle \Delta N(\mathbf{r}, t) \Delta N^*(\mathbf{r} + \mathbf{r}'', t + \tau) \rangle \quad (3.14)$$

is the time and space autocorrelation function of the density fluctuations. If the medium within the scattering volume is homogeneous and stationary, the autocorrelation will only depend on the time and space increments (τ and \mathbf{r}''), and the two integrals can be separated:

$$\begin{aligned} \langle E_s(\mathbf{k}, t) E_s^*(\mathbf{k}, t + \tau) \rangle &= \left(\frac{E_0 r_e \sin \chi}{R_s} \right)^2 e^{-i\omega_0 \tau} \int_V \int_V R_N(\mathbf{r}'', \tau) e^{-i\mathbf{k} \cdot \mathbf{r}''} d\mathbf{r}^3 d\mathbf{r}''^3 \\ &= \left(\frac{E_0 r_e \sin \chi}{R_s} \right)^2 e^{-i\omega_0 \tau} \int_V d\mathbf{r}^3 \int_V R_N(\mathbf{r}'', \tau) e^{-i\mathbf{k} \cdot \mathbf{r}''} d\mathbf{r}''^3 \\ &= \left(\frac{E_0 r_e \sin \chi}{R_s} \right)^2 e^{-i\omega_0 \tau} V \int_V R_N(\mathbf{r}'', \tau) e^{-i\mathbf{k} \cdot \mathbf{r}''} d\mathbf{r}''^3 \end{aligned} \quad (3.15)$$

where the integral in the last expression is the spatial Fourier transform of the autocorrelation function of the density fluctuations, $\langle |N(\mathbf{k}, \tau)|^2 \rangle$. The Δ symbol is dropped in the following text to be in accordance with more conventional notation. The autocorrelation function of the scattered electric field can be written as:

$$\langle |E_s(\mathbf{k}, \tau)|^2 \rangle = \left(\frac{E_0 r_e \sin \chi}{R_s} \right)^2 e^{-i\omega_0 \tau} V \langle |N(\mathbf{k}, \tau)|^2 \rangle \quad (3.16)$$

The power spectrum of the scattered electric field can be obtained from the Fourier Transform of Eq. 3.16:

$$\langle |E_s(\mathbf{k}, \omega_0 + \omega)|^2 \rangle = \left(\frac{E_0 r_e \sin \chi}{R_s} \right)^2 V \langle |N(\mathbf{k}, \omega)|^2 \rangle \quad (3.17)$$

This last result states that the power spectrum of the electric field detected by a radar is a scaled version of the Doppler spectrum of electron density fluctuations matching the Bragg condition in the volume illuminated by the radar.

3.4 Incoherent scatter of radio waves

Following the first incoherent scatter observations, several investigators started to work on the spectrum of density fluctuations in the ionosphere that would explain the narrow spectrum detected by *Bowles* (1958). They used different approaches but obtained equivalent results (e.g. *Doughery and Farley*, 1960; *Salpeter*, 1961; *Fejer*, 1961; *Hagfors*, 1961). *Doughery and Farley* (1960) used the Fluctuation-Dissipation (or Generalized Nyquist theorem) to derive the IS spectrum for a magnetized plasma in thermal equilibrium ($T_e = T_i$). A series of papers using the same approach but investigating more complex plasma conditions were published in the following years. *Farley et al.* (1961), for instance, included the effects of a background magnetic field. The effect of neutral-ion collisions which

are important in the lower ionosphere was investigated by *Dougherty and Farley* (1963), and the effects of unequal electron and ion temperatures were derived in *Farley* (1966a) and elsewhere.

3.4.1 The spectrum of thermal density fluctuations

Swartz and Farley (1979) summarized the spectrum of thermal electron density fluctuations (IS spectrum) for a magnetized plasma containing a mixture of ions in quasi-equilibrium. The spectrum is written in terms of normalized admittance functions for the ionized species forming the plasma:

$$\langle |n_e(\mathbf{k}, \omega)|^2 \rangle = \frac{2N_e |y_e|^2 \sum_j n_j \text{Re}(y_j) + |\sum_j \mu_j y_j + i\lambda_{De}^2 k^2|^2 \text{Re}(y_e)}{\omega |y_e + \sum_j \mu_j y_j + i\lambda_{De}^2 k^2|^2} \quad (3.18)$$

where, $\langle |n_e(\mathbf{k}, \omega)|^2 \rangle = \langle |N(\mathbf{k}, \omega)|^2 \rangle$, N_e is the electron density, $\lambda_{De} = \left(\frac{\epsilon_0 K_B T_e}{N_e e^2} \right)^{1/2}$ is the electron Debye length, k is the scattering wave number, y_j is the normalized ion admittance function, y_e is the normalized electron admittance function, $n_j = N_j/N_e$ is the fraction density for each ion species, and $\mu_j = T_j/T_e$ is the ratio of the ion temperature T_j to electron temperature T_e . Note that $i^2 = -1$ and j is a subscript that refers to each ion species.

The admittance function for species s is given by (e.g. *Dougherty and Farley*, 1963):

$$y_s = \frac{i + (\theta_s - i\psi_{sn})J_s}{1 - \psi_{sn}J_s} \quad (3.19)$$

where J_s is the so-called Gordeyev integral:

$$J_s(\theta - i\psi_{sn}, \phi, \alpha) = \int_0^\infty dt e^{-i(\theta_s - i\psi_{sn})t - \phi_s^{-2} \cos^2 \alpha \sin^2(0.5\phi_s t) - 0.25t^2 \sin^2 \alpha} \quad (3.20)$$

and, α is the aspect angle and $\theta_s, \psi_{sn}, \phi_s$ are normalized frequencies given by:

$$\begin{aligned} \theta_s &= \frac{\omega}{\sqrt{2}kC_s} \\ \phi_s &= \frac{\Omega_s}{\sqrt{2}kC_s} \\ \psi_s &= \frac{\nu_{sn}}{\sqrt{2}kC_s} \end{aligned}$$

where $C_s = \sqrt{\frac{k_B T_s}{m_s}}$, ω is the spectral angular frequency offset, $\Omega_s = \frac{eB}{m_s}$ is the gyrofrequency, and ν_{sn} is the collision frequency of ionized species s with neutrals.

The Gordeyev integral can be seen as an one-sided Fourier transform of a single particle correlation function $C(\mathbf{k}, \omega)$ (*Hagfors and Brockelman, 1971; Sulzer and González, 1999*):

$$\begin{aligned} J(\mathbf{k}, \omega) &= C(\mathbf{k}, \omega) = \int_0^\infty d\tau C(\mathbf{k}, \tau) e^{i\omega\tau} \\ &= \int_0^\infty d\tau e^{i\omega\tau} \int d\mathbf{v}^3 f_0(\mathbf{v}) e^{-i\mathbf{k}\cdot\mathbf{v}\tau} \end{aligned} \quad (3.21)$$

Therefore, the Gordeyev integral can be estimated from numerical simulations of the motion of the plasma species. Recently, *Sulzer and González (1999)* used

this approach to investigate the electron Gordeyev integral. They have shown that electron Coulomb collisions are important at small aspect angles. The results of *Sulzer and González (1999)* are used in Chapters 4 and 5 to analyze radar observations at small aspect angles.

3.4.2 Short and long wavelength regimes

Eq. 3.18 is a theoretical model of the spectrum of electron fluctuations with wavevector \mathbf{k} in a plasma. In general, two different regimes are of particular interest: $k^2\lambda_{De}^2 \ll 1$ and $k^2\lambda_{De}^2 \gg 1$. For $k^2\lambda_{De}^2 \gg 1$, the wavelengths considered are small compared with the Debye length. In this case, electrons can be assumed to be independent particles with random velocities. Any collective motion can be neglected. The width of the spectrum is determined by the electron thermal velocity. This is the regime of interest in experiments of laboratory plasmas. In this case, incoherent scattering (or Thomson scattering) is used to estimate electron temperatures and densities of confined plasmas using laser beams. In ionospheric radar observations, where VHF or UHF radio waves are used, the regime where $k^2\lambda_{De}^2 \ll 1$ applies.

3.4.3 Long wavelength regime: The ion and plasma lines

In the case where $k^2\lambda_{De}^2 \ll 1$, the wavelength considered is much longer than the Debye length. In this case, interactions between electrons and ions in the plasma must be taken into consideration. The interaction leads to a collective behavior of the particles forming the plasma, and the development of electro-

static plasma waves. At least two modes of naturally occurring waves exist in a plasma and are responsible for the scattering of radio waves; they are ion acoustic and electron (Langmuir) waves (e.g. *Chen, 1984*). Ion acoustic waves are slow plasma waves caused by ion thermal fluctuations. To maintain plasma quasi-neutrality, electron clouds follow the ions. Much more mobile than ions, electrons are responsible for the wave scattering. Langmuir waves, on the other hand, are faster waves and are caused by electron thermal fluctuations.

In most of IS radar experiments, only scattering from ion acoustic waves is considered. The low frequency portion of the spectrum formed by these waves is referred to as the “ion line”, even though it is not really a spectral line. Fig. 3.2 shows some examples of the ion line calculated for plasmas with different temperatures and ion compositions. The overall shape of the ion line can be explained in terms of the ion thermal velocity and Landau damping effects. In this dissertation, the ion line is referred to simply as the IS spectrum unless otherwise noted.

Fig. 3.3 shows another example of the incoherent scatter spectra as predicted by Eq. 4.1. In this case, the spectrum is computed for higher frequencies, and for both long ($k^2 \lambda_{De}^2 \gg 1$) and short ($k^2 \lambda_{De}^2 \ll 1$) wavelengths. In the long wavelength case, the plasma line can be identified. In the short wavelength case, the plasma line is absent and the spectrum is much broader, as explained earlier.

3.4.4 Estimation of plasma parameters

Ionospheric parameters are estimated by finding theoretical IS spectra that best fit the radar measurements. It is common practice to measure the autocorrela-

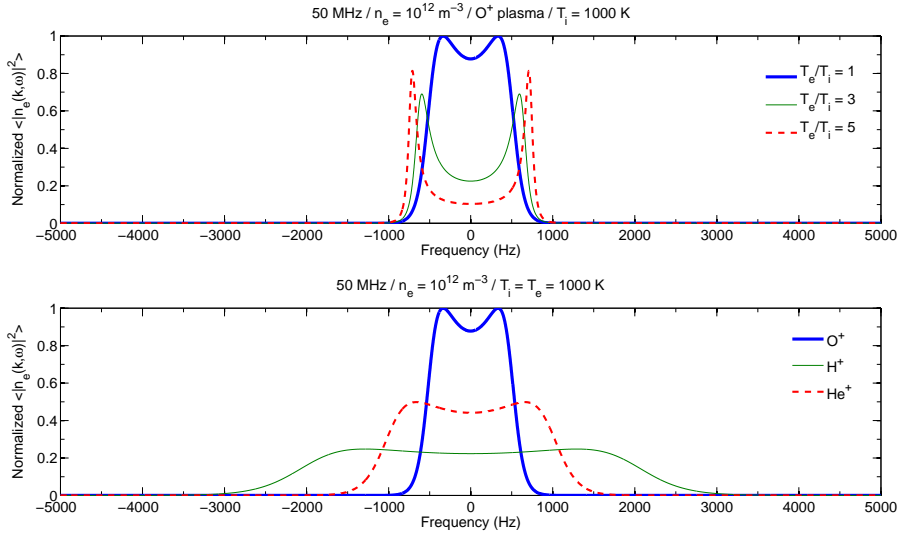


Figure 3.2: Ion line computed for different values of electron-to-ion temperature ratio (top panel) and different ion compositions (single ion species considered in all cases).

tion function (ACF) of the signal instead of the power spectrum. The spectrum and the ACF contain equivalent information. The fitting routines take into consideration the uncertainties in the measurements. These uncertainties can be estimated for different pulse schemes used in the observations. A detailed explanation on how to calculate the uncertainties for different ACF estimators is given by *Farley (1969a)*.

The shape of the ion line depends on several plasma parameters as illustrated in Fig. 3.2. The velocity of ion acoustic waves increases with the temperature and so does the spectral width of the ion line. A similar effect is found when lighter ions are included in the composition of the plasma. The ion composition/temperature effects are not ambiguous when the mass of the ions are considerably different. For instance, estimates of He^+ , H^+ and O^+ can be distinguished in the measurements (e.g. *González and Sulzer, 1996*). For a given

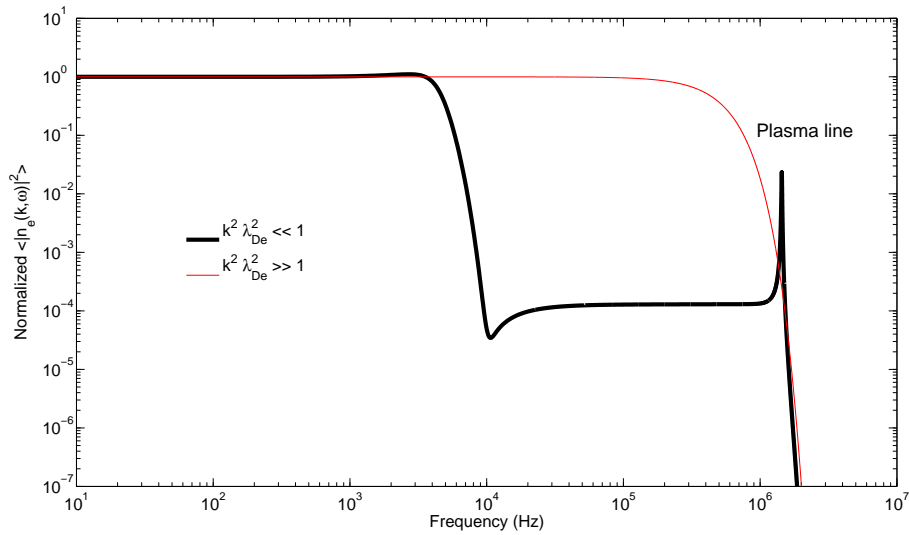


Figure 3.3: Examples of IS spectra for short and long wavelength regimes. The calculations were made for an UHF radar. The plasma line is the narrow spectral line around 2 MHz.

ion temperature, Landau damping effects are reduced at larger electron-to-ion ratios (T_e/T_i), and a spectral line starts to develop at the ion acoustic velocity.

3.5 Coherent scatter of radio waves

The development of the IS radar technique and the first observations lead to the discovery of small-scale, non-thermal fluctuations in the ionosphere. It is now known that these fluctuations can be generated by a number of different plasma instabilities and have amplitudes that can cause radar echoes as strong as 50 dB above the thermal level. This makes possible the use of relatively small and inexpensive radars for their study. Such radars are referred to as coherent scatter radars.

Due to the high diffusivity in the direction of the geomagnetic field, density perturbations with wavevectors parallel to magnetic field diffuse very quickly. Only density fluctuations with wavevectors perpendicular to the geomagnetic field (so called field-aligned irregularities) can survive and be detected in radar soundings. Therefore, detection of such irregularities requires the radar to be pointing perpendicular to the geomagnetic field. *Farley and Hysell (1996)* designed an interferometric radar experiment to accurately measure very small aspect angles at Jicamarca and used it to estimate the degree of alignment of spread F density irregularities. The results of their experiment showed that the rms deviation from perfect alignment can be as small as 0.0075° .

There is no mathematical model relating the spectrum of coherent echoes to macroscopic ionospheric parameters. It is common practice, however, to associate the first moment of the spectrum of coherent echoes with the bulk motion of the electrons in the radar scattering volume. It is also common to associate the second moment of the spectrum to the strength of the plasma turbulence. These assumptions, however, have no theoretical grounds and are based on a limited set of examples of coherent backscatter spectra. *Hysell (1992)* and *Hysell and Farley (1996b)* pointed out that the Doppler shift of coherent echoes might represent the motion of the scattering layer and perhaps of the background plasma during spread F events that are not very turbulent. During well developed radar plumes, wide spectra centered at abnormally high Doppler shift values are observed that might be a result of high-speed plasma eddies in the highly turbulent flow associated with the plume development. In the particular case of spread F , the spectral shape of the echoes can vary significantly from time to time and/or from range gate to range gate making the interpretation of these echoes difficult (e.g. *Woodman and LaHoz, 1976*).

An interesting type of coherent echoes comes from the valley region (~ 150 km) in the equatorial ionosphere. It was shown that these echoes have Doppler shifts corresponding to the background plasma velocity, and they are currently used at Jicamarca and elsewhere for accurate estimates of the vertical plasma drift of the F region during daytime hours when they are observed (*Kudeki and Fawcett, 1993; Chau and Woodman, 2004*). Despite its usefulness for drift measurements, the generation mechanism of the 150-km echoes is not understood. They serve, however, as an example of the importance of coherent scatter radar studies.

3.6 Propagation of radio waves in the ionosphere

Magneto-ionic theory describes the propagation of electromagnetic waves in a magnetized cold plasma (*Ratcliffe, 1959*). In this case, the Appleton-Hartree equation provides the index of refraction n given various parameters of the plasma:

$$n^2 = (\mu + j\chi)^2$$

$$n^2 = 1 - \frac{X}{1 - jZ - \frac{Y_T^2}{2(1-X-jZ)} \pm \left[\frac{Y_T^4}{4(1-X-jZ)^2} + Y_L^2 \right]^{1/2}} \quad (3.22)$$

Normalized parameters in the Appleton-Hartree equation are defined as:

$$X = \frac{\omega_p^2}{\omega^2} \quad (3.23)$$

$$Y_L = \frac{\Omega_e}{\omega} \cos \theta \quad (3.24)$$

$$Y_T = \frac{\Omega_e}{\omega} \sin \theta \quad (3.25)$$

$$Z_T = \frac{\nu}{\omega} \quad (3.26)$$

where ω is the angular frequency of the electromagnetic wave, $\omega_p = \left(\frac{n_e e^2}{\epsilon_0 m_e}\right)^{1/2}$ is the electron plasma frequency, $\Omega_e = \frac{eB}{m_e}$ is the electron gyrofrequency, θ is the angle between the wavevector of the electromagnetic wave and the direction of the background magnetic field B ($\theta = 90^\circ - \alpha$), and ν is the collision frequency of the electrons with neutral particles (*Ratcliffe, 1959*). In general, the working frequency of ionospheric radars is sufficiently high that the collision term can be neglected ($Z \sim 0$), and Eq. 3.22 becomes:

$$n^2 = 1 - \frac{X}{1 - \frac{Y_T^2}{2(1-X)} \pm \left[\frac{Y_T^4}{4(1-X)^2} + Y_L^2 \right]^{1/2}} \quad (3.27)$$

In the case of a wave propagating in the direction of the magnetic field ($\theta = 0^\circ$), the Appleton-Hartree equation reduces to:

$$n^2 = 1 - \frac{X}{1 \pm Y_L} \quad (3.28)$$

For electromagnetic propagation along the magnetic field, the characteristic modes correspond to waves that are left and right circularly polarized. In fact, the angle between the wavevector and the magnetic field does not have to be exactly zero degrees for the left and right circularly polarized waves be the characteristic modes of the medium. They will be characteristic modes as long as

the quasi-longitudinal (QL) approximation is valid. The QL approximation requires:

$$R = \frac{4(1 - X)^2 Y_L^2}{Y_T^4} \gg 1 \quad (3.29)$$

Jicamarca radar takes advantage of the QL approximation to make absolute measurements of the ionospheric density using the Faraday rotation technique (e.g. *Farley, 1969b; Pingree, 1990; Aponte, 1998*). This technique will be explained below. For now, it will be shown that the longitudinal approximation is, in fact, valid for most of Jicamarca observations. Fig. 3.4(a) shows an example of a daytime ionospheric profile for Jicamarca's location based on the IRI model for 2005. The geomagnetic field intensity and the angle between the radar pointing direction and the geomagnetic field as a function of range are calculated using the IGRF for 2005 and are shown in panels (b) and (c), respectively. The magnetic field values are calculated for the on-axis position, which is the radar pointing position generally used for Faraday rotation measurements at Jicamarca. The corresponding ratio R (Eq. 3.29) was calculated and it is shown in panel (d) of Fig. 3.4. The figure shows that R varies from between 15 and 20 at F regions heights, indicating that the QL approximation can be used. In fact, the characteristic modes are not exactly circular. They are slightly elliptical, but this is compensated for by the transmission and reception hardware at Jicamarca.

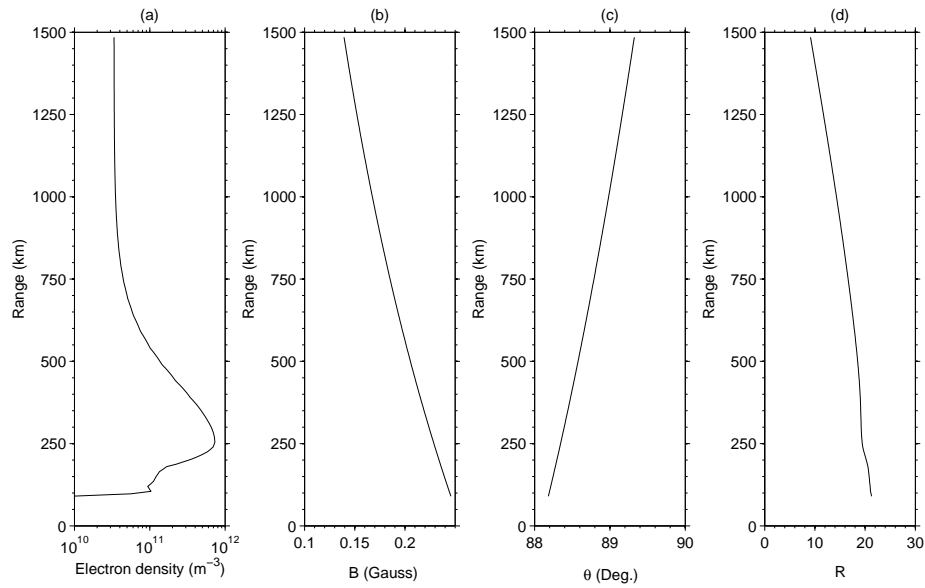


Figure 3.4: (a) Example of an equatorial daytime ionospheric profile from the IRI model, (b) magnetic field intensity and (c) the angle between the wavevector \mathbf{k} and the magnetic field calculated for Jicamarca's on-axis position (for 2005), and (d) the corresponding ratio R as defined in Eq. 3.29.

3.7 Faraday rotation

In most observatories, digisonde measurements of the ionospheric F region peak density ($N_m F_2$) are used to calibrate backscatter power profiles that, after range correction, are used to represent density profiles. Some radar facilities are capable of measuring the full IS spectrum, and absolute density measurements can be made from the plasma line. At night, however, these lines can be too weak to be detected. Their detection is more likely during daytime when they are enhanced by fast photoelectrons (*Beynon and Williams, 1978*). The operating frequency (50 MHz) and the ability to transmit signals with orthogonal polarizations allow the Jicamarca radar to make measurements of the absolute

electron density in the ionosphere using Faraday rotation (*Farley, 1969b*).

In the Faraday rotation approach, the idea is that electromagnetic waves with orthogonal polarizations travel at different phase speeds in a magnetized plasma. Given that the two waves travel the same path, the total electron content along the path can be inferred from the phase difference between the two waves. This technique has been widely employed in the estimation of the total electron content (TEC) of the ionosphere using signals transmitted by satellites and received on the ground or by other satellites (e.g. *Davies, 1990*). In general, there is ambiguity involved in the TEC estimation due to the possibility of phase differences exceeding 2π radians.

In the radar case, not only the TEC but also the vertical profile of the electron density can be estimated. This is done by differentiating the phase difference with respect to range. There is no ambiguity in the density profile estimation since the phase difference between two range gates does not exceed 2π for a well-designed experiment. As shown in the previous section, the quasi-longitudinal approximation is valid for typical Jicamarca measurements. Therefore, the indices of refraction for the two characteristic modes are given by Eq. 3.28:

$$n_R^2 = 1 - \frac{\omega_p^2}{\omega} \left(\frac{1}{\omega - \Omega_e} \right) \quad (3.30)$$

$$n_L^2 = 1 - \frac{\omega_p^2}{\omega} \left(\frac{1}{\omega + \Omega_e} \right) \quad (3.31)$$

Considering that $\frac{\Omega_e}{\omega} \ll 1$ and $\frac{\omega_p}{\omega} \ll 1$, it is possible to write the phase difference for the left and right circularly polarized waves as:

$$\begin{aligned}
d\phi &= \frac{\omega}{c}(n_R - n_L)dl \\
d\phi &= \left(\frac{e^3}{\epsilon_0 m_e^2 c \omega^2} \right) n_e(l) B(l) \cos \theta(l) dl
\end{aligned} \tag{3.32}$$

Eq. 3.32 shows that the phase difference depends on the length of propagation path (dl), and the magnetic field intensity and direction with respect to the wave propagation direction [$\mathbf{B}(l) \cdot \hat{\mathbf{k}} = B(l) \cos \theta(l)$] along the path. Assuming that the magnetic field and density change slowly along the path, the density profile is related to the phase measurements by the following expression:

$$n_e(h) = \left(\frac{c \omega^2 m_e^2 \epsilon_0}{e^3 B \cos \theta} \right) \frac{d\phi(l)}{dl} \tag{3.33}$$

where accurate estimates of B and θ can be obtained from geomagnetic field models. Faraday measurements have been performed at Jicamarca routinely using a double-pulse IS radar mode. In this mode, IS ACFs and Faraday rotation can be measured simultaneously. In practice, density profiles are not estimated from Faraday rotation alone. Faraday rotation is very sensitive to clutter, and uncertainties of the estimated density become large in the topside F region. Furthermore, Faraday rotation cannot be accurately measured in the topside and bottomside F region at night when the density and signal-to-noise ratio are very low. It is common practice to use Faraday rotation values from the F_2 region to calibrate backscattered power profiles. It will be shown in Chapter 4 that power profiles must also be corrected by the proper radar cross section so that they can accurately represent density profiles.

3.8 Instrumentation

This dissertation presents results of observations made by two radars. Incoherent scatter observations were made with the Jicamarca radar located near Lima, Peru (76.87° W, 11.95° S). Coherent scatter observations were made by a small radar located in São Luís, Brazil (44.21° W, 2.59° S). Both radars are located near the magnetic equator as shown in Fig. 3.5.

3.8.1 Jicamarca radar

The radar in Peru is part of the Jicamarca Radio Observatory, a facility of the *Instituto Geofísico del Perú* - IGP (National Geophysical Institute of Peru) operated with funds of the US National Science Foundation (NSF) through Cornell University. The Jicamarca Radio Observatory began operation in the early sixties with emphasis on IS radar observations of the ionosphere. Currently, the radar can be operated in either incoherent or coherent backscatter mode.

The Jicamarca radar has three (soon four) 1.5 MW peak power transmitters and operates at 50 MHz (more precisely 49.92 MHz) with a receiving bandwidth of about 1 MHz. The radar is equipped with an impressive 288m by 288m antenna array with a beamwidth as small as 1° . The array is formed by 64 (8×8) independent modules of 12×12 crossed half-wave dipoles. The crossed dipoles make possible the transmission/reception of circularly polarized waves and Faraday rotation measurements. The polarization and phase of each module can be set individually. Currently, this is done manually by adding cables of different lengths at each module. The implementation of a digital phase switch-

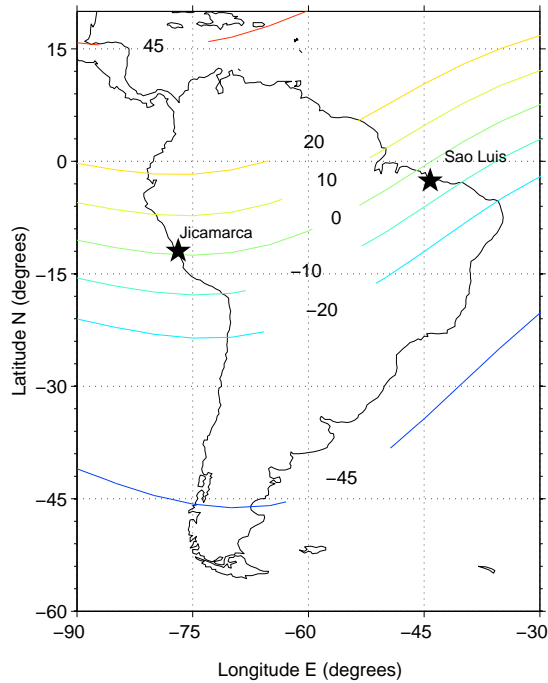


Figure 3.5: Location of the two radar facilities where observations presented in this dissertation were made. Contours of magnetic inclination are also shown (IGRF values for 2005). Incoherent scatter observations were made with the Jicamarca radar, while coherent scatter observations were made with the São Luís radar.

ing is planned. Jicamarca IS radar observations are presented and analyzed in Chapters 4 and 5.

3.8.2 São Luís radar

The system at São Luís is a small, low-power coherent backscatter radar maintained by the *Instituto Nacional de Pesquisas Espaciais* - INPE (Brazilian National Institute for Space Research) with partial support from FAPESP, a São Paulo State research agency. The radar began operation in December, 2000, and was

originally capable of basic two-antenna interferometric observations. In 2005, the radar system was upgraded, and two more antenna modules were added to the existing system. The radar is now capable of producing interferometric images of scattering layers of ionospheric irregularities. The São Luís radar has two 4-kW transmitters and operates at 30 MHz (more precisely 29.795 MHz). This radar has the advantage of a field of view that is wider than what is currently available at Jicamarca. Chapter 6 gives more details about this radar and discusses results related to radar imaging of equatorial spread F structures.

CHAPTER 4
ON THE PROPER RADAR CROSS SECTION FOR JICAMARCA OBLIQUE
IS RADAR OBSERVATIONS*

4.1 Introduction

It has been shown recently that, for measurements made close to perpendicular to the geomagnetic field, electron Coulomb collisions cause significant changes in the shape of the IS spectrum (*Sulzer and González, 1999*). This collisional effect has important implications in the estimation of ionospheric plasma parameters from IS radar observations at Jicamarca (e.g. *Aponte et al., 2001*). Additionally, the IS radar cross section (RCS) can also be significantly affected by Coulomb collisions (*Milla and Kudeki, 2006*). This chapter describes a study of the IS radar cross section (RCS) at small aspect angles ($1^\circ < \alpha < 6^\circ$) and its application in the correction of power profiles measured at Jicamarca. Once corrected with the proper RCS, power profiles can be used to represent the height variation of the ionospheric electron density. This is a long standing question at Jicamarca, since the calculation of the IS RCS requires full knowledge of the IS spectrum at small aspect angles. It is important to emphasize that Jicamarca is the only low-latitude radar facility where the RCS calculations and power corrections can be validated against absolute density measurements obtained from Faraday rotation measurements. Another motivation for the study of the IS RCS is the possibility of estimating the electron-to-ion temperature ratio (T_e/T_i) from the ratio between electron density (from Faraday rotation) and backscattered power. The T_e/T_i information could be used, for instance, in a fitting routine

*Some of this chapter has been adapted from the original published work, *Rodrigues et al. (2007a)*. Reproduced by permission of American Geophysical Union.

to estimate the fraction of molecular ions from IS measurements in the lower F region.

4.2 Magnetic field effects in the IS spectrum

The IS spectrum becomes narrower at small aspect angles. This is because, at angles close to perpendicular to the magnetic field, Landau damping of the ion acoustic waves disappears, leading to long-lived scattering (Bragg) waves (*Bernstein, 1958; Farley et al., 1961*). Therefore, the IS spectrum (autocorrelation function) becomes narrower (flatter) as the aspect angle (α) decreases. Another way of interpreting this effect is to think of the control of the magnetic field over the transverse motion of the electrons. The electrons have a small gyroradius compared to the radar wavelength, and so the gyromotion does not affect significantly the phase of the signal. Their guiding center motion affects the phase of the signal, but only the component of this motion along the radar wavevector \mathbf{k} affects the scattering. The smaller the aspect angle, the farther the electron must move to affect the phase of the radar signal, as illustrated in Fig. 4.1. At small aspect angles, the guiding center of the random electron motion appears slower, and the electron behaves as a heavier particle with an effective mass $m'_e = m_e / \sin^2 \alpha$. The narrowing of the IS spectrum at small aspect angles has been used at Jicamarca for many years to make very accurate plasma drift measurements (*Woodman and Hagfors, 1969; Kudeki et al., 1999*).

4.3 Discrepancies in the IS radar observations at Jicamarca

Over the past four decades, theoreticians and experimentalists were satisfied with the theory describing the Doppler spectrum of radio waves incoherently scattered by electrons in the ionosphere. Results of measurements made at different IS radar sites indicated that the theory was complete. However, discrepancies in the electron and ion temperatures estimated from IS measurements made with the Jicamarca radar were often observed. An unexplained additional narrowing of the spectrum resulted in lower apparent electron temperatures when plasma parameters were estimated. In some cases, the estimated electron temperatures were even lower than the ion temperature. There was a high confidence in the IS theory, and consensus was that the discrepancies were caused by some sort of systematic measurement error. A careful investigation to evaluate and mitigate possible error sources was carried out by *Pingree (1990)*. In the end, a source of measurement errors could not be found, but a series of improvements were made in the double-pulse and Faraday experiments at Jicamarca thanks to this effort.

4.4 Electron Coulomb collision effects in the IS spectrum

The discrepancies in the Jicamarca observations were resolved when *Sulzer and González (1999)* showed that electron-electron and electron-ion Coulomb collisions are responsible for the unexpected narrowing of the spectrum. *Sulzer and González (1999)* demonstrated the effects of electron Coulomb collisions on the shape of the IS spectrum using Monte-Carlo simulations of the electron motion. As described earlier, the smaller the aspect angle, the longer the electron must

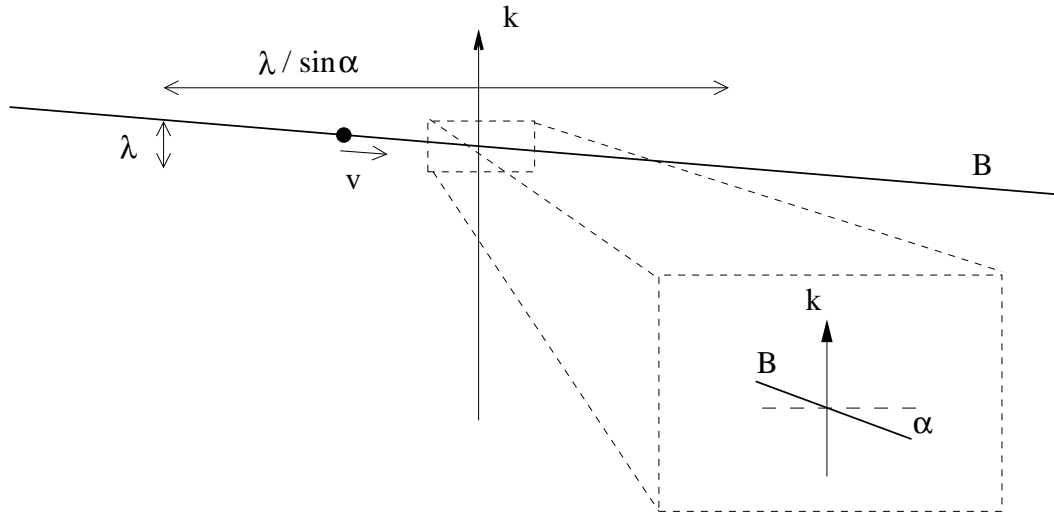


Figure 4.1: Sketch illustrating how the electron motion affects the phase of the radar signal.

move to affect the phase of the radar signal. Therefore, at smaller aspect angles, electron collisions become more important. At F region heights, collisions with neutrals can be neglected, but Coulomb collisions with other electrons and ions can be important. The random nature of the electron motion along the magnetic field determines the IS spectrum. The temperature profiles shown by *Aponte et al.* (2001) served to illustrate that non-physical values of $T_e/T_i < 1$ are no longer obtained from Jicamarca measurements when electron Coulomb collisions effects are taken into account.

4.5 The calculation of the IS spectrum including electron Coulomb collisions

The IS scatter spectrum was described in Chapter 3. For reader's convenience, we reproduce the results here:

$$\langle |n_e(\mathbf{k}, \omega)| \rangle = \frac{2N_e |y_e|^2 \sum_j n_j \text{Re}(y_j) + |\sum_j \mu_j y_j + i\lambda_{De}^2 k^2|^2 \text{Re}(y_e)}{\omega |y_e + \sum_j \mu_j y_j + i\lambda_{De}^2 k^2|^2} \quad (4.1)$$

where N_e is the electron density, $\lambda_D = \left(\frac{\epsilon_0 K_B T_e}{N_e e^2}\right)^{1/2}$ is the electron Debye length, k is the scattering wave number, y_j is the normalized ion admittance function, y_e is the normalized electron admittance function, $n_j = N_j/N_e$ is the fraction density for each ion species, and $\mu_j = T_j/T_e$ is the ratio of the ion temperature T_j to electron temperature T_e . Note that j is a subscript that refers to each ion species. Collisions with neutrals can be neglected at F region altitudes, and the admittance function becomes:

$$y_s = i + \theta_s J_s \quad (4.2)$$

Again, θ_s is the normalized frequency and J_s is the so-called Gordeyev integral for each plasma species s . Coulomb collisions and magnetic field effects are taken into account in the derivation of the admittance functions and Gordeyev integrals.

4.5.1 The Gordeyev integral for a collisional and magnetized plasma

In this study and for operational purposes at Jicamarca, the IS spectrum for small aspect angles ($\alpha < 6^\circ$) has been computed using a numerical library of the electron Gordeyev integral provided by *Sulzer and González* (1999). The li-

brary is a result of numerical simulations and contains the electron Gordeyev integral as a function of electron density, electron temperature, radar frequency and aspect angle. At F region heights, ion Coulomb collisions destroy the ion gyroresonance and the ion Gordeyev integral for an unmagnetized plasma can be used (Farley, 1964; Pingree, 1990). In the next chapter, an alternative approach to the calculation of the IS spectrum at small aspect angles suggested by Woodman (2004) and Kudeki and Milla (2006) will be presented. Magnetic field and Coulomb collision effects on the ion gyrorotation and their implications for the IS spectrum will also be studied in more detail in the next chapter.

4.5.2 Illustration of electron Coulomb collision effects

Fig. 4.2 shows examples of IS spectra calculated for various aspect angles and a relatively high value of electron density ($n_e = 10^{12} \text{ m}^{-3}$). These curves were computed for the cases of an unmagnetized plasma and a magnetized plasma with and without electron Coulomb collision effects taken into account. The curves show that as the aspect angle increases, the effect of both Coulomb collisions and magnetic field decrease. At about 6° , collisional effects in the spectral shape are almost negligible. On the other hand, magnetic field effects are still observable and must be considered, even at 6° .

At very small aspect angles (0.25°), electron Coulomb collisions significantly change the shape of the IS spectrum. The collisional spectrum differs greatly from the spectrum for a magnetized plasma. The spectrum becomes much narrower than the spectrum predicted for collisionless plasma. Also, the overall spectral shape seems to be modified by the collisions. At very small aspect an-

gles, the spectral shape resembles a Lorentzian function, while the spectrum for the magnetized collisionless plasma looks Gaussian. These changes on the shape of the IS spectrum must be considered when estimating ionospheric parameters from the IS measurements. For instance, the width of the spectrum is proportional to the electron-to-ion temperature ratio. Fig. 4.2 shows that, even at about 4° , the collisional effect can be observed in the IS spectrum.

Fig. 4.3 shows another set of IS spectra calculated for a relatively low electron density ($n_e = 5 \times 10^{12} \text{ m}^{-3}$). These examples show that, even for small densities values, electron Coulomb collision effects are noticeable at aspect angles as large as 2° .

4.6 Standard IS radar pointing positions at Jicamarca

Fig. 4.4 shows the height variation of the aspect angle for the three standard pointing positions used at Jicamarca for oblique IS observations. The pointing positions are chosen by changing the phases of the 8×8 antenna modules forming the antenna array. For historical reasons, these pointing positions are called the on-axis, 4.5° , and 6° positions. The on-axis position is obtained when the antenna modules are in phase. This position has been used for typical electron density measurements at Jicamarca. At this pointing position, the aspect angle varies from about 1.8° to 1.0° in the 150-1000 km range, and the electron Coulomb effects cannot be neglected. In the past, the so-called 6° position was used to minimize the effects of the electron Coulomb collisions in the temperature estimates. However, avoiding the collision effects by using this position might not be possible nowadays due to changes in the Earth's magnetic field

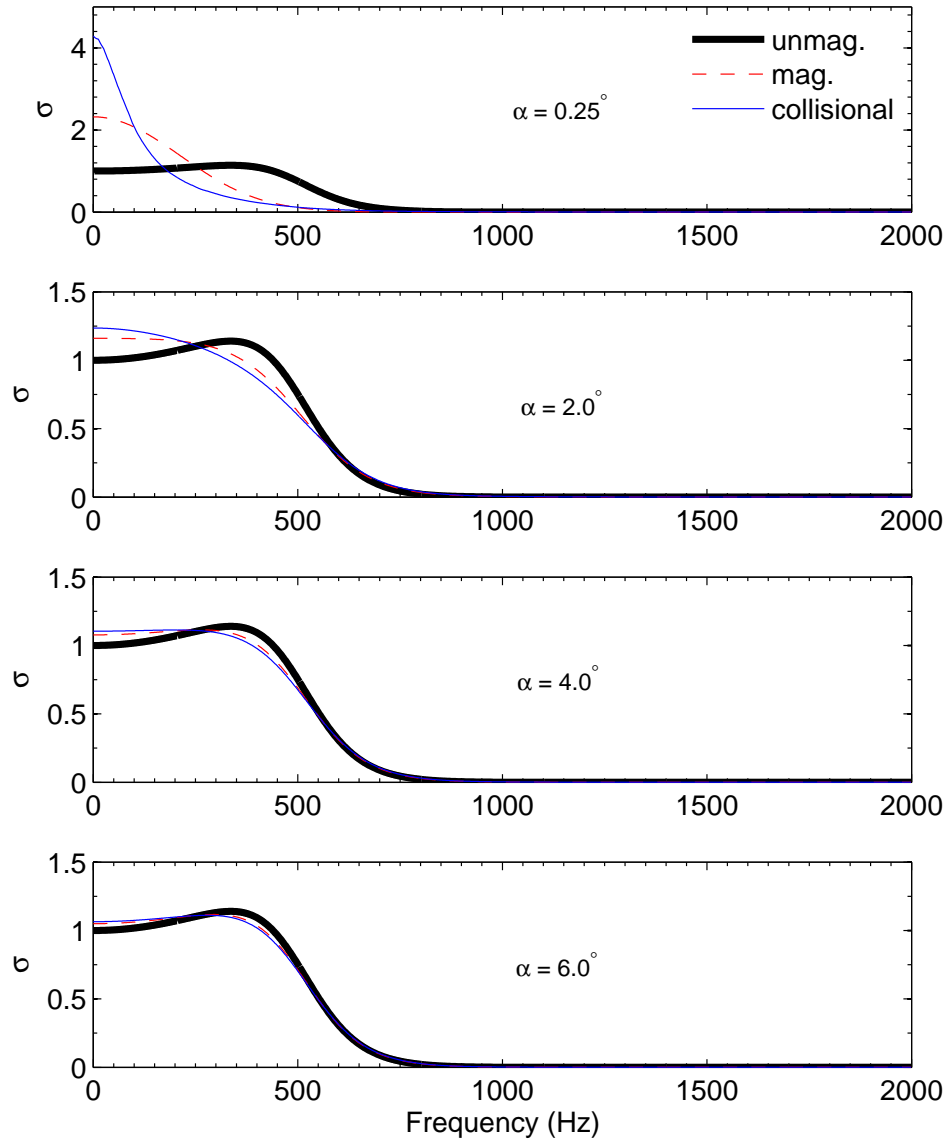


Figure 4.2: Incoherent scatter spectra calculated for different aspect angles (α) for an unmagnetized plasma, a collisionless magnetized plasma, and magnetized plasma with electron Coulomb collision effects included (O^+ plasma, $T_e = T_i = 1000$ K and $n_e = 10^{12} \text{ m}^{-3}$).

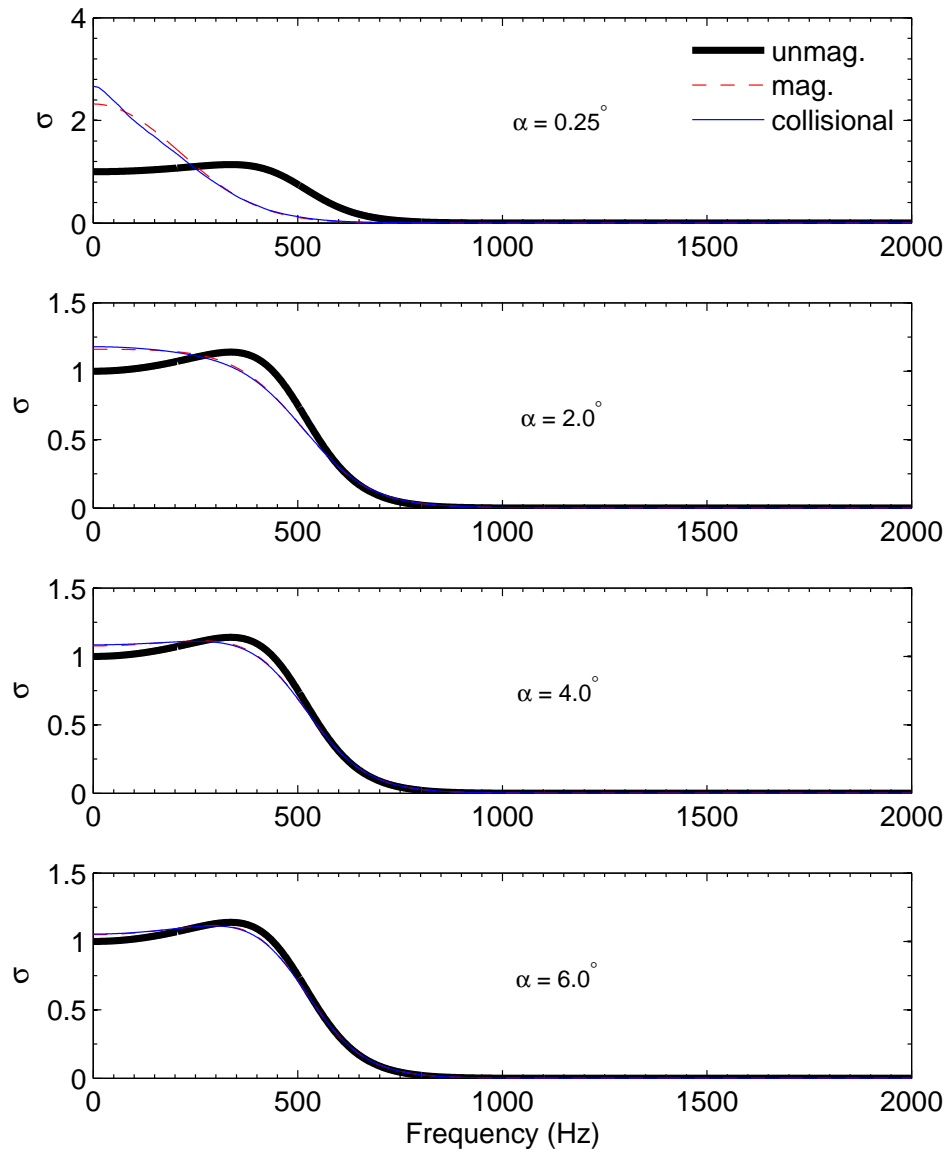


Figure 4.3: Same as Fig. 4.2 but for $n_e = 5 \times 10^{10} \text{ m}^{-3}$.

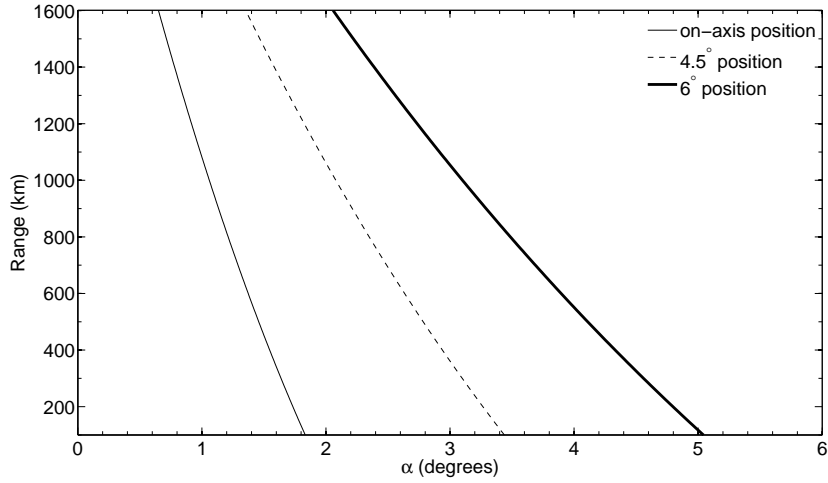


Figure 4.4: Height variation of the aspect angle (α) for the three standard pointing positions at Jicamarca. Calculations used geomagnetic field values from the IGRF model (April 2006).

geometry. Since the early measurements at Jicamarca in the 1960's, the aspect angles for the standard positions changed significantly. Fig. 4.4 shows that the aspect angle now varies from 3° to 5° in the 150-1000 km range, and electron Coulomb collisions are still significant at this pointing position as illustrated in Fig. 4.2. Furthermore, the aperture efficiency is much less at the 6° position than at the on-axis position.

4.7 IS radar cross section

The volumetric differential radar cross section ($\sigma(\mathbf{k}, \omega)$) is related to the spectrum of the electron density fluctuations ($\langle |n_e(\mathbf{k}, \omega)|^2 \rangle$):

$$\sigma(\mathbf{k}, \omega)d\omega = 4\pi r_e^2 \langle |n_e(\mathbf{k}, \omega)|^2 \rangle d\omega \quad (4.3)$$

where r_e is the classical electron radius. The integral of the differential radar cross section over all frequencies gives the total volumetric IS radar cross section (σ_T):

$$\sigma_T(\mathbf{k}) = \int_{-\infty}^{\infty} \frac{d\omega}{2\pi} \sigma(\mathbf{k}, \omega) \quad (4.4)$$

In this dissertation, σ_T is often referred to as the IS RCS. The received backscattered power P_{rec} from a soft target illuminated by the radar at range r can be described by (e.g. *Milla and Kudeki, 2006*):

$$P_{rec}(t) = K_{sys} \int \frac{d\omega}{2\pi} dr d\Omega \frac{G^2(r, \theta, \phi)}{r^2} |\chi(t - \frac{2r}{c}, \omega)|^2 \sigma(\mathbf{k}, \omega) \quad (4.5)$$

where K_{sys} is a system constant that takes into account several radar parameters, $d\Omega = \sin(\theta)d\theta d\phi$, where θ and ϕ are the usual polar coordinates (not to be confused with the normalized frequencies defined earlier), $G(r, \theta, \phi)$ is the antenna gain, and $|\chi(t - 2r/c, \omega)|^2$ is the radar ambiguity function describing the contributions to the received power according to the signal range and Doppler shift.

4.7.1 The efficiency factor η

Following the notation of *Milla and Kudeki (2006)*, the efficiency factor η is defined next. If the radar has a narrow antenna beam and the transmitted pulses

are not too long, one can assume that the cross section is constant over the volume illuminated by the radar, and Equation 4.5 can be written as:

$$P_{rec} = K'_{sys} \frac{\eta(\mathbf{k})}{r^2} \quad (4.6)$$

where η is an efficiency factor defined in *Milla and Kudeki (2006)*:

$$\eta(\mathbf{k}) = \int \frac{d\omega}{2\pi} \frac{\langle |n_e(\mathbf{k}, \omega)|^2 \rangle}{N_e} \quad (4.7)$$

The efficiency factor can be seen as a normalized version of the IS RCS:

$$\eta(\mathbf{k}) = \frac{\sigma_T(\mathbf{k})}{4\pi r_e^2 N_e} \quad (4.8)$$

The name supposedly comes from the efficiency that electrons have of shielding the ions and causing scattering. In general, this efficiency decreases as T_e/T_i increases, at least for typical T_e/T_i values found in the *F* region ionosphere. Equation 4.6 shows that the received power is a function of the electron density, distance from the target to the radar, and efficiency factor. Since K'_{sys} is constant and the range r is known, electron density can be inferred from backscattered power as long as the efficiency factor has been correctly estimated.

4.8 Electron Coulomb collision effects in the IS RCS

Milla and Kudeki (2006) have pointed out that Coulomb collisions also affect the IS RCS at small aspect angles. This has immediate implications for using IS power profiles to represent ionospheric electron density profiles. *Farley* (1966b) showed that for a magnetic field-free collisionless plasma with a Debye length much smaller than the radar wavelength, the total RCS σ_T is given by $\sigma_T \approx \frac{4\pi r_e^2 N_e}{1+T_e/T_i}$, where N_e is the electron density, r_e is the classical electron radius, and T_e and T_i are the electron and ion temperatures, respectively. Farley's result is also valid for large aspect angles and it is often referred to when power-density conversions are made. Fig. 4.5 shows the results of a numerical calculation of the RCS for an unmagnetized plasma. The results are compared with Farley's approximation. The approximation works well for low values of temperature ratio (say $T_e/T_i < 3$) which is typically the case in the low latitude ionosphere. However, this relationship is incorrect at small aspect angles and deteriorates further when electron Coulomb collisions are considered, as will be shown next. *Farley* (1966b) also investigated the IS RCS for a magnetized collisionless plasma.

Fig. 4.6 compares the efficiency factor of magnetized plasmas with and without electron Coulomb collisions taken into account. The efficiency factor for an unmagnetized collisionless plasma is also shown for comparison. Note that for $T_e = T_i$, the efficiency factor is 0.5 in the three cases. At small aspect angles, the efficiency factors for magnetized plasmas differ significantly from the values for an unmagnetized plasma. These results show, however, that even for a considerably large value of electron density ($N_e = 10^{12} \text{ m}^{-3}$), collisions do not greatly affect the RCS for $\alpha > 0.25^\circ$. At $\alpha = 6^\circ$, Coulomb collision effects are negli-

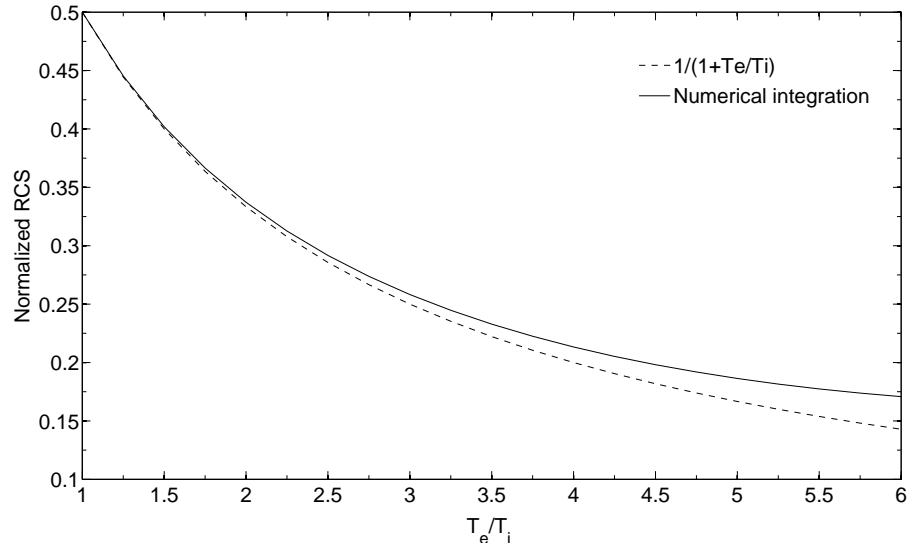


Figure 4.5: Results of numerical calculation of the IS RCS (Eq. 4.7) for an unmagnetized plasma and comparison with the approximation $\sigma_T \approx \frac{4\pi r_e^2 N_e}{1+T_e/T_i}$ found by Farley (1966b). The results are for Jicamarca frequency (50 MHz), an O^+ plasma, $T_i = 1000$ K and $N_e = 10^{12} \text{ m}^{-3}$.

ble, but magnetic field effects are still observable. At larger aspect angles, the efficiency factor for a magnetized plasma approaches that of a magnetic field-free plasma. The range of aspect angles and T_e/T_i studied here was limited by the library of electron Gordeyev integrals used to calculate the IS spectrum. At smaller aspect angles, Coulomb collisions will have a more significant impact in the RCS. At the moment, the IS spectrum for $\alpha < 0.25^\circ$ is being studied by means of numerical simulation at University of Illinois at Urbana Champaign (Milla and Kudeki, personal communication) and will greatly improve our understanding of the IS spectrum near perpendicular to the magnetic field.

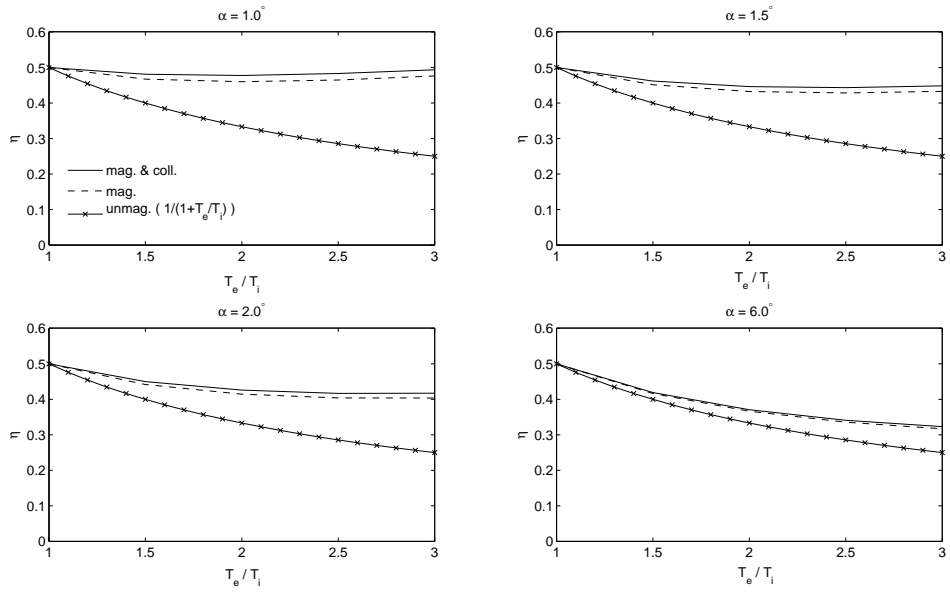


Figure 4.6: Efficiency factors for different aspect angles. Results are for a magnetized plasma with and without electron Coulomb collisions effects included and for a unmagnetized plasma (O^+ plasma with $T_i = 1000^\circ$ and $N_e = 10^{12} \text{ m}^{-3}$).

4.9 Experimental setup

The operating frequency of the Jicamarca radar, its narrow beamwidth, and cross-polarized antenna array permit electron density profile measurements using Faraday rotation (*Farley, 1969b*). In general, Faraday rotation measurements are made simultaneously with measurements of the IS autocorrelation function (ACF) using a double-pulse transmission scheme. While Faraday rotation provides the height variation of the electron density, the ACFs provide both electron and ion temperature profiles as well as backscattered power profiles. However, Faraday rotation measurements are imprecise at low SNR. In practice, corrected power profiles normalized to Faraday rotation measurements are used to repre-

sent the height variation of the electron density.

The measurement results presented in this chapter were found with Jicamarca's "hybrid 2" mode on April 20, 2006 using the on-axis position. The hybrid 2 mode combines the double-pulse mode for F -region observations and the long-pulse mode for topside ionosphere measurements. Only double-pulse observations will be discussed here. The double-pulses were 0.1 ms long and interleaved with the 1.5 ms long uncoded pulse. The sampling rate was 10 kHz, giving independent range gates every 15 km. The interpulse period for the entire set of pulses, including the long pulse and two pairs of double pulses, was 6,000 km.

Ten non-zero lags of the autocorrelation function (ACF) spaced by 0.2 ms plus the zero-lag (power) measured with the double-pulse experiment. Estimates for T_e and T_i were obtained by fitting the ACFs assuming a purely O^+ plasma. The fitted ACFs were obtained after a time integration of about 22 minutes. The procedure also yields error estimates for both temperatures. The reader is referred to *Pingree (1990)* for a detailed description of the error analysis for the double-pulse experiment. Uncertainties for the efficiency factor were also estimated. In estimating the uncertainty in the efficiency factor, errors in the electron density from Faraday rotation and aspect angle uncertainties were neglected. Changes in electron densities do not greatly affect the efficiency factor for the aspect angles in question, and errors in the IGRF values are assumed to be much smaller than errors in T_e and T_i .

Fig. 4.7 shows an example of the power-density observations that have been analyzed. Panel (a) of Fig. 4.7 shows a power profile (range-squared corrected and calibrated to the Faraday measurements at the F -region peak, assuming

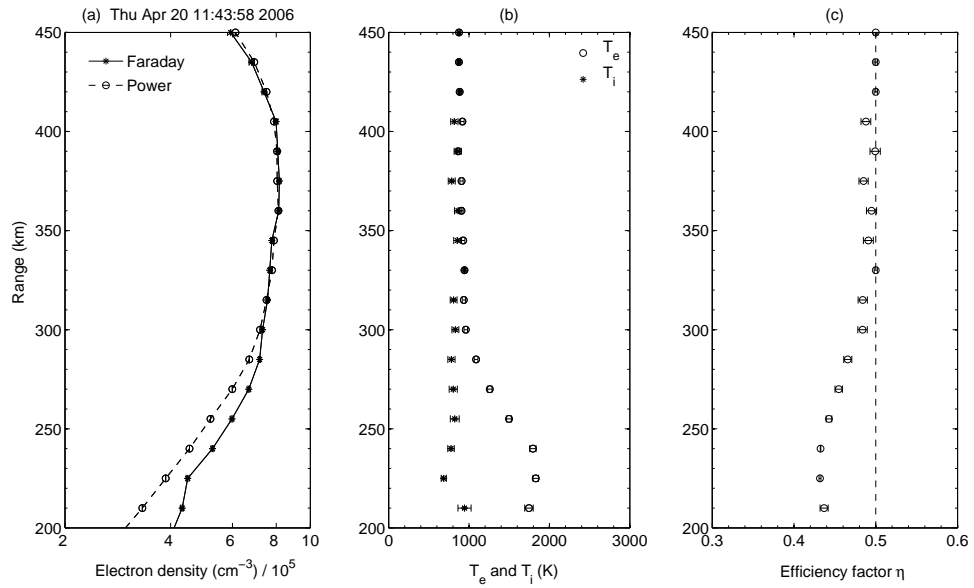


Figure 4.7: Example of (a) backscattered power and Faraday rotation measurements, (b) electron and ion temperature measurements, and (c) efficiency factor calculated using known values (from IGRF) of aspect angles and measured values of n_e , T_e and T_i .

$T_e = T_i$) along with an electron density profile from the Faraday rotation measurements. Panel (b) shows estimates of the electron and ion temperature profiles obtained from fits to the double pulse autocorrelation functions. Panel (c) shows the efficiency factor as a function of height calculated using the Faraday measurements of electron densities and the fitted temperatures. Uncertainties are also shown for each profile. The electron density from Faraday rotation and the backscattered power diverge in the region where $T_e > T_i$ (< 300 km) due to the efficiency factor effects.

4.10 Validating RCS calculations and power corrections

Using the efficiency factor, power profiles measured at Jicamarca were corrected and compared with electron density profiles derived from Faraday rotation. Fig. 4.8 shows the corrected power profiles and Faraday electron density profiles for three different times on April 20, 2006. Time resolution for each profile is 22 minutes. These are typical of double-pulse measurements made at Jicamarca. Higher time and range resolution profiles can be obtained if the double-pulse experiment is run by itself or if the pulses are Barker coded. Left panels show the uncorrected and corrected power profiles and the electron density profile measured with Faraday rotation for each time. The panels on the right side show the calculated efficiency factor for each time. Error bars for each profile are also shown.

The agreement for most of the points in the profiles (density and corrected power) is within their estimated uncertainties. However, some disagreement can be observed at lower ranges (< 215 km). Faraday rotation densities at lower range gates are larger than the densities predicted by the corrected power profiles. This disagreement can be caused either by clutter affecting the IS ACFs and/or the Faraday rotation or by molecular ions, which were not included in the plasma composition. If an appreciable amount of molecular ions is present, T_e/T_i can be overestimated, and the efficiency factor can be underestimated. However, large variations in the Faraday density at these heights from profile to profile suggest that the discrepancies are caused by clutter affecting the Faraday angle estimation.

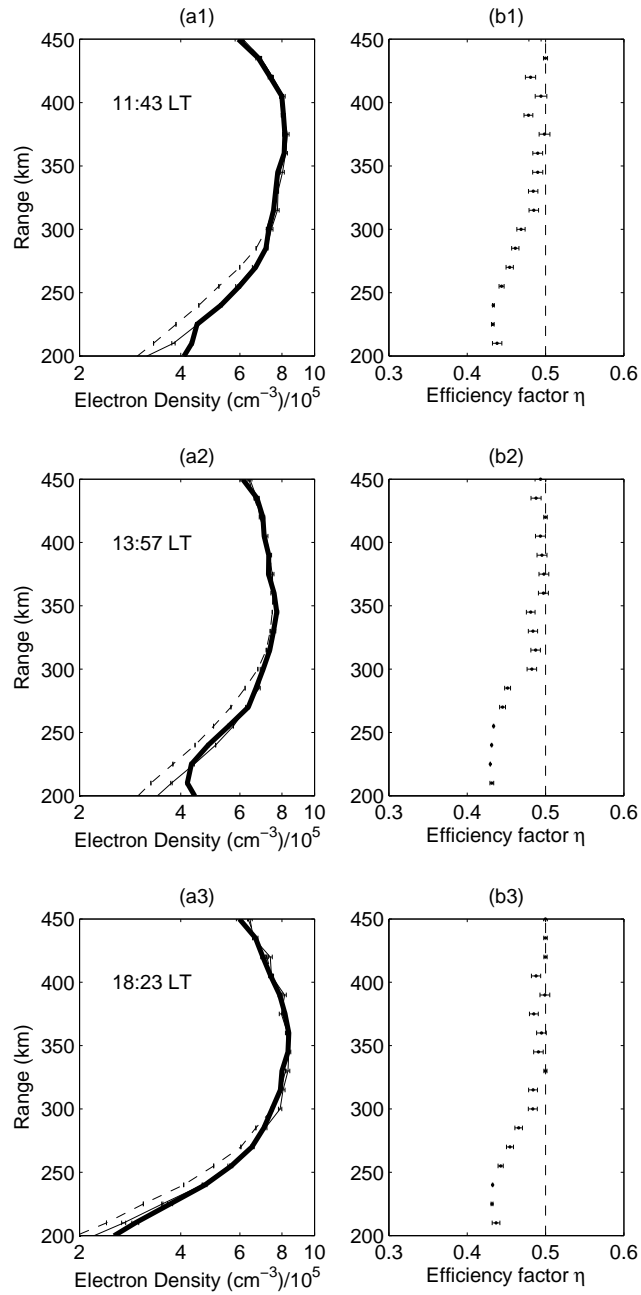


Figure 4.8: Examples of power (dashed line), corrected power (solid line), and Faraday rotation (thick solid line) for three different times on April 20, 2006. Predicted efficiency factors used in the power correction are also shown in the panels on the right.

4.11 On the estimation of T_e/T_i from power-density measurements

Another motivation for the study of the IS RCS was the possibility of estimating T_e/T_i from the ratio between backscattered power and density similar to what has been done with Arecibo plasma line observations (*Aponte et al., 2007*). With the T_e/T_i information, one can obtain the fraction of molecular ions in the bottomside F region from the IS ion line measurements. Considering the case of an unmagnetized plasma (or large aspect angles), where $\eta = \frac{1}{1+T_e/T_i}$ and rewriting Eq. 4.6 one obtains:

$$\frac{P_{rec}(r)}{N_e(r)} = \frac{K'_{sys}}{r^2} \left(\frac{1}{1 + T_e(r)/T_i(r)} \right) \quad (4.9)$$

Eq. 4.9 shows that T_e/T_i can be obtained for every range gate from the power-density ratio. K'_{sys} can be obtained from upper F region ranges where $T_e \approx T_i$. Unfortunately, at small aspect angles the unmagnetized approximation cannot be used as the results in Fig. 4.6 show. Furthermore, the results also show that, for a magnetized plasma and small aspect angles, η varies little as a function of T_e/T_i , making an unambiguous determination of the temperature ratio impractical, especially when considering typical errors in the power or density measurements ($> 5\%$).

4.12 An approximate formula for the efficiency factor of a magnetized plasma

A formula for the efficiency factor including magnetic field effects would be particularly useful for regular Jicamarca users willing to convert the power profiles available in the Jicamarca database to density profiles. Therefore, an approximate expression is proposed for the efficiency factor of a magnetized plasma based on the original $\eta = 1/(1 + T_e/T_i)$ expression (Farley, 1966b). This new expression shown in Eq. 4.10 has 5 parameters (T_r , α , p_1 , p_2 and p_3).

$$\eta_{new} = \frac{1}{1 + T_r^{[p_1(T_r/\alpha)^2 + p_2(T_r/\alpha) + p_3]}} \quad (4.10)$$

where, $T_r = T_e/T_i$, α is the aspect angle (in radians), and p_1 , p_2 , p_3 are constants whose values are 0.000023, -0.008800 and 0.943694 , respectively. These parameters were found by least-squares fitting to a series of efficiency factors for a magnetized collisionless plasma at various values of aspect angles between 1° and 6° and temperatures ratios (1 to 3). Fig. 4.9 shows a comparison of the efficiency factor obtained with the new expression and the efficiency factors from the full numerical calculation. The agreement is within a few percent for all aspect angles. If the aspect angle is less than 1° or if higher accuracy is necessary, full calculation of the IS RCS (including collisions) is recommended.

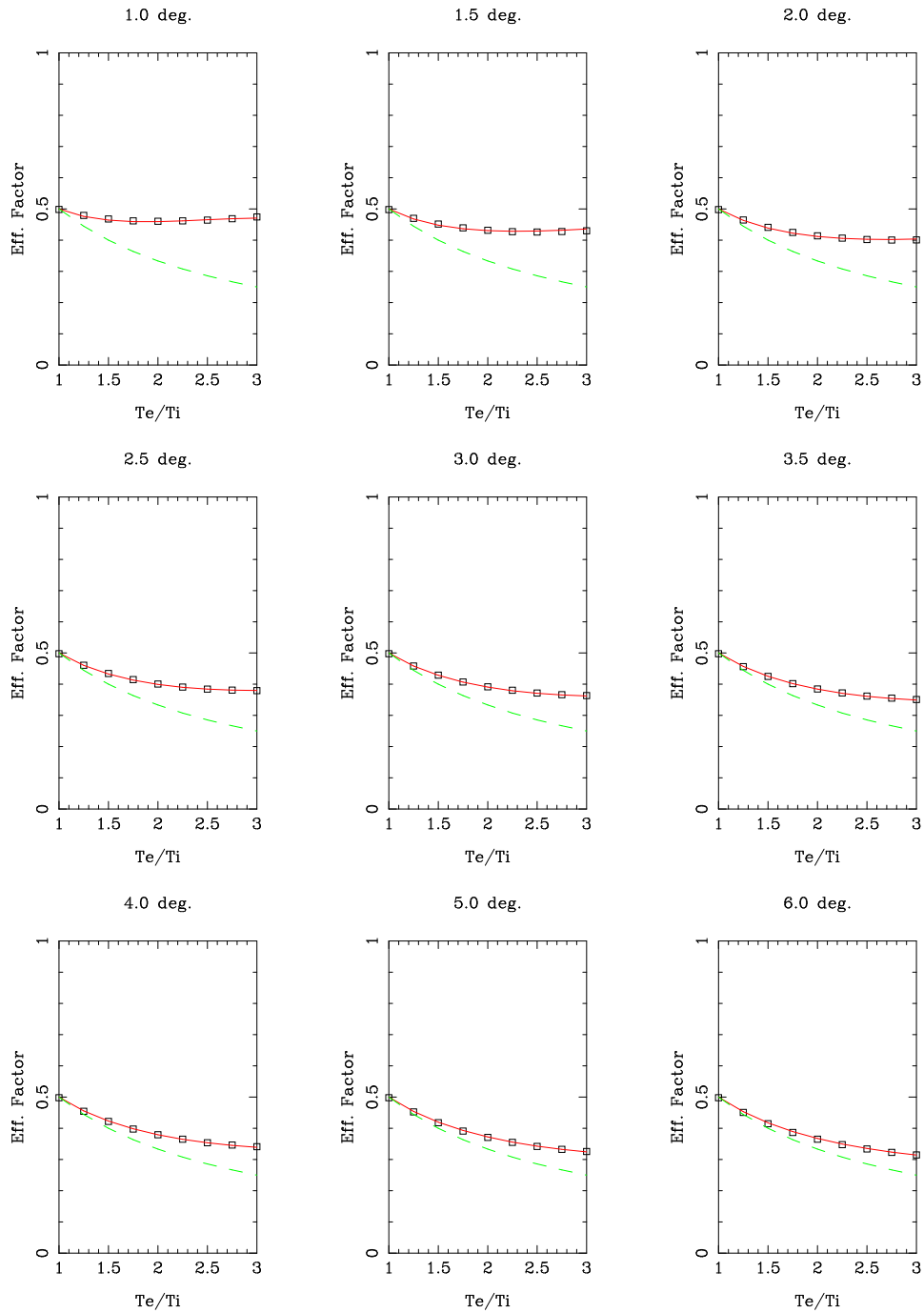


Figure 4.9: Efficiency factors for different aspect angles. Dashed lines show $\eta = 1/(1 + T_e/T_i)$. Square marks show the values of the η computed with full IS theory including electron Coulomb collisions. The solid line shows the results of the proposed new expression.

4.13 Summary

It was shown in this study that the magnetic field has a significant effect in the IS RCS at small aspect angles so that the usual $1/(1 + T_e/T_i)$ power-density correction cannot be used at Jicamarca, even in the 6° pointing position. Electron Coulomb collisions also affect the RCS but their effect can be considered secondary for aspect angles between 0.25° and 6° even for relatively large density values. It is stressed, however, that Coulomb collisions do affect significantly the shape of the IS spectrum even at $\alpha = 6^\circ$ and must be taken into account when estimating ionospheric parameters from the IS measurements. The analysis of the IS RCS at small aspect angles also indicated that T_e/T_i cannot be estimated unambiguously from the power to density ratio, at least from the on-axis pointing position at Jicamarca.

Using Jicamarca's unique capability of simultaneous measurements of the backscattered power and Faraday rotation angle (electron density), it was possible to confirm the correctness of cross section calculations for small aspect angles. Absolute electron density measurements are not possible with the UHF ALTAIR radar and similar direct comparisons were not possible in the work of *Milla and Kudeki* (2006). The effect of collisions in the RCS is about 5% at $\alpha = 1^\circ$, and becomes larger as the aspect angle decreases.

Efficiency factors including magnetic field and collision effects were used to correct power profiles. The corrected power profiles agree with electron density profiles derived from Faraday rotation within measurements uncertainties except at lower ranges where radar clutter can be affecting the Faraday measurements. This result can be used to improve electron density profiles measured

at Jicamarca. Previous power measurements made at Jicamarca can also be corrected. Power measurements are more accurate and less sensitive to clutter and interference than Faraday rotation measurements. Accurate electron density profiles can best be obtained by correcting the power profile and normalizing it with Faraday rotation measurements.

CHAPTER 5
NEW OBSERVATIONS OF THE PROTON GYRORESONANCE AT
JICAMARCA*

5.1 Introduction

At least two reasons motivated the construction of the Jicamarca incoherent scatter (IS) radar in Peru. The first reason, of course, was the necessity of observations in the equatorial region, which was known to be the home of interesting ionospheric phenomena. The second reason was that the IS theories predicted that, if the radar were pointed nearly perpendicular to magnetic field, it would be possible to detect the gyro-motion of the ions forming the plasma (*Salpeter, 1961; Farley et al., 1961*). In this case, Jicamarca could be used as a mass spectrometer (*Farley, 1991*). This would provide a powerful technique for studying ion composition.

First attempts to measure O^+ gyro-harmonics were unsuccessful and it was later realized that ion gyro-harmonics are destroyed by ion-ion collisions and that O^+ gyroresonance would not be detectable for any realistic F region densities (*Farley, 1964; Woodman, 1967*). In the topside ionosphere, however, where the densities are lower and collisions are less frequent, the proton gyroresonance was detected during an experiment performed by *Farley (1967)* indicating that the gyroresonance might still be useful for estimation of ionospheric parameters. The study of the ion gyroresonance was never continued, and automated

*Some of this chapter has been adapted from the original published work, *Rodrigues et al. (2007b)*. Reproduced by permission of American Geophysical Union.

estimation of ionospheric parameters from gyroresonance observations was not attempted (e.g. *Farley, 1991*).

In this chapter, observations of the proton gyroresonance in the topside ionosphere over Jicamarca are revisited. The main motivation for the renewed interest in the gyroresonance is to test the possibility of obtaining estimates of the topside composition (fractions of O^+ and H^+) and temperatures. Another reason for new gyroresonance observations is that the IS theory for small aspect angles has been improved recently so that the effect of electron Coulomb collisions is better understood and can be more easily added to numerical calculations of the IS spectrum (*Sulzer and González, 1999; Woodman, 2004; Kudeki and Milla, 2006*).

5.2 Topside observations at Jicamarca

Radar observations of the topside ionosphere using conventional incoherent scatter (IS) methods are difficult. The low signal-to-noise ratio and the large number of artificial satellites passing over the equatorial region are the main obstacles for topside IS radar observations. At Jicamarca, due to its operating frequency, the sky noise contribution is the dominant term in the total system noise temperature. The sky noise temperature at 50 MHz varies between 5,000 and 45,000 K. Therefore, IS radar measurements at Jicamarca are made at much lower signal-to-noise levels than most of the other IS radar systems. Other radar facilities usually operate at UHF or higher frequencies. The sky noise at 400 MHz is approximately 100 K.

Even though first topside measurements were made in the mid-1960's (*Farley, 1966a*), only a few new observations have been made since then. There has

been a renewed interest in topside measurements at Jicamarca in the last few years. These are motivated by the necessity of calibration of (or comparison with) satellite observations. *Hysell (2000a)* implemented a new topside mode at Jicamarca using alternating codes that seems to produce good results during high solar flux years when the ionospheric density is higher and echoes with larger signal-to-noise ratios are detected. For low solar flux conditions, a radar mode that uses a long uncoded pulse and novel parameter estimation techniques has been investigated (e.g. *Rodrigues and Hysell, 2005*). Recent results have shown that topside parameters might be obtained with the long pulse experiment even during low solar flux conditions (*Hysell et al., 2008*).

5.3 The ion gyroresonance

The IS theory for a collisionless magnetized plasma predicts spectral lines at multiples of the ion gyrofrequency (e.g., *Farley et al., 1961; Salpeter, 1961*). This effect occurs at small aspect angles ($\alpha < \sim 10^\circ$ for a H^+ plasma). The fluctuations in the IS spectrum map into peaks in the IS autocorrelation function (ACF) at lag times corresponding to multiples of the ion gyroperiod, $2\pi m_i/qB$ (where m_i is the ion mass, q is the ion charge, and B is the magnetic flux density). For mixtures of ions, peaks should exist at the gyroperiods of each ion, suggesting a powerful ionospheric diagnostic for composition measurements. The physical explanation for the ion gyroresonance is quite intuitive. The ions move in helical orbits, with Larmor (gyro) motion superimposed on a guiding center drift. Near perpendicular incidence, a radar with a wavelength in the appropriate regime ($\lambda/4\pi$ greater than the Debye length but less than the ion gyroradius) will be sensitive to the periodic motion at the gyrofrequency in the absence of

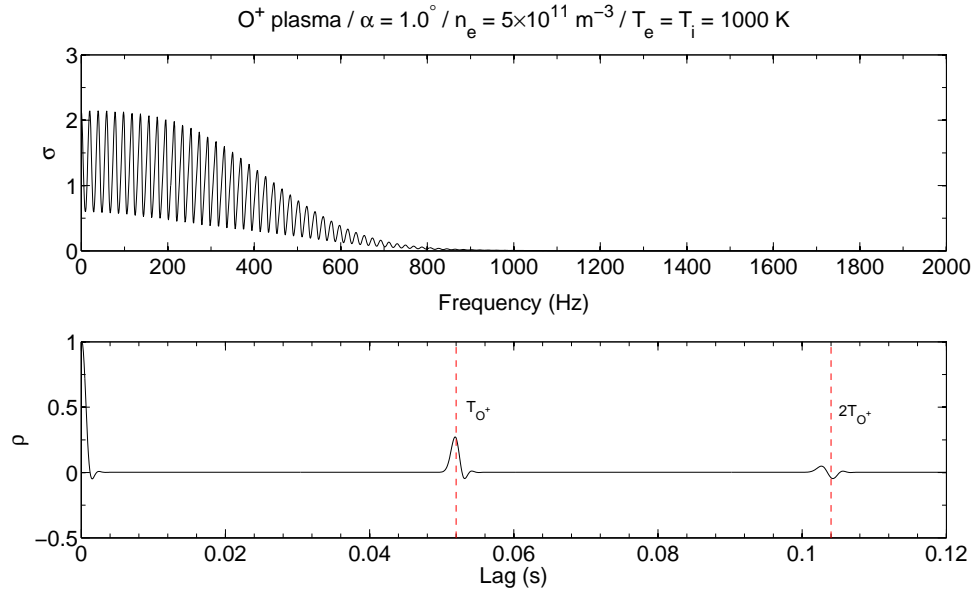


Figure 5.1: IS spectrum calculated for a magnetized collisionless plasma O⁺ (top panel) and the corresponding IS ACF (bottom panel). The dashed lines indicate multiples of the O⁺ gyroperiod (T_{O^+}) for the magnetic field used in the calculation (20,000 nT).

other forces that could suppress such a resonance (Farley, 1967). Fig. 5.1 shows an example of IS spectra calculated for an O⁺ magnetized collisionless plasma (Farley et al., 1961; Salpeter, 1961). The gyroresonance “lines” can be observed in the spectrum and the first gyroresonance peak is shown around the gyroperiod in the ACF.

The first attempts to measure the O⁺ resonance were unsuccessful. Farley (1964) then suggested that the O⁺ gyroresonance would be destroyed by ion-ion Coulomb collisions at *F*-region heights. Thus, because the resonance is effectively destroyed, incoherent scatter calculations near perpendicular usually neglect the gyroresonance effect completely by not including the magnetic field in the calculation of the appropriate ion admittance function (e.g., see Swartz

and Farley, 1979; Pingree, 1990). However, at higher altitudes where densities are lower and Coulomb collisions are less important, observations of the H^+ resonance are still possible. Farley (1967) made the first and the only published observations of the H^+ gyroresonance, showing that under the right conditions, one can measure the H^+ gyroresonance peaks. In his experiment, Farley was able to observe the first three H^+ gyroresonance peaks in the IS ACF. At the time Farley made his measurements, computation of theoretical ACFs was time consuming, especially for small aspect angles, so that computer-based fits of the measured ACFs were virtually impossible. To illustrate the good agreement between his observations and the IS theory including the geomagnetic field, Farley plotted one example of his measured ACFs and a few theoretical ACFs provided by R. Woodman who was working on a full IS theory (Woodman, 1967) and had developed a technique to compute plasma ACFs for small aspect angles.

5.4 Collisional effects on the gyroresonance

In chapter 4, the effects of electron (electron-electron plus electron-ion) Coulomb collisions in the shape of the IS spectrum and radar cross section were investigated. The analysis considered F region altitudes where magnetic field effects on the ions can be neglected, and computation of the ion Gordeyev integral is greatly simplified (Farley, 1964; Pingree, 1990). Electron Coulomb collision effects were taken into account by using a library of the electron Gordeyev integral developed by Sulzer and González (1999) using numerical simulations of the electron motion. In order to study the ion gyroresonance, it is also necessary to take into account ion-ion Coulomb collisions. In this case, the approach recently proposed by Kudeki and Milla (2006) to calculate the ion Gordeyev integral is fol-

lowed.

5.4.1 Gordeyev integral for a magnetized collisional plasma

It was shown in chapter 3 and reviewed in chapter 4 that the IS spectrum can be written in terms of the admittance function for ions and electrons. It was also shown, that for F region heights, the admittance function for each species is given by $y_s = i + \theta_s J_s$, where J_s is the Gordeyev integral for the species s . For a complete analysis of the gyroresonance, a Gordeyev integral that takes into account both the magnetic field and Coulomb collisions will be introduced.

Woodman (1967) derived an expression for the IS ACF that takes into account an external magnetic field and both electron and ion Coulomb collisions. He used a Fokker-Planck like collision operator to model electron and ion Coulomb collisions for the specific case of $T_e = T_i$. *Kudeki and Milla* (2006) generalized the result of *Woodman* (1967) for the case of unequal electron and ion temperatures by matching his result of $\langle |n_e(\omega, \mathbf{k})|^2 \rangle$ to a general expression written in terms of normalized frequencies and Gordeyev integrals. Using this approach, *Kudeki and Milla* (2006) found an analytical expression for the Gordeyev integral that takes into account both electron (electron-electron plus electron-ion) and ion (ion-ion plus ion-electron) collisions:

$$J(\theta_s) = \int_0^\infty dt e^{-j\theta_s t} e^{-\frac{\psi_{st}-1+e^{-\psi_s t}}{2\psi_s^2} \sin^2 \alpha} e^{-\frac{\cos(2\gamma_s)+\psi_{st}-e^{-\psi_s t} \cos(\phi_{st}-2\gamma_s)}{2(\psi_s^2+\phi_s^2)} \cos^2 \alpha} \quad (5.1)$$

where α is the aspect angle, $\theta_s = \frac{\omega}{\sqrt{2}kC_s}$ is the normalized Doppler frequency, $\phi_s = \frac{\Omega_s}{\sqrt{2}kC_s}$ is the normalized gyrofrequency, and $\psi = \frac{v_s}{\sqrt{2}kC_s}$ is the normalized

(Coulomb) total collision frequency for plasma species s . $C_s = \left(\frac{k_B T_s}{m_s}\right)^{1/2}$ is the thermal velocity, $\Omega_s = eB/m_s$ is the gyrofrequency, and $\gamma_s = \tan^{-1}\left(\frac{v_s}{\Omega_s}\right)$ for each plasma species s . The Gordeyev integral becomes that found by *Farley et al.* (1961) for a magnetized collisionless plasma when $\nu_s = 0$ is assumed. The Gordeyev integral in Eq. 5.1 is computed using a Clemshaw-Curtis numerical quadrature algorithm (e.g. *Press et al.*, 1992). In practice, the integration is truncated at a upper limit, even though the upper limit of Eq. 5.1 is indefinite. Fortunately, the second exponential term in the integrand makes the function converge quickly to zero for any reasonable collision frequency value as t increases so that the contribution of the function at very large values of t do not contribute significantly to the integral.

5.4.2 Ion Coulomb collision frequency

Following *Woodman* (1967), the total ion collision frequency for a plasma with a mixture of ions is given by:

$$\nu_s = \frac{e^4 \ln(24\pi\lambda_e^3 N_e)}{4\pi\epsilon_0^2 m_s^{1/2} (2k_B T_s)^{3/2}} \sum_j N_j C_{sj} \quad (5.2)$$

where the summation is over all the charged species including electrons, ϵ_0 is the dielectric constant, k_B is the Boltzmann constant, N_s is the density of species s , and C_{sj} is a dimensionless constant calculated by *Woodman* (1967). Values of C_{sj} are given in Table 5.1. When the plasma is formed by a single ion, Eq. 5.2 becomes the Spitzer collision frequency.

Table 5.1: Values of C_{sj} for different ion mixtures (*Woodman, 1967*).

C_{sj}	H ⁺	He ⁺	O ⁺	electron
H ⁺	0.601	0.853	1.015	0.0176
He ⁺	0.352	0.601	0.854	0.0090
O ⁺	0.185	0.351	0.601	0.0048
electron	1.127	1.128	1.128	0.601

5.4.3 Electron Coulomb collision frequency

While the formulation of *Woodman (1967)* predicts the damping effect of ion-ion collisions in the gyroresonance, it did not predict the additional narrowing of the IS spectrum at small aspect angles (*Sulzer and González, 1999*). More recently, *Woodman (2004)* revisited his calculation and compared ACFs predicted by his formulation and ACFs generated by the numerical simulations of *Sulzer and González (1999)*. He found a better agreement if a higher value of electron Coulomb collisions than predicted by the Spitzer formula is considered. *Woodman (2004)* proposed the following ad-hoc model for the total electron Coulomb collision frequency:

$$\nu_e = \left[1.06 + 7.55 \left(\frac{\sin \alpha}{\sin \alpha_c} \right) - 2.00 \left(\frac{\sin \alpha}{\sin \alpha_c} \right)^2 + 0.27 \left(\frac{\sin \alpha}{\sin \alpha_c} \right)^3 \right] \nu_{e0} \quad (5.3)$$

where $\alpha_c = \sin^{-1} \left(\frac{2\pi\nu_{e0}}{kC_e} \right)$ is a critical aspect angle, and

$$\nu_{e0} = \frac{e^4 N_e}{4\pi\epsilon_0^2 m_e^{1/2} (2k_B T_e)^{3/2}} \ln(24\pi\lambda_e^3 N_e) \quad (5.4)$$

is the Spitzer collision frequency for electrons. In this study, however, the library provided by *Sulzer and González (1999)* was used directly to obtain the electron Gordeyev integral values.

5.5 The collisional IS spectrum

The results of *Sulzer and González (1999)*; *Woodman (2004)*; *Kudeki and Milla (2006)* now make possible an estimation of the IS spectrum at small aspect angles with the effects of both ion and electron Coulomb collisions taken into account. Fig. 5.2 shows the IS spectra for the case of an O^+ plasma at different density values. The IS spectrum for the collisionless case is also shown in every panel for comparison. This plot shows that O^+ gyroresonance lines are heavily suppressed by ion collisions even at low density values. *Farley (1964)* claimed that the O^+ gyroresonance at F region heights would be destroyed by collisions and it would not be observable for any realistic value of ionospheric density. The results in Fig. 5.2 show that except at extremely low densities ($n_e = 10^{10} \text{ m}^{-3}$), the O^+ gyroresonance is not observed. The results also illustrate the effects of electron Coulomb collisions in the width of the IS spectrum. The spectrum is narrower at higher density values.

Fig. 5.3 shows the IS spectra for a H^+ plasma. In this case, a weak gyroresonance can be observed even at relatively large density values ($n_e = 10^{12} \text{ m}^{-3}$). This is justified by the fact that, for the same density and temperature, the ratio of collision to gyrorotation frequency for an O^+ plasma is about 4 times larger than for a H^+ plasma.

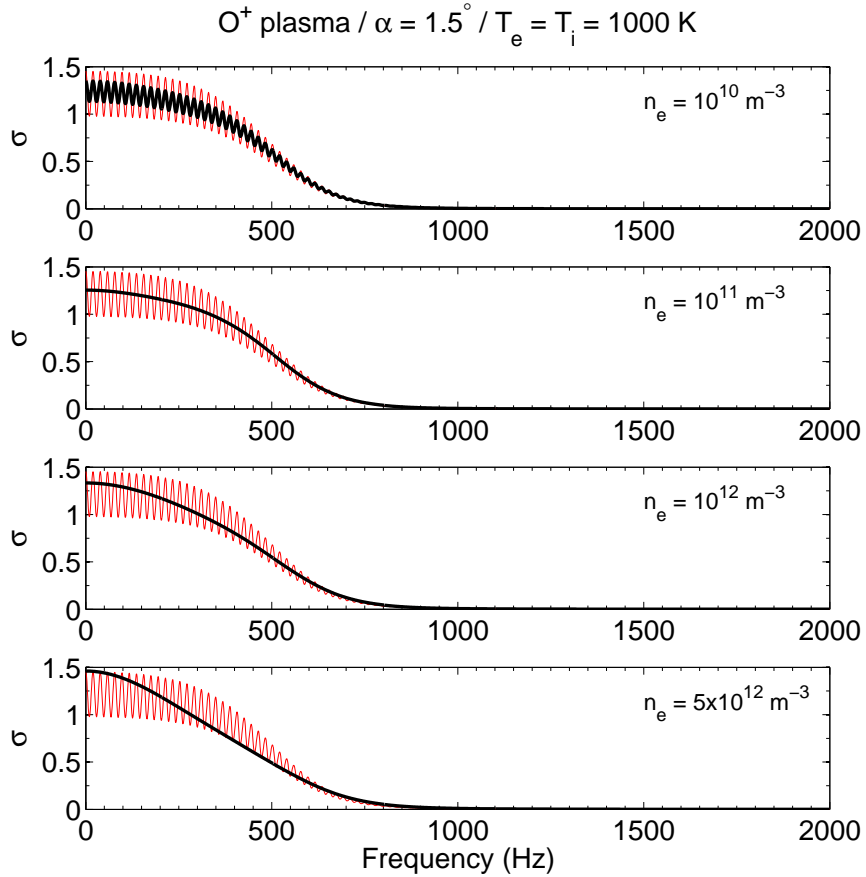


Figure 5.2: Examples of incoherent scatter spectra calculated for a collisional (thick line) and collisionless (thin line) O^+ plasma and for different values of electron density.

5.6 The proton gyroresonance

The shape of the first H^+ gyroresonance peak in the IS ACF varies as a function of aspect angle, ion composition, temperature and density. The aspect angle can be found from geomagnetic field models and a reasonable estimate of the density can be obtained from normalized backscattered power profiles. This encouraged an attempt to estimate temperature and ion fraction from gyroresonance measurements.

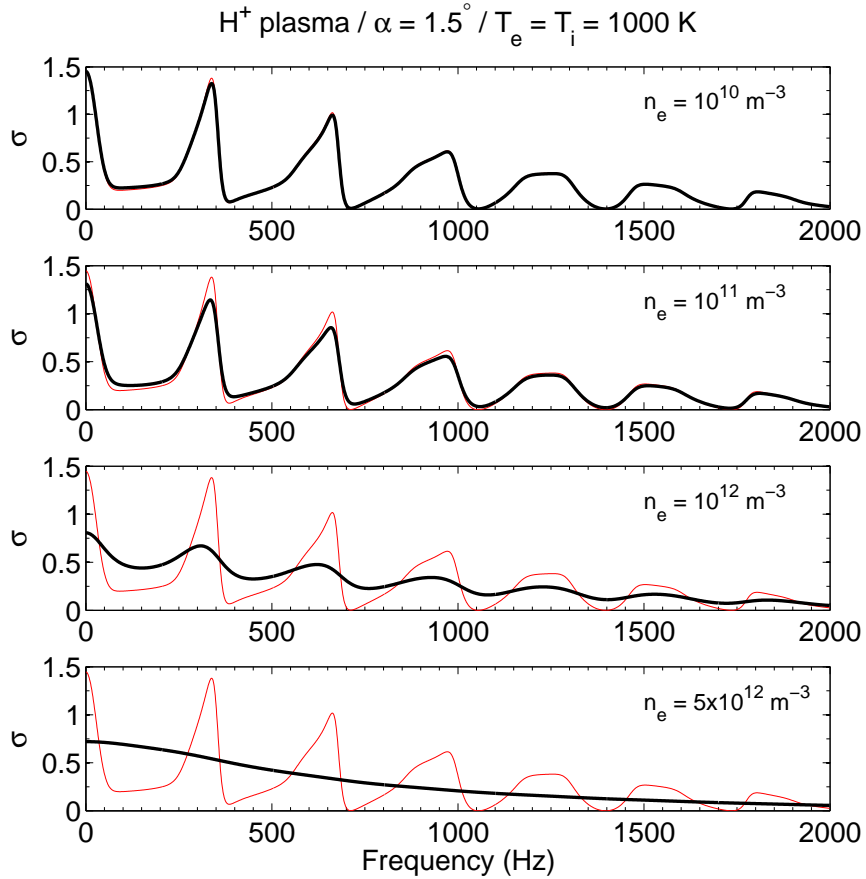


Figure 5.3: Same as Fig. 5.2 but for a H⁺ plasma.

Fig. 5.4 illustrates how the gyroresonance peak in the IS ACF varies as a function of the aspect angle. The first point to be noticed is that the gyroresonance peak increases as the aspect angle decreases. At approximately $\alpha \sim \sqrt{m_e/m_i}$, however, the maximum correlation starts to decrease and the width of the gyroresonance starts to increase. Close to perpendicular, the effective mass of the electron is scaled by a factor $1/\sin^2 \alpha$ so that the electrons appear to have more inertia and cannot shield out the ions as effectively. This role causes the gyroresonance to move to longer lags as the electrons diffuse away more slowly (e.g., *Woodman, 1967*).

Obviously, the fraction of H^+ forming the ionospheric plasma also affects the gyroresonance peak. The peak of the proton gyroresonance increases with the fraction of H^+ ions as shown in Fig. 5.5. In this case, Coulomb collisions were not considered, but they also affect the maximum correlation of gyroresonance as well. Fig. 5.6 shows that as the density increases, the gyroresonance becomes more damped. This is caused by the increase of ion Coulomb collisions and their effect on the gyrotation of the ions. At large densities, the gyroresonance disappears completely. Also, considering an O^+H^+ plasma for instance, an increase in the fraction of H^+ would decrease the total H^+ collision frequency according to Eq. 5.2, therefore causing less damping of the gyroresonance.

During the analysis, it was found that the shape of the gyro resonances is only weakly affected by the amount of electron Coulomb collisions. Nevertheless, electron Coulomb collisions were incorporated in the theoretical model. The main effects of electron Coulomb collisions on the shape of the IS spectrum (or ACF), and its dependence on the aspect angle seem to be exactly those explained by *Sulzer and González (1999)*. Electron Coulomb collisions narrow (broaden) the IS spectrum (IS ACF) and have stronger effects at smaller aspect angles.

Calculations also show that the width of the gyro-peak seems to be controlled by the temperature. The gyroresonance is broader at lower temperature. The ACFs in Fig. 5.7 show the proton gyroresonance for different temperatures. The temperature effect in the gyroresonance peak is weak and it is hardly noticed. The effect in the width is more noticeable, especially when the ACFs for $T = 600$ K and $T = 1800$ K are compared.

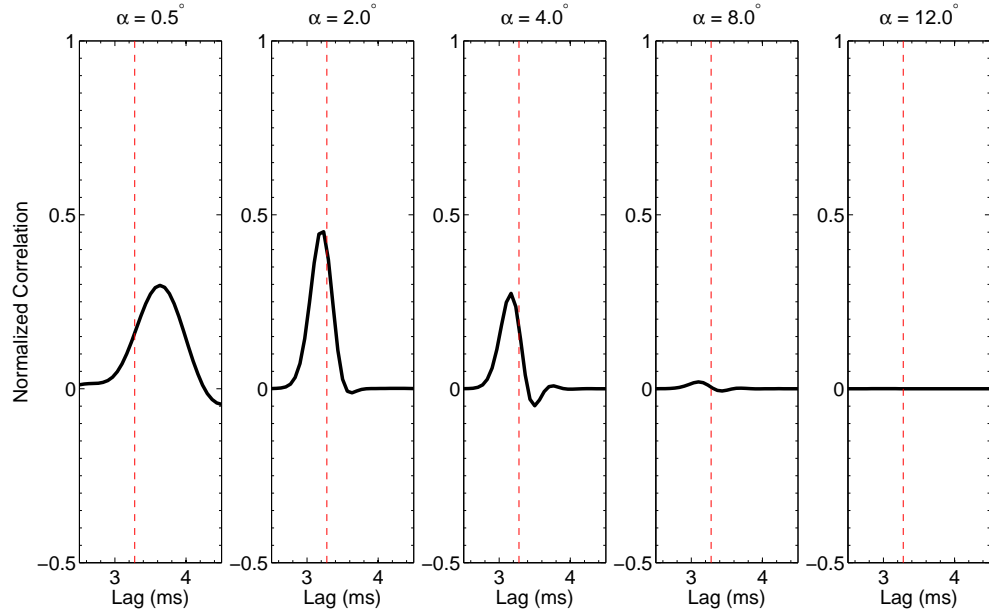


Figure 5.4: Aspect angle effects: First gyroresonance peak in the IS ACF calculated for a collisionless H^+ plasma at different aspect angles ($n_e = 10^{12} m^{-3}$, $T_e = T_i = 1000$ K, $|\mathbf{B}| = 20,000$ nT). The vertical dashed lines indicate the proton gyrorotation period.

5.7 Experiment setup

For observations of the proton gyroresonance, a single-polarization double-pulse setup was used. A single circular polarization was used with two transmitters combined to improve the signal-to-noise ratio of the received echoes. Echoes with both circular polarizations were received, and it was observed that depolarization effects were negligible. The two transmitters combined deliver a peak power of 2 MW. The on-axis configuration (declination -12.88° , hour angle -4.617°) of the Jicamarca antenna was used in order to obtain the best antenna gain. The range-time diagram for the experiment is shown in Fig. 5.9. The dark blocks in the diagram show the regions from where correlated signals come.

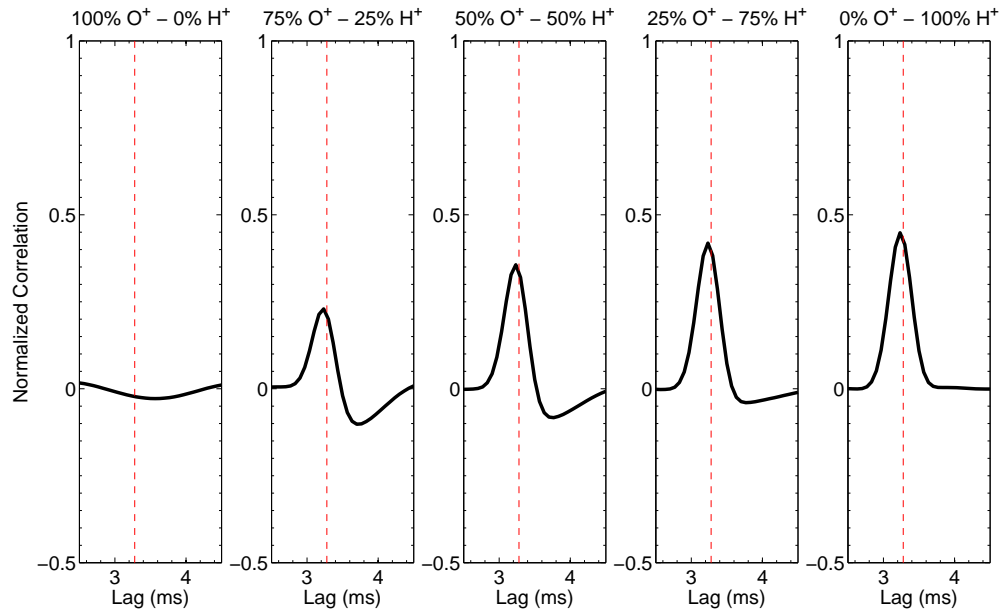


Figure 5.5: Composition effects: First gyroresonance peak in the IS ACF calculated for a collisionless plasma with different composition fractions ($\alpha = 1.5^\circ$, $n_e = 10^{11} \text{ m}^{-3}$, $T_e = T_i = 1000 \text{ K}$, $|\mathbf{B}| = 20,000 \text{ nT}$). The vertical dashed lines indicate the proton gyrorotation period.

Clutter comes from the gray regions above and below the range of interest. The clutter from above is weaker than the signal of interest and does not greatly affect the measurements. Clutter from below, in the other hand, contains stronger coherent echoes from bottom-type layers that are frequently observed after sunset in the bottomside F region.

The expected proton gyroperiod was calculated using values of the geomagnetic field from the International Geomagnetic Reference Field (IGRF) model for ranges along the line-of-sight of the radar in the Jicamarca standard on-axis position. The gyroperiod varies between 3 and 4 milliseconds (ms) for topside (550-1000 km) ranges. Fig. 5.8 shows the geomagnetic field values as a func-

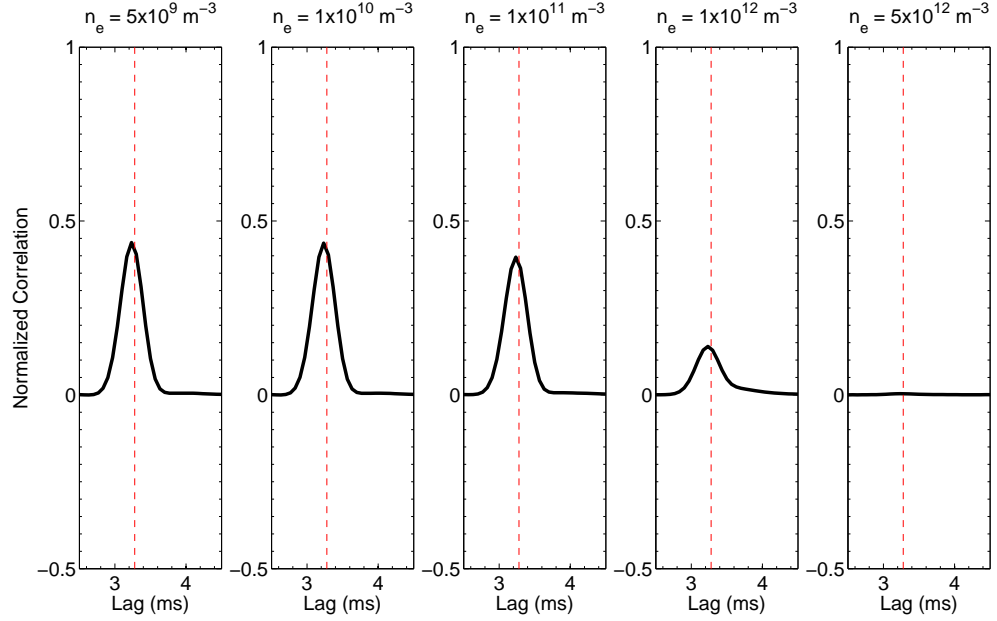


Figure 5.6: Density effects: First gyroresonance peak in the IS ACF calculated for a H^+ plasma with different density values ($\alpha = 1.5^\circ$, $T_e = T_i = 1000$ K, $|\mathbf{B}| = 20,000$ nT). The vertical dashed lines indicate the proton gyrorotation period.

tion of range along with the corresponding proton gyroresonance period and the angle the wave vector of the transmitted wave makes with the geomagnetic field for the on-axis antenna configuration. The aspect angle becomes very small (varying from 1.5 to 1.0 degrees) in the 550-1000 km range, and electron Coulomb collisions can become an important factor in determining the shape of the IS spectrum.

Based on the estimates of the proton gyroperiod from the IGRF model, five equally spaced lags between 3.1 and 3.9 ms were chosen to be measured with the double pulses. The zero lag (power) was measured with a single pulse before each transmission of the set of five double pulses. The single pulse provides

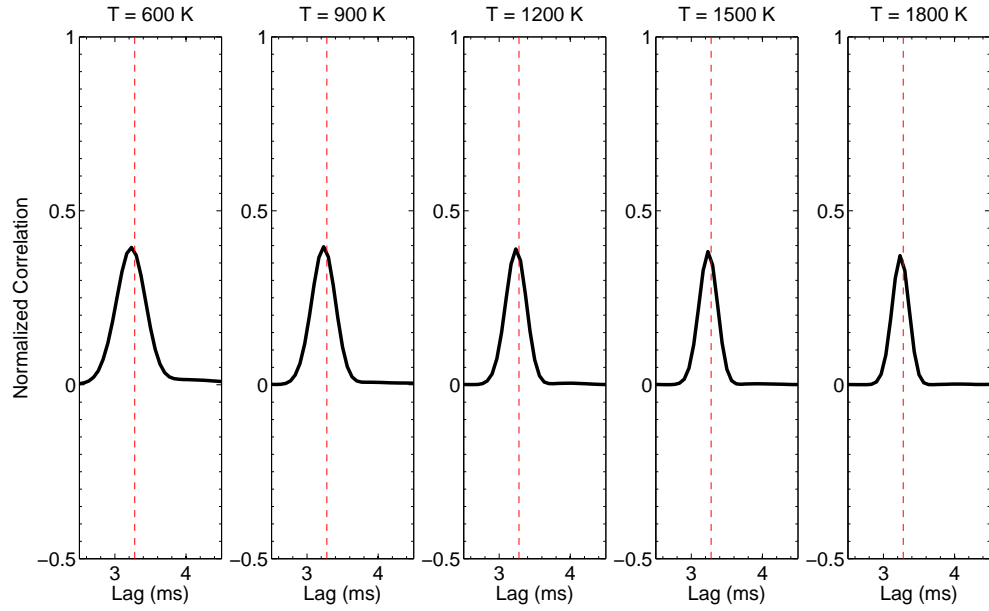


Figure 5.7: Temperature effects: First gyroresonance peak in the IS ACF calculated for a H^+ plasma at different temperatures ($T = T_e = T_i$, $\alpha = 1.5^\circ$, $n_e = 10^{11} m^{-3}$, $|\mathbf{B}| = 20,000$ nT). The vertical dashed lines indicate the proton gyrorotation period.

normalization for the measured ACF, and combined with digisonde measurements of f_0F2 , gives electron density estimates for the F region and topside. Measurements were made at night when $T_e \sim T_i$, and the radar cross section correction is not necessary. The pulses used in this experiment were 0.5 ms (75 km) long, and the interpulse period was 2500 km. The sampling frequency was 20 kHz, giving range gates every 7.5 km.

5.7.1 ACF estimator

The estimator used for the normalized ACF (ρ) is given by:

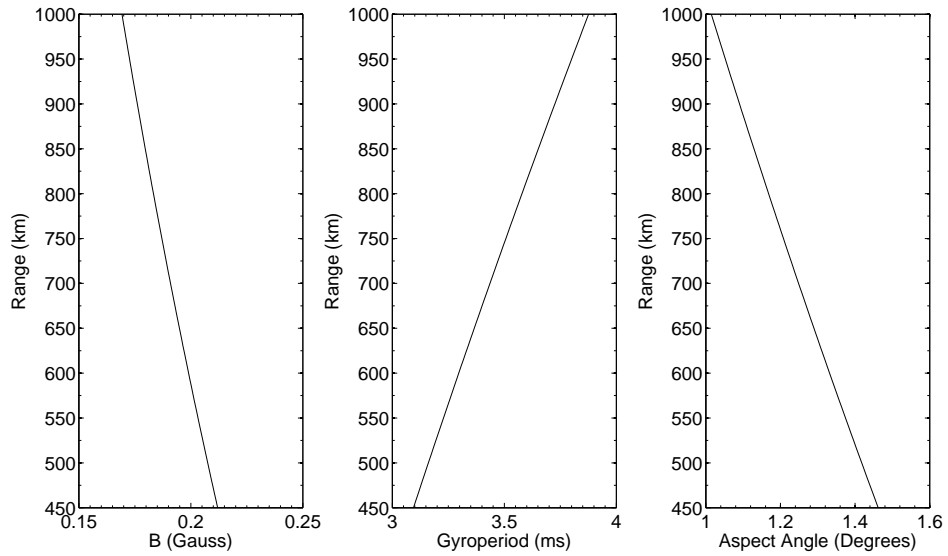


Figure 5.8: Geomagnetic field intensity, gyroperiod and aspect angle as a function of range along the radar line-of-sight for the pointing position used in the gyroresonance experiment

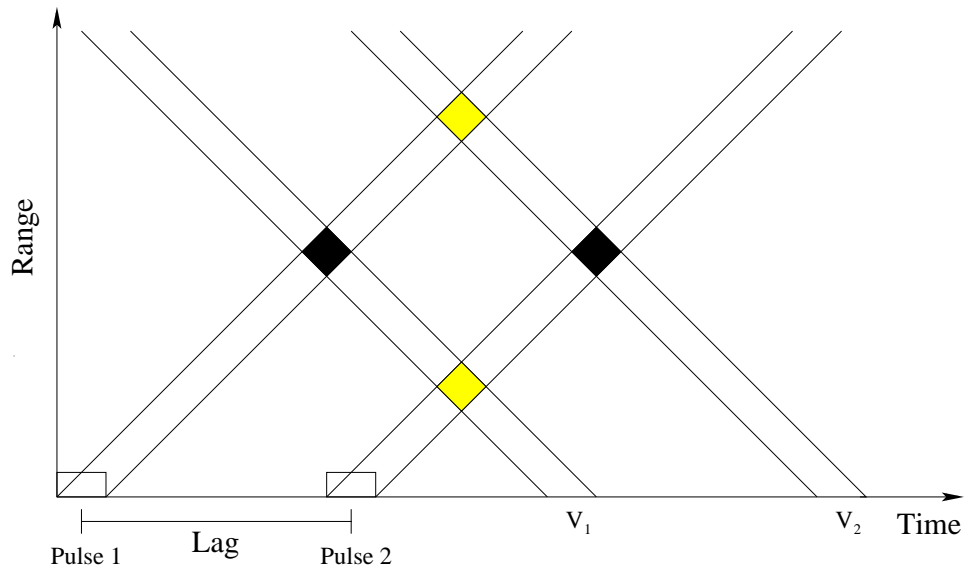


Figure 5.9: Range-time diagram for the single-polarization double-pulse experiment used for the gyroresonance observations.

$$\hat{\rho} = \frac{\hat{R}}{\hat{S}} \quad (5.5)$$

where \hat{R} is the unnormalized correlation estimator:

$$\hat{R} = \frac{1}{K} \sum_{i=1}^K V_i(t) V_i^*(t + \tau) \quad (5.6)$$

and \hat{S} is the signal power estimator:

$$\hat{S} = \frac{1}{K} \sum_{i=1}^K |V_i(t)|^2 - \frac{1}{K_n} \sum_{i=1}^{K_n} |V_{ni}(t)|^2 \quad (5.7)$$

where $V_i(t)$ and $V_i(t + \tau)$ are complex voltage samples spaced by the time delay τ and $V_{ni}(t)$ are noise voltage samples. K is the number of samples used in the correlation and power estimation, and K_n is the number of samples used in the noise power estimation.

The voltages used for the correlation and power estimation are independent. The correlation estimation uses voltages from the double-pulse transmissions and the power estimator uses voltages from the single-pulse transmissions. Noise samples come from the highest range gates, and $K_n \gg K$. It can be shown that these two estimators are unbiased, meaning that their expected values correspond to the true values of correlation and power ($\langle \hat{R} \rangle = R$ and $\langle \hat{S} \rangle = S$). When noise and clutter are taken into consideration, and when the voltage samples used to estimate the power are independent of the signal samples used to estimate the signal correlation, the variance for the normalized ACF is given by (Farley, 1969a):

$$\langle |\hat{\rho} - \langle \hat{\rho} \rangle|^2 \rangle \approx \frac{1}{K} \left(\frac{S + N + C}{S} \right) (1 + |\rho|^2) \quad (5.8)$$

where S , N and C are the signal, noise and clutter power, respectively. While S and N are obtained from the power profile of the single-pulse transmissions, estimates of C for each measured lag are obtained from the power profile of the double-pulse transmissions. In order to eliminate or at least minimize the effects of coherent echoes caused by satellites and space debris in the estimator of the ACF, short-time integration ACFs were computed and sorted out first, and outliers were removed.

5.8 Experiment results

The gyroresonance experiment was conducted in the evenings of October 9 and 10, 2006. A major difficulty of an experiment of this type is clutter (i.e., unwanted signals) from the F region, coherent echoes from spread F , and satellites/space debris. The former contaminant is pulse-to-pulse clutter resulting from the long spacings required to measure the appropriate lags. This clutter is removable to some degree. Unfortunately, on both nights equatorial spread F events were observed. Spread F started with a bottom-type layer around 1930 LT and developed into coherent scatter radar plumes reaching the topside ionosphere. Spread F reached the topside ionosphere at around 2130 LT, making gyroresonance observations impossible after this time. However, it was possible to use data from the early evening hours after eliminating data affected by satellites and space debris.

The proton gyroresonance was observed on both nights, but clearer examples of the first gyroresonance were obtained on October 9. Fig. 5.10 shows a profile of gyroresonance measurements during the evening of October 9. The figure shows measured ACFs as a function of range together with measurement errors. Horizontal dashed lines indicate the zero correlation level for each ACF, and the vertical spacing between dashed lines correspond to a correlation of 0.5. The diagonal solid line shows the gyroperiod as a function of range.

The ACFs are a result of a 40-minute incoherent integration. Lags with large error bars were removed from the plot. It can be observed that longer lags in the lowest ranges have larger error bars. This is because these lags are more strongly affected by the coherent echoes coming from coherent scattering layers at lower ranges. The peaks in the ACFs are in good agreement with the gyroperiod in almost every range gate. The maximum correlation seems to increase with altitude, indicating an increase in the H^+ fraction with height, as expected. The gyroresonance peak could not be detected below 550 km or above 850 km. Error bars below 550 km were too large, and it is likely that there was no detectable H^+ below that altitude. The sensitivity of the experiment was too low for detection above 850 km.

5.9 Temperature and composition estimates

The measurements shown in the previous section indicate the detection of the proton gyroresonance. However, the uncertainties in the measured lags are larger than what was anticipated due to the presence of strong coherent echoes (clutter) coming from lower ranges. The uncertainties in the measurements

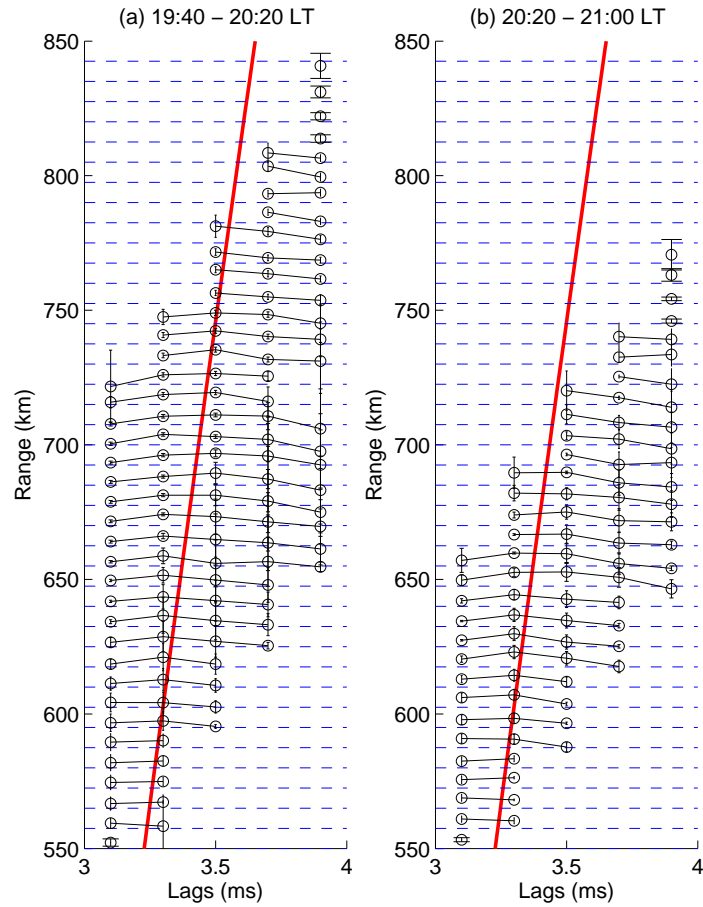


Figure 5.10: (a) Incoherent scatter autocorrelation functions measured on October 9, 2006 (1940-2020 LT). The solid diagonal line shows the values of the gyroperiod based on IGRF. The vertical spacing between dashed lines correspond to a correlation of 0.5. (b) Same except for 2020-2100 LT.

could be reduced by increasing the integration time. The ionospheric parameters (temperature, ion composition and total density), however, would vary greatly over a longer period of time, and the resulting ACFs might not correspond to any theoretical ACF.

Nevertheless, an error-weighted general least-squares method was used to find theoretical curves that best fit the measurements. Fits were constrained to the isothermal case ($T_e = T_i$), which is a reasonable assumption at night. The fits were also carried out using the aspect angle and magnetic field intensity obtained from the IGRF model. It is difficult to calculate the uncertainty of the geomagnetic model, but the accuracy is expected to be within a few percent. Topside electron density estimates were obtained from the profiles of the signal power measured by the radar and calibrated by the F -peak electron density (f_0F2) measured by the Jicamarca digisonde.

Fig. 5.11 shows example ACFs measured in consecutive range gates and the respective best fits to the data. The best fit ACFs match the data within the error bars. The fraction of H^+ resulting from the fits varies between 30 and 45%, while the temperature varies between 750 and 1550 K for ranges varying from approximately 650 to 710 km. Both the temperature and the fraction of H^+ seem to increase with altitude. The uncertainties for the estimated parameters are in agreement with the variability of the results. These errors, however, do not take into account the uncertainties in density and magnetic field. The larger variability of the estimated temperatures is a consequence of its dependence on the width of the gyroresonance, which is difficult to be accurately estimated with only five lags especially with the uncertainty of the measurements presented here.

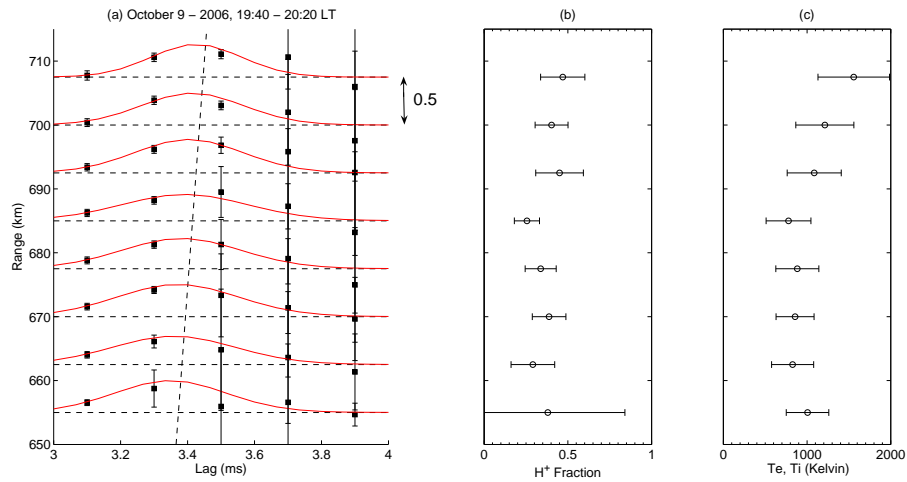


Figure 5.11: (a) Examples of the least-squares best fits (solid lines) for a set of gyroresonance measurements (square marks) on October 9 2006, 1940-2100 LT (see scale on the top right side of the panel). Inverted H⁺ fractions and temperatures are shown in panels (b) and (c), respectively.

The International Reference Ionosphere (IRI) model predicts H⁺ fraction between 46% and 58% and ion temperature between 889 and 910 K in the 650-710 km altitude range over Jicamarca on October 9, 2006. The estimated temperatures and ion fractions are reasonable values even though the measurements were made in less than optimal conditions. It is possible that more accurate information can be obtained during periods free of coherent echoes.

5.10 Summary

Despite the clutter from *F* region IS echoes and bottom-type spread *F*, the first peak of the proton gyroresonance could be measured at Jicamarca. The observed gyroresonance is in agreement with the gyroperiod predicted by the

IGRF model and theoretical predictions of the magnetized and collisional IS theory. The observations were limited to periods before spread F radar plumes appeared. Radar plumes contaminate the topside data with strong coherent echoes. Coherent echoes from bottom-type layers, however, were an unavoidable, strong source of clutter during the observations resulting in relatively large error bars in the measured ACFs. Nevertheless, theoretical curves that best fit the measurements were found. Reasonable values of temperature and H^+ fraction were obtained from the fits. The fitting procedure takes into account both ion and electron Coulomb collisions, both of which affect the IS ACFs at small aspect angles. It is believed that for periods with reduced clutter (from coherent echoes at lower ranges), the gyroresonance can be measured with higher accuracy, and the uncertainties in the estimated parameters can be reduced. Although, successful detection of the gyroresonance was possible, the results indicate difficulties in using this experiment as an operational mode for topside studies at Jicamarca. The sensitivity of this experiment is relatively low compared to the measurements made with the full-profile technique applied to long uncoded pulse soundings, recently implemented at Jicamarca (*Hysell et al., 2008*).

CHAPTER 6

COHERENT BACKSCATTER RADAR IMAGING OBSERVATIONS OF LARGE-SCALE WAVES AT THE ONSET OF EQUATORIAL SPREAD F

6.1 Introduction

The ionospheric collisional interchange instability, also referred to as the Generalized Rayleigh-Taylor (GRT) instability, operates in the bottomside equatorial F region and is usually invoked to explain the observations of density irregularities in the nighttime equatorial F region (Kelley, 1989). The manifestation of these irregularities in a number of different types of sensors are referred to simply as equatorial *spread F* . Observations have shown that electron density irregularities with scale-sizes ranging from a few cm to hundreds of km can be detected during spread F events. Typical equatorial spread F events are first observed in postsunset hours in the bottomside F region at the magnetic equator. In some cases, large-scale ionospheric plasma depletions can reach the topside ionosphere. These large-scale spread F events are responsible for signal disruption in satellite-based communication and navigation systems (e.g., Kintner *et al.*, 2001). Therefore, forecasting the occurrence of spread F events, which have a high day-to-day variability, has been the subject of numerous research efforts. The magnitude of fluctuations in the amplitude (amplitude scintillations) of the GPS signal (L1 = 1.575 GHz) measured at a number of stations in Brazil are shown in Fig. 6.1. These measurements illustrate the impact of spread F on satellite-based systems and motivates the study of equatorial spread F .

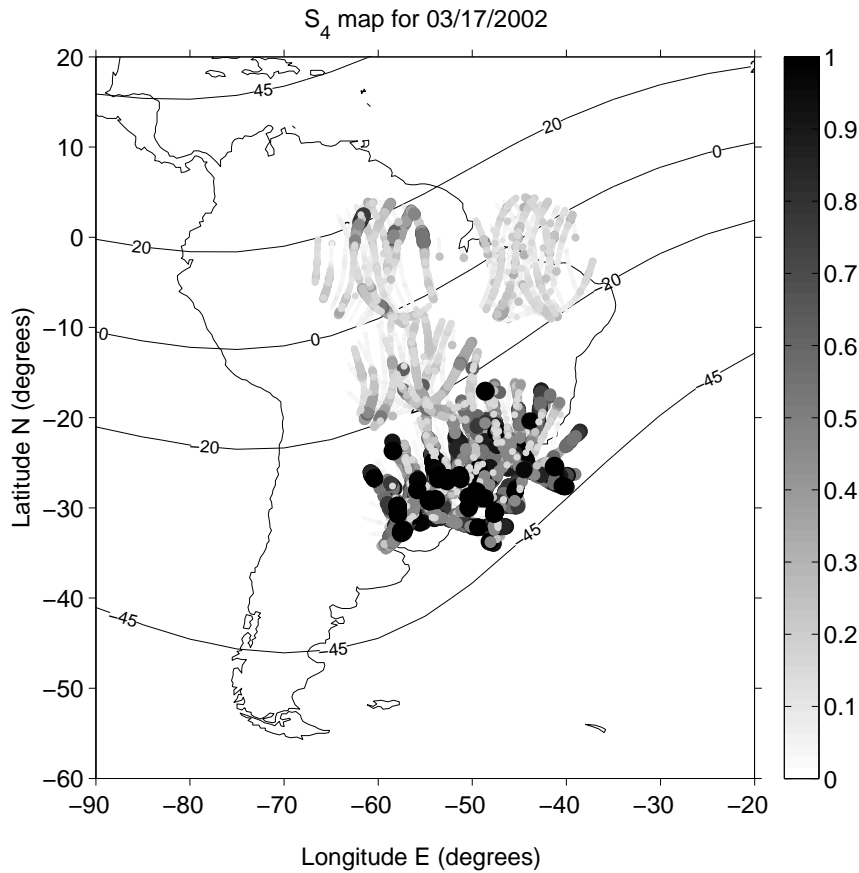


Figure 6.1: Amplitude scintillations measured with GPS-based scintillation monitors in Brazil. The S_4 is a widely used scintillation index defined as the power variance normalized by the average power. Scintillation is particularly strong near the Appleton Anomaly region where F region densities are higher. GPS signal tracking can be lost by the receiver during strong scintillation events.

6.1.1 Development of equatorial spread F

The generalized or ionospheric Rayleigh-Taylor (GRT) instability is the plasma analog to the Rayleigh-Taylor (RT) instability acting in neutral fluids. The RT instability will take place, for instance, in the case of a dense fluid on top of a lower density fluid. This configuration is in unstable equilibrium, and a small pertur-

bation causes the denser fluid to descend under the action of gravity, making the low density fluid convect upward.

At night, the upward electron density gradient in the bottomside of the equatorial F region is large due to the absence of solar ionization and the fast recombination of molecular ions. *Dungey* (1956) first noticed that this configuration resembles the situation where a dense fluid rests on top of a lighter fluid. In this case, however, the neutral fluid is substituted by the ionospheric plasma and forces other than gravity and pressure gradient act on the plasma. A small density perturbation in the bottomside F region would cause a convective motion of the plasma similar to that in a hydrodynamic RT instability. In the ionospheric case, the convection is not directly driven by gravity but by polarization electric fields generated by horizontal currents and conductivity gradients.

6.1.2 Local linear growth rate

Fig. 6.2(a) illustrates the plasma configuration in the equatorial F region in the post-sunset hours. There is an accentuated upward density gradient in the bottomside F region and a current density \mathbf{J} that is perpendicular to \mathbf{B} in the eastward direction. The current considered here is mainly driven by gravity. Background electric field and neutral winds are not considered for simplicity. If a small perturbation in density is considered as illustrated in Fig. 6.2(b), a perturbation electric field \mathbf{E}_1 will arise. The perturbation electric field will lead to a Pedersen current, and the total current density is given by:

$$\mathbf{J} = \sigma_p \mathbf{E}_1 + \frac{ne}{\Omega_i} \mathbf{g} \times \hat{\mathbf{B}} \quad (6.1)$$

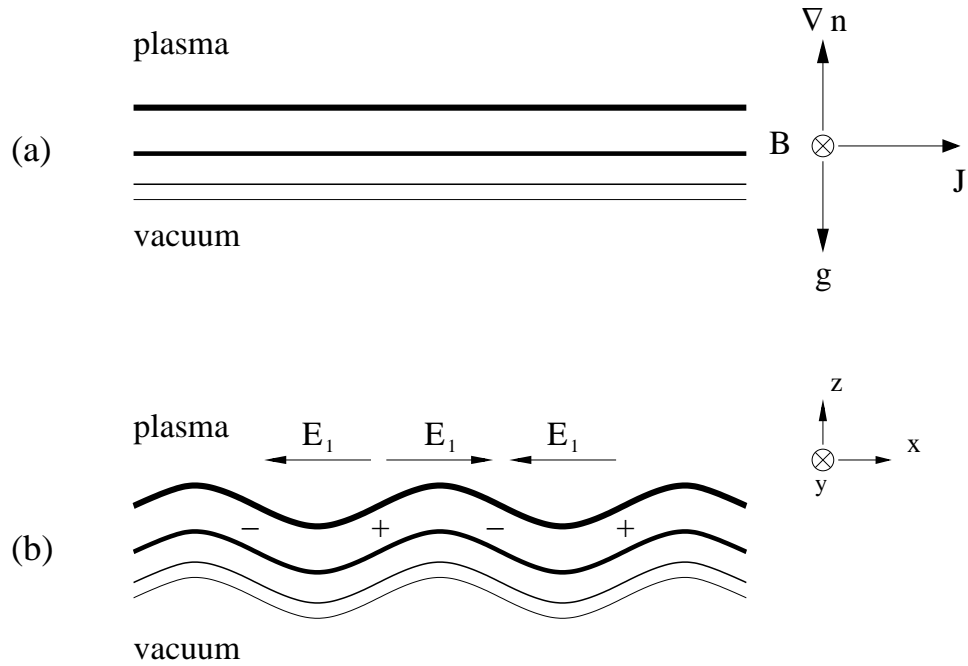


Figure 6.2: Illustration of density perturbations in the bottomside F region and the generation of polarization electric fields causing the convection of low density plasma upward.

One can combine the continuity equation for an incompressible plasma and the divergence-free current condition to derive a dispersion relation for the density fluctuations. The equations are linearized assuming small perturbations of the form:

$$\begin{aligned}\phi(x) &= \phi_1 e^{j(\omega t - kx)} \\ n(z, x) &= n_0(z) + n_1 e^{j(\omega t - kx)}\end{aligned}$$

where $\mathbf{E}_1 = -\nabla\phi$. The dispersion relation found is given by (e.g. Kelley, 1989):

$$\omega = k \left(\frac{m_i g e}{B} \right) - j \frac{g}{v_{in}} \left(\frac{1}{n_0} \frac{\partial n_0}{\partial z} \right) \quad (6.2)$$

This result shows that for positive (upward) density gradients, the amplitude of the perturbation grows in time with a linear growth rate given by:

$$\gamma = \frac{g}{v_{in}} \left(\frac{1}{n_0} \frac{\partial n_0}{\partial z} \right) \quad (6.3)$$

This simple but illustrative calculation can explain some of the features of spread F events. Spread F usually occurs when large pre-reversal enhancements of the zonal electric field are observed. The large zonal electric field moves the F region to higher altitudes where the v_{in} is lower and the growth rate is larger. Spread F also starts in the bottomside F region around post-sunset when positive (upward) large density gradients are observed. The linear growth rate gives the exponential rate at which density perturbations will grow as long as their amplitudes remain small. Beyond this point, a numerical nonlinear model is necessary to follow the development of these perturbations (*Retterer et al., 2005*).

6.1.3 Flux-tube integrated linear growth rate

The zonal electric field and neutral winds were also found to be important in the linear growth rate of the generalized RT instability. The term “generalized” originates from the fact that a number of destabilizing factors other than gravity

contribute the instability. Additionally, the variation of ionospheric parameters along magnetic flux tubes play an important role in the linear growth rate. Following the flux-tube integration formalism (e.g. *Haerendel et al., 1992*), *Sultan (1996)* derived an expression for the linear growth rate of the generalized RT instability:

$$\gamma = \frac{\Sigma_P^F}{\Sigma_P^E + \Sigma_P^F} \left(V_p - U_L^P + \frac{g_L}{\nu_{eff}^F} \right) K^F \quad (6.4)$$

where, g_L is the vertically downward acceleration due to gravity at the magnetic equator and on a field line designated by the McIlwain parameter L : $g_L = g_0/L^2$, where g_0 is the ground value of the gravity acceleration; V_p is the upward component of plasma drift due to eastward magnetic field E_0 at the magnetic equator: $V_p = L^3 E_0/B_0$, where B_0 is the value of geomagnetic field on the Earth's surface; U_L^P is the vertically upward component of neutral wind velocity perpendicular to B weighted by the flux-tube integrated Pedersen conductivity Σ_P . ν_{eff}^F is the flux-tube integrated effective F-region ion-neutral collision frequency, weighted by the number density in the flux tube; Σ_P^E and Σ_P^F are the contributions to the flux-tube integrated Pedersen conductivity from the E and F regions; and K^F is the F region flux tube electron content height gradient.

Eq. 6.4 shows that a number of different factors can affect the GRT growth rate. These factors include, for instance, the occurrence of sporadic E layers at low latitudes, neutral winds, and the intensity of the zonal electric field in the equatorial F region. These factors seem to have a high day-to-day variability, which would explain, at least partially, the observed day-to-day variability of spread F . Direct measurements or indirect estimates of these various param-

ters is a subject of ongoing research.

6.1.4 Triggering mechanism

Even though favorable conditions for the GRT instability growth can be found in the equatorial ionosphere during postsunset hours, an initial perturbation in the Pedersen conductivity might be necessary to trigger spread F in view of the relatively modest growth-rate of the instability. Large density perturbations would give a “head start” to spread F development. Atmospheric gravity waves are often invoked to explain the existence of such perturbations. Theories propose that gravity wave wind fields can directly modulate the electron density in the bottomside F region (e.g., Kelley *et al.*, 1981; Vadas and Fritts, 2004) or can modulate the conductivity of thin E region layers at low latitudes creating perturbation electric field (e.g., Prakash, 1999). These electric fields then map along magnetic field lines to the equatorial bottomside F region. Direct measurements of atmospheric winds in the lower thermosphere are rarely available, however, making it difficult to determine the actual role of the gravity waves in the seeding process.

In order to further investigate the role of gravity waves in seeding equatorial spread F , a multi-instrumented campaign of aeronomical observations was conducted in Brazil between September and November of 2005. The spread F Experiment (SpreadFEx) campaign is part of an observational and theoretical collaborative effort between several universities and institutes in the US and Brazil. During the campaign, a number of instruments for aeronomical observations were operated simultaneously. The set of instruments included optical

systems for nighttime airglow observations (photometers and all-sky imagers), dual frequency-receivers GPS for total electron content (TEC) measurements, GPS-based scintillation monitors, and digisondes. These instruments were distributed at a number of locations over the Brazilian territory. Besides ground-based observations, satellite measurements made with the Global Ultraviolet Imager (GUVI) onboard the TIMED satellite, and other instruments onboard the CHAMP satellite will eventually be used to characterize both the neutral atmosphere and the ionosphere during the campaign. The SpreadFEx campaign not only allowed a multi-instrumented investigation of gravity wave activity and their impact on spread F , but also gave the opportunity to study other plasma processes that can be connected with equatorial spread F .

The coherent backscatter radar installed at São Luís near the magnetic equator in Brazil also made observations of F region irregularities in support to the SpreadFEx campaign. This radar probes small-scale (5-meter) irregularities matching the Bragg condition for the operating frequency of 30 MHz. The radar has been making conventional coherent scatter radar and basic two-antenna interferometric observations of E and F region irregularities since 2001. In 2005, the radar was upgraded, and two more antenna modules were added to the system. A total of four antenna modules became available, with the possibility of six nonredundant antenna baselines for interferometry purposes. Since then, the construction of in-beam radar images of the scattering layers has been possible.

In this chapter, signatures of a large-scale wave (~ 35 km) in the radar images of a strong bottom-type layer detected on October 25 2005 are examined. Bottom-type scattering layers presumably occur as frequently during the spread

F season in Brazil as they do over Jicamarca, in Peru. However, they are not so often observed with detectable signal-to-noise ratio (SNR) levels with the low-power radar in São Luís, especially during periods of low solar flux. This makes radar imaging studies more difficult since the resolution of the images depend on the SNR of the echoes. The event of October 25 combined with the wide field-of-view of the São Luís radar gave us a rare opportunity to investigate the structure of bottom-type layers with a larger angular coverage than was previously possible in other radar imaging experiments (*Hysell et al.*, 2004a; *Hysell and Chau*, 2006a).

6.2 Experimental setup

A 30 MHz coherent backscatter radar is installed at the São Luís Observatory (2.59° S, 44.21° W, -2.35° dip lat) in Brazil. This radar uses two 4-kW peak-power transmitters for observations of small-scale (5-meter) field-aligned electron density irregularities. Initially, only two antenna modules arranged side-by-side in the magnetic east-west direction were available for transmission and reception. Each antenna module is composed of an array of 4×4 Yagi antennas. With two antenna modules, only standard coherent backscatter observations and basic two-antenna interferometry were possible. Nevertheless, these two modules allowed real-time spread F monitoring and measurements of the zonal as well as vertical drift velocity of the scattering structures at the magnetic equator in Brazil (e.g., *de Paula and Hysell*, 2004a; *de Paula et al.*, 2004; *Rodrigues et al.*, 2004b).

In order to perform radar imaging observations, two more antenna modules were added to the radar system in 2005. Fig. 6.3 shows a diagram with the

disposition of the four antenna modules. The antenna modules are aligned with the magnetic east-west direction. Modules A and B in Fig. 6.3 are the original antenna modules and are used both for transmission and reception. Modules C and D are the new antenna modules and are used for reception only. The set of four independent antenna modules can be used to perform interferometry with 6 nonredundant baselines, with baseline lengths varying from 25 to 150 m (2.5 to 15 λ). The locations of the modules were chosen to give an approximately uniform distribution of baseline lengths. Observations were made with 28-bit binary phase coded pulses.

Table 6.1 lists the main parameters for spread F radar imaging observations in São Luís. Parameters for radar imaging experiments at Jicamarca are also shown for comparison. Jicamarca is a much larger radar system and can provide higher resolution images. Usually at Jicamarca, imaging experiments use the north and south quarters of the main antenna for transmission and the modules (64ths of the array) for reception. Each module is formed by a 12 \times 12 array of crossed dipoles.

6.3 Interferometric radar imaging

The use of radar interferometry in ionospheric studies was introduced by *Woodman* (1971). *Farley et al.* (1981) and *Kudeki et al.* (1981) used radar interferometry to study E and F region electron density irregularities, respectively. *Kudeki and Sürücü* (1991) generated the first interferometric images of equatorial electrojet irregularities. More recently, *Hysell* (1996b) combined radar interferometry and the maximum entropy method to obtain higher resolution radar images.

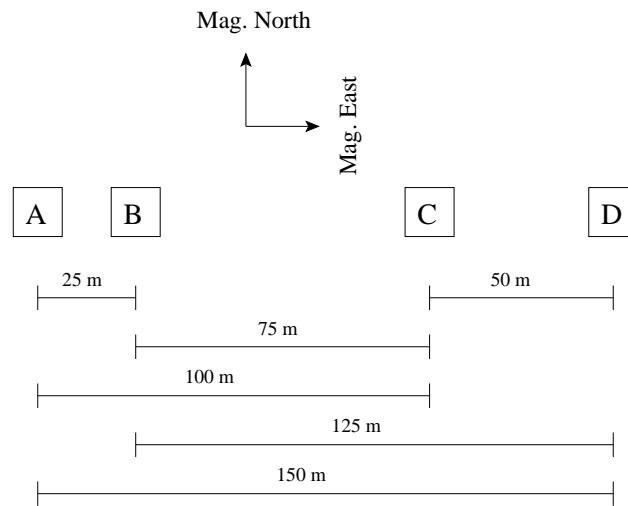


Figure 6.3: Diagram showing the disposition of the four (A, B, C and D) antenna modules. The modules are aligned in the magnetic east-west direction.



Figure 6.4: Antenna arrays at the São Luís radar in Brazil.

Table 6.1: Radar parameters for equatorial spread F imaging observations. Jicamarca parameters are also shown for comparison purposes (*Hysell et al., 2004a*).

Parameter	São Luís	Jicamarca
Peak power	8 kW	100 kW - 1 MW
Number of baselines	6	28
Baud length	2.5 km	300 m
Code length	28 bits	28 bits
In-beam image angular coverage	$\sim 16^\circ$	$\sim 8^\circ$
In-beam image angular resolution	0.4°	0.1°

6.3.1 Inversion algorithm

The algorithm described in *Hysell (1996b)* was used in this study to construct interferometric images of the scattering layers. Here, only a summary of the technique is given, and the reader is referred to *Hysell (1996b)* and *Hysell and Chau (2006a)* for a more complete mathematical derivation.

There is a mathematical relationship between the real valued function f that describes the angular distribution of radar scatterers and the complex cross spectrum g computed from signals arriving at two antennas spaced by a distance d :

$$g(kd, \omega) = \int \frac{d\psi}{\sqrt{1 - \psi^2}} f(\psi, \omega) A(\psi) e^{ikd\psi} \quad (6.5)$$

where, k is the radar wavenumber, d is the antenna separation, which in this

case is taken to be perpendicular to the magnetic meridian, ω is the Doppler frequency, ψ is approximately the zenith angle in the magnetic equatorial plane, and $A(\psi)$ is a function representing the antenna pattern in the magnetic east-west direction. Adopting the notation used in Astronomy and followed by *Hysell* (1996b), g is referred to as the visibility function and f the brightness distribution. Eq. 6.5 shows that f and g are related by an expression similar to a continuous spatial Fourier transform.

In radar imaging, $f(\psi, \omega)$ is sought, the true angular distribution of the Doppler shifted backscattered signals in each radar range gate and for each incoherent integration period. With n antenna modules available, it is possible to obtain estimates of g for $M = n(n - 1)/2$ nonredundant baselines. Generally, g is incompletely sampled, and finding f given a limited, noisy data-set becomes a typical example of an inverse problem.

To obtain an estimate of $f(\omega, \psi)$, the maximum entropy (MaxEnt) approach for image reconstruction is used. With this technique, one searches for the brightness distribution that maximizes the Shannon (or information) entropy constrained by the measurements and their uncertainties. The discrete version of the Shannon entropy of the brightness distribution is given by:

$$S = - \sum_i f_i \ln(f_i/F) \quad (6.6)$$

where, $F = \sum_i f_i$ is the total brightness. Maximizing the entropy is equivalent to finding the brightness that is the most likely to have occurred in a random process. In image reconstruction, the entropy can be interpreted as a smoothness measure.

Given M non-redundant interferometric baselines, it is possible to obtain $2M + 1$ independent measurements of the visibility. These data points correspond to the real and imaginary parts of a component of g plus the absolute power. Therefore, for each baseline with a separation distance d_j , there is a measurement g_j with a random uncertainty e_j added to it. The relationship between the visibility and brightness can be written as:

$$g_j + e_j = \sum_i f_i h_{ij} \quad (6.7)$$

where h_{ij} is either the real or the imaginary part of the interferometer point spread function $e^{jkd_j\psi_i}$. The brightness distribution that maximizes S while being constrained by the data is the extremum of the functional:

$$E[f(\lambda_j)] = S + \sum_j \lambda_j (g_j + e_j - \sum_i f_i h_{ij}) + \Lambda \sum_j (e_j^2 \sigma_j^{-2} - \Sigma) \quad (6.8)$$

where λ_j are lagrange multipliers enforcing data constraints and Λ is another lagrange multiplier enforcing a constraint on the error norm Σ . The σ_j^2 are the theoretical error variances. Error covariances are neglected here. Maximizing a simpler version of Eq. 6.8 with respect to f_i and another Lagrange multiplier introduced to enforce the normalization of the brightness yields a parameterized expression in λ_j (*Hysell and Chau, 2006a*):

$$f_i = F \frac{e^{-\sum_j \lambda_j h_{ij}}}{\sum_i e^{-\sum_j \lambda_j h_{ij}}} \quad (6.9)$$

Maximizing Eq. 6.8 with respect to λ_j yields $2M + 1$ non-linear equations given by:

$$g_j + e_j - \sum_i f_i h_{ij} = 0 \quad (6.10)$$

These equations are solved numerically for the $2M + 1$ Lagrange multipliers λ_j . Maximizing Eq. 6.8 with respect to e_j yields an expression relating the statistical fluctuations e_j to the Lagrange multipliers λ_j .

$$\lambda_j + \frac{2\Lambda}{\sigma_j^2} e_j = 0 \quad (6.11)$$

Finally, maximizing the functional with respect to Λ yields one more equation relating it to Σ , λ_j and σ_j^2 :

$$\Lambda^2 - \sum_j \frac{\lambda_j^2 \sigma_j^2}{4\Sigma} = 0 \quad (6.12)$$

6.3.2 In-beam radar images

Images are constructed from the spectral brightness distributions $f(\omega, \psi)$ for each range gate. Each spectral estimate is composed of four spectral bins. Colors are associated to each spectral bin. Green is used for the zero-frequency component, magenta for the Nyquist frequency component, and red and blue for the red- and blue-shifted components, respectively.

For each spectral bin, an image with the respective color associated with the bin is created. The intensity of the color in each pixel is proportional to the signal-to-noise ratio (SNR) of the spectral bin. The four images are added to produce the composite radar images presented in this paper. While pure color images indicate narrow spectral features, color combinations denote broad spectra. White color indicates flat (white) spectra. Conventional Range-Time-Intensity (RTI) maps can be formed by integrating the radar images over all frequencies and zenith angles. The angular coverage of the in-beam radar images is controlled by the radiation patterns of the transmitting and receiving antennas and by the dynamic range of the received echoes. For the São Luís radar, the field-of-view is approximately 16° wide. The angular field-of-view also limits the maximum horizontal scale-size of the waves that can be unambiguously observed.

6.4 Observations of October 25, 2005

Coherent backscatter radar observations were made almost every night during the SpreadFEx campaign from September 25 to November 8, 2005. The spread F season in Brazil starts around mid-September and lasts until the end of April (Sobral *et al.*, 2002; Abdu *et al.*, 2003). RTI maps and range-time maps of the vertical and zonal velocities could be produced for every observation night using measurements made with only a pair of antenna modules. However, a reduced number of observations could be used for the generation of in-beam radar images due to a technical problem with one of the receiver channels. Primary attention has been given to observations made during the period of 24-27 October, 2005, when good sky conditions for airglow measurements were found,

and preliminary results from a number of different observation instruments indicated the occurrence of spread F (Fritts *et al.*, 2007). Focus here is given to the night of October 25, 2005, when a strong bottom-type layer was detected and radar images could be generated. Bottom-type layers are not so frequently observed at São Luís as they are at Jicamarca. This is, at least in part, due to the lower sensitivity of the radar in Brazil.

Fig. 6.5 shows the RTI map for October 25. The RTI map shows that first detected echoes come from a thin scattering layer. The layer is approximately 35 km thick and starts around 250 km altitude. This thin layer was observed between 2145 UT and 2215 UT. The RTI map also shows that at least three fully developed radar plumes occurred later in the night. The first plume was observed around 2215 UT and reached about 500 km in altitude. A second plume was observed around 2330 UT and reached over 700 km. A third plume was observed around 0130 UT and also reached over 700 km. Echoes for this third plume were much weaker and indicate that small-scale waves responsible for radar echoes were decaying. RTI maps are ambiguous indicators of the space-and-time distribution of the scattering irregularities. This is due to the “slit camera” distortion effect, which is caused by the finite beamwidth of the radar antenna and the motion of the plasma across and along the radar field-of-view during the development of the radar plume. Structures with horizontal scale-sizes of tens of kilometers cannot be distinguished in the RTI maps, hence the necessity of interferometric techniques for radar studies of spread F .

Using the MaxEnt algorithm, in-beam images of the spread F event of October 25 were constructed. Fig. 6.6 shows a sequence of radar images between 2145 UT and 2155 UT, when a thin scattering layer is seen in the RTI map. The

radar images show that echoes actually come from a localized structure that emerged to the east (right) of the radar site and moved westward entering the radar field-of-view. The initial westward velocity of the structure was about 80 m/s and decreased as time passed. This westward moving scattering structure was located in the bottomside F region, probably in the valley region. Another sequence of images from the period between 2206 UT and 2208 UT is shown in Fig. 6.7. These images show a second scattering structure entering the field-of-view of the radar on the east side as the first structure moved to the west. Radar imaging shows that what seems to be a homogeneous scattering layer in the RTI map is actually highly structured in the horizontal direction. The fact that a scattering cluster is within the radar beam at any given time and the “slit camera” effect mentioned earlier cause these structures to appear as homogeneous layers in the RTI maps. Horizontal modulation of scattering layers in the bottomside F region was observed at other nights, but the organization of the scattering structures in the images was not as clear as in the case of October 25. A third sequence of images is shown in Fig. 6.8. This sequence shows images from the period between 2208 UT and 2216 UT. It shows that the scattering clusters continue to move, slowly now, in the westward direction. The images also show how scattering structures start to emerge at higher ranges. As the initial scattering clusters move westward, a vertically elongated scattering structure develops, reaching F peak altitudes. This scattering structure corresponds to the bottomside radar plume seen in the RTI map around 2215 UT created via GRT instability.

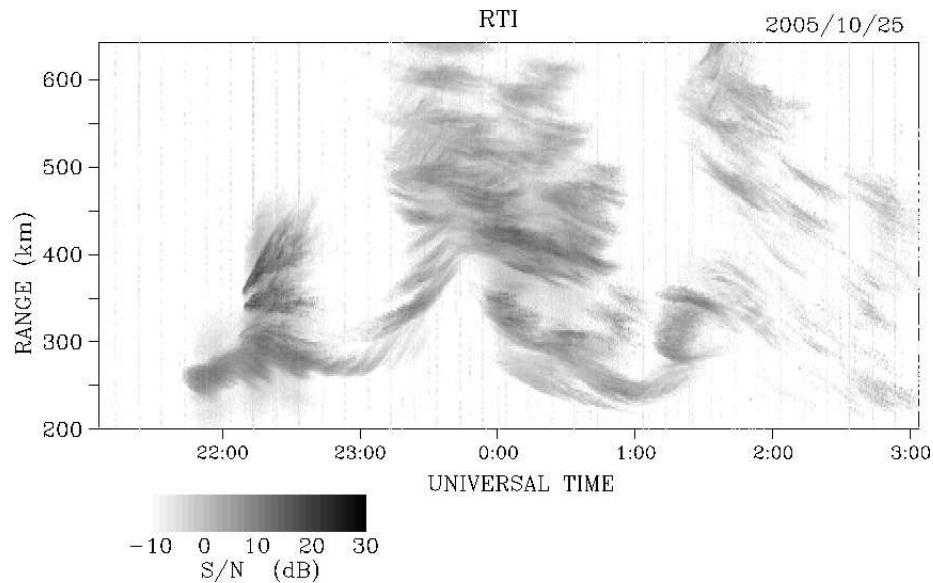


Figure 6.5: Range-Time-Intensity (RTI) map for the São Luís (30 MHz) radar observations made on October 25, 2005 (UT \approx LT+3)

6.5 Bottom-type layers

The characteristics of the layer shown in Fig. 6.6 match those of bottom-type scattering layers frequently observed by the Jicamarca radar in Peru during spread F season. Bottom-type layers are vertically narrow bands of scattering irregularities in the bottomside F region moving westward or slowly eastward (*Hysell and Burcham, 1998a*). These layers occur after sunset and do not develop vertically. They are precursors of radar plumes, which are signatures in the RTI maps of large-scale ionospheric plasma depletions generated via GRT instability.

A better understanding of the generation of bottom-type layers came from the development of an advanced observation mode at Jicamarca Observatory that combines incoherent and coherent backscatter radar measurements (*Kudeki*

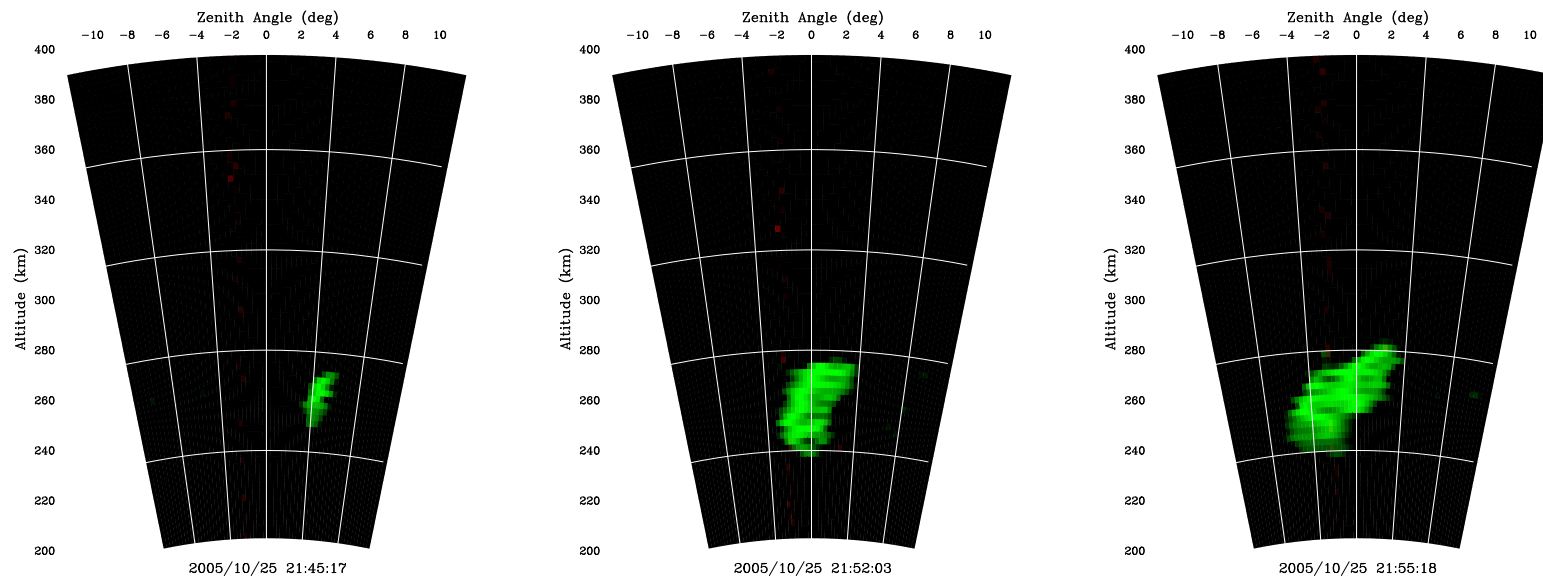


Figure 6.6: Sequence of in-beam radar images showing a bottom-type layer. The images shows that the layer is created to the East of the radar location and moves in westward direction entering the radar field-of-view.

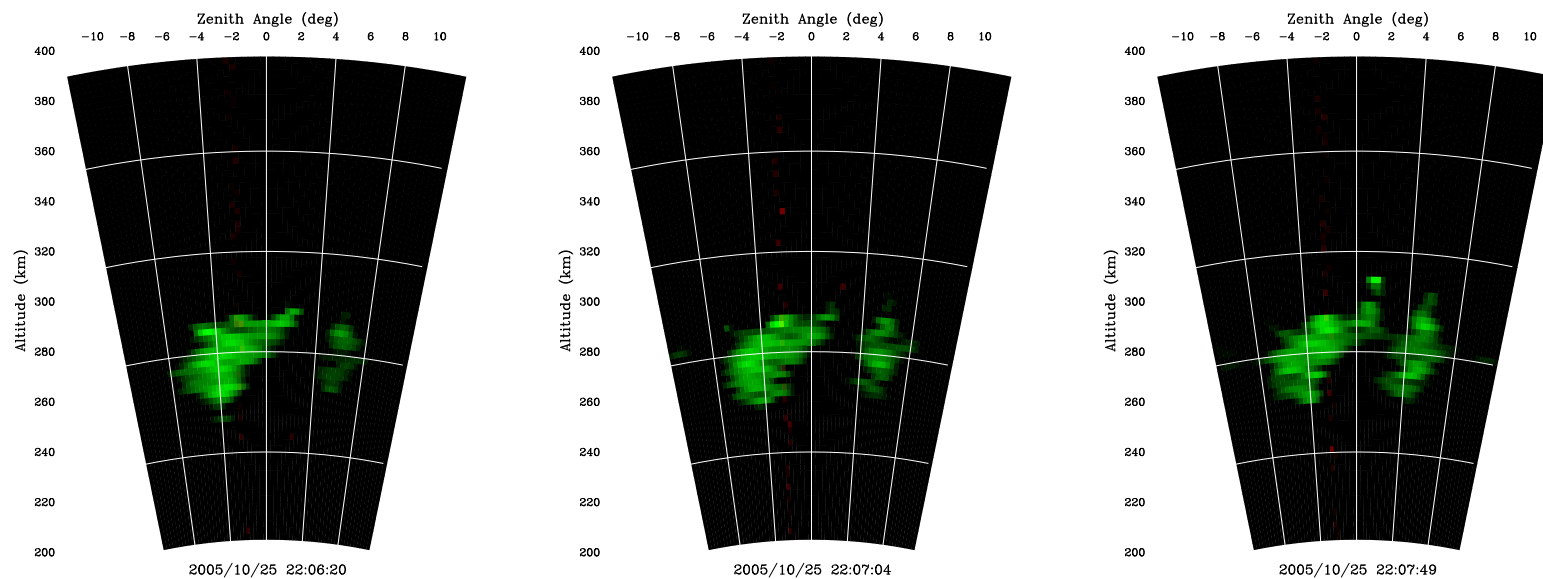


Figure 6.7: Sequence of in-beam radar images showing two clusters of scattering waves within the radar field-of-view.

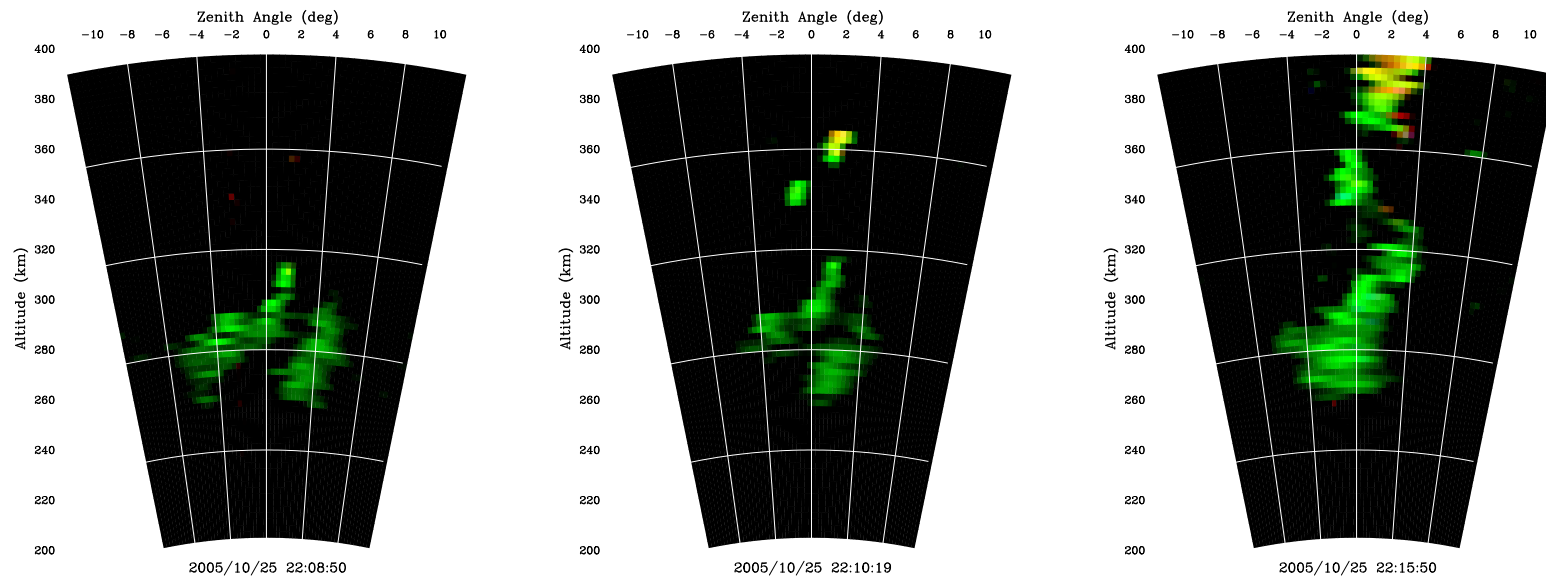


Figure 6.8: Sequence of in-beam radar images showing the development of a radar plume.

et al., 1999; *Kudeki and Bhattacharyya*, 1999). *Kudeki and Bhattacharyya* (1999) used this mode to observe the so-called post-sunset plasma vortex in the equatorial region. Their observations showed that the strata where the plasma motion is retrograde with respect to neutral wind and where bottom-type layers are located would be unstable to wind-driven gradient drift instabilities, given that horizontal density gradients are present. These gradients would be generated by defragmentation of the plasma vortex. Gradient drift instabilities can have growth rates for intermediate-scale waves much larger than the maximum predicted for the GRT instability for typical differential plasma-neutral flow speeds. Small-scale plasma waves responsible for radar scattering would be generated presumably by the primary waves via three-wave mode coupling (*Hysell et al.*, 2004a).

Observations also showed that the plasma vortex is stronger when the pre-reversal enhancements of the vertical plasma drift is larger, and this would also explain why bottom-type layers share the climatology of equatorial spread F (*Kudeki et al.*, 1999). Radar imaging observations contributed, showing that bottom-type layers are formed by kilometric structures with characteristics matching those expected for irregularities created by wind-driven gradient drift instability (*Hysell et al.*, 2004a). In-situ measurements of the vertical electric field measurements made by rockets confirmed the predominance of structures with vertical scale-sizes of a few km within bottom-type layers (*Hysell et al.*, 2006b). Due to the vertical resolution (2.5 km) of the measurements made with the São Luís radar, the primary kilometric waves within the bottom-type structure could not be distinguished in the images as they can be at Jicamarca.

6.6 Vertical shear of the zonal plasma flow

By looking at the zonal displacement of the scattering structure in the sequence of radar images of Fig. 6.6 one can notice the westward motion of the structure. It is also possible to see that irregularities at lower ranges move faster. The initial westward velocity at lower ranges was about 80 m/s. Because of the inconstant zonal velocity with altitude, the structure distorts and tilts to the east.

The westward motion of bottom-type layers is a feature that has been commonly observed at Jicamarca using interferometric techniques (e.g. *Kudeki et al.*, 1981). Bottom-type irregularities move with the background plasma and indicate the presence of a vertical shear in the zonal flow of the plasma at F region heights. The shear is formed by ionospheric plasma at F region peak heights moving in the eastward direction with the thermospheric wind, and bottom-side F region plasma moving in the westward direction (e.g. *Fejer*, 1981; *Tsunoda et al.*, 1981; *Haerendel et al.*, 1992).

Zonal drifts are altitude independent in the equatorial F region except during periods of fast drift variations and at times around the pre-reversal enhancement (*Fejer*, 1981). While first studies indicated the action of both E and F region dynamos as main drivers of the vertical shear (e.g., *Heelis et al.*, 1974), recent results have shown that other factors can be potentially important as well. These factors would include zonal electric fields on flux tubes with significant Hall conductivity, vertical winds, and vertical boundary currents forced from above or below the flux tube in question (*Haerendel et al.*, 1992; *Hysell et al.*, 2005a).

6.7 Structures in the bottom-type layer

The sequence of in-beam radar images in Fig. 6.6 illustrates interesting features that can be detected with the Brazilian radar. Initially, only one cluster of scatterers was observed in the radar images. As the cluster moves westward (to the left), another cluster enters the field-of-view of the radar. These horizontally spaced irregularity clusters suggest the presence of large-scale horizontal plasma waves in the bottomside F region. These waves would create regions with horizontal density gradients that are alternately stable and unstable to wind-driven gradient drift instabilities as illustrated in Fig. 6.9. The spacing length between scattering clusters (~ 35 km) would correspond to the wavelength of the large-scale wave.

The plasma wave responsible for modulating the bottom-type layer can also have served as the seed wave for the GRT instability leading to fully developed radar plumes. Fig. 6.8 shows a rare observation, where a sequence of radar images shows the full development of a radar plume that occurred within the radar field-of-view. The plume starts to develop in the region between and above the two bottom-type clusters. As the bottom-type clusters continue to move westward, the radar plume evolves vertically and starts to move slowly eastward. The radar images indicate that the two different and independent types of instability could be consequences of the same large-scale wave.

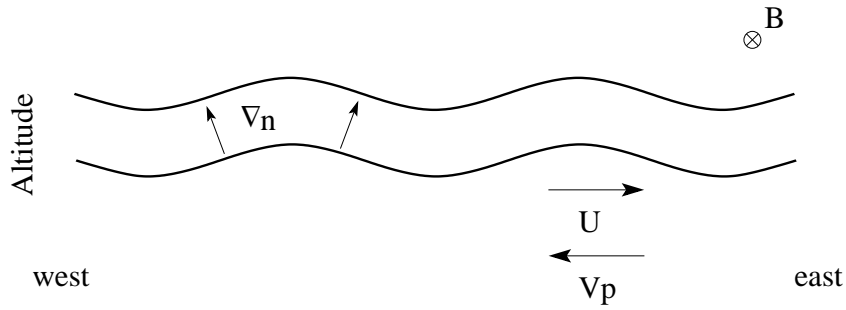


Figure 6.9: Diagram illustrating electron density perturbations caused by the large-scale waves and the geometry for the generation of the irregularity clusters. Regions where horizontal wind (U) is large in the plasma rest frame and parallel to a component of the density gradient (∇n) are gradient drift unstable.

6.8 Previous observations

The radar imaging observations at São Luís confirm the presence of deca-kilometric horizontal structures previously detected at Jicamarca. *Hysell et al.* (2004a) observed clusters of scattering irregularities horizontally spaced by approximately 30 km in bottom-type layers. The structures observed at Jicamarca were located around 330 km altitude, while the structures observed in São Luís were located around 270 km. This difference in altitude is within the height variability of the bottom-type layers. In both cases, the structures span about 40 km altitude and were moving westward. In the Jicamarca case, no tilt in the structures could be observed. The spacing between the clusters observed in São Luís is slightly larger than the spacing of the structures observed at Jicamarca. The short duration of the bottom-type layer on October 25 allowed the detection of only two clusters of scattering structures before the development of the radar plume. Scattering clusters have only been observed in Jicamarca radar images of bottom-type layers that preceded fully developed radar plumes. Horizontal

structures in bottom-type layers have not been observed at nights when spread F did not occur (Hysell *et al.*, 2004a). This suggests that monitoring such structures could provide a practical diagnostic for spread F forecasting.

ALTAIR (Advanced Research Project Agency (ARPA) Long Range Tracking and Identification Radar) is a VHF/UHF radar located at Kwajalein Atoll in the western Pacific. This radar is capable of performing coherent and incoherent scatter observations of the ionosphere and has been used sporadically for studies of the equatorial and low-latitude ionosphere. Examples of ALTAIR observations from the EQUIS II (Equatorial Ionospheric Study) campaign carried out in 2004 are shown in Fig. 6.10. The observations show that bottom-type layers, seen around 250 km altitude in the images, are not continuous but organized in clusters spaced by 30-50 km. Additionally, clusters of bottom-type layers spaced by 150-250 km were found in ALTAIR observations. The radar also showed that electron density undulations with similar scale-lengths (tens of km or 150-250 km) in the bottomside F region accompanied the scattering clusters.

6.9 On the origin of the bottom-type clusters

The measurements at São Luís are additional evidence of the presence of large-scale waves in the bottomside equatorial F region at the onset of spread F . These measurements, combined with other independent observations (Hysell *et al.*, 2004a, 2006b), indicate a correlative relationship between clusters of bottom-type scattering irregularities and the initiation of spread F . Hysell and Kudeki (2004b) investigated the possibility of shear flow to generate large-scale plasma waves in the bottomside equatorial ionosphere. They found a collisional branch

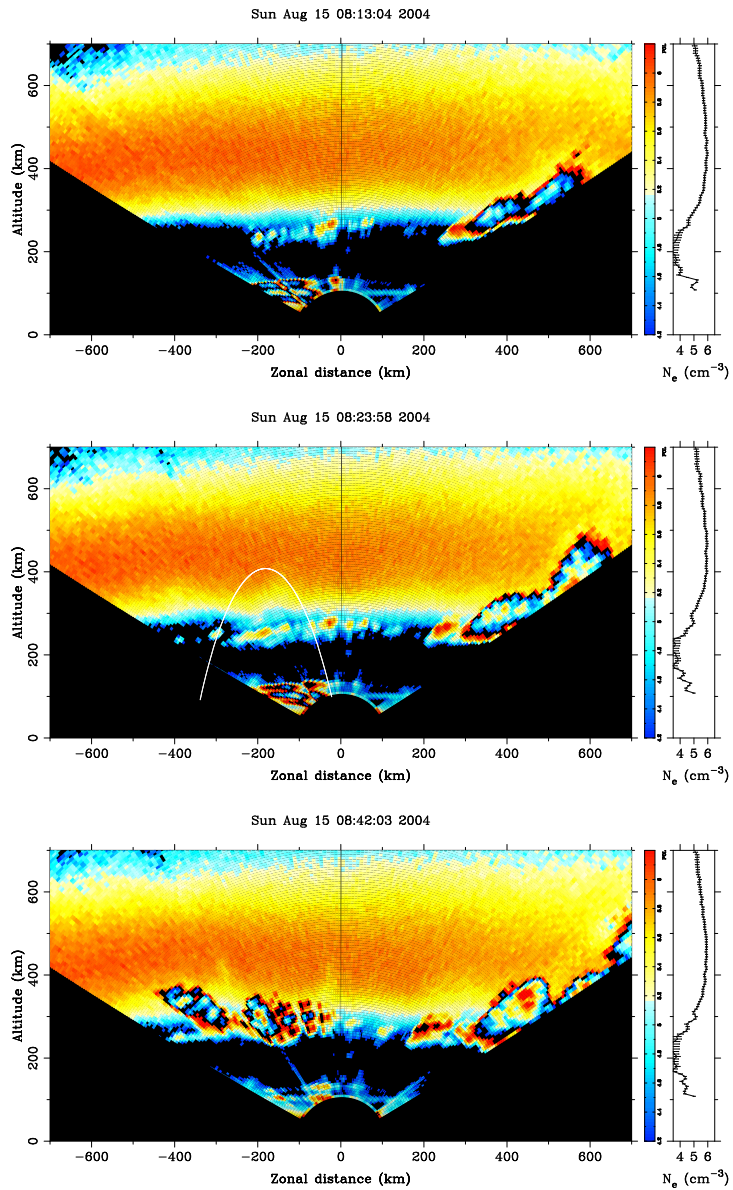


Figure 6.10: Altair radar scans prior to, during, and after a rocket launch on August 15, 2004 during the EQUIS II observation campaign. The white arc is the instrumented rocket trajectory. The rightmost panels depict electron density profiles at zenith. Times shown are UT (LT \approx UT + 11). After (Hysell *et al.*, 2005b). Reproduced by permission of American Geophysical Union.

of the electrostatic Kelvin-Helmholtz instability that could operate under typical conditions of the bottomside equatorial F region. The main destabilizing factor for this collisional shear instability is the retrograde motion of plasma with respect to the neutral wind, commonly observed in the bottomside equatorial F region.

Nonlocal boundary value analysis of the collisional shear instability reported by *Hysell and Kudeki (2004b)* predicted larger growth rates for wave modes with wavelengths (λ) in the order of $4\pi L$, where L is the length scale of the shear flow for a vertical profile of the zonal velocity $v(z)$ modelled as $v(z) = v_o(z) \tanh(z/L)$. Their results showed that the growth rate for these modes is comparable to growth rates of the collisional interchange instability in the equatorial F region under ideal conditions (4-5 e-foldings per hour). *Hysell and Kudeki (2004b)* also pointed out using a time-dependent numerical simulation of the shear instability that waves with shorter wavelengths of order L are observed in the initial stage of the instability development. The growth rate for these transient modes, however, was relatively long (~ 1 e-folding per hour). More recently, *Kudeki et al. (2007)* revisited the collisional shear instability with a nonlocal linear analysis. Their results showed larger growth rates for the $\lambda = L$ mode (18 e-foldings per hour), while the results for $\lambda = 4\pi L$ agreed with the results obtained in *Hysell and Kudeki (2004b)*.

The wavelengths ($\lambda \sim L$) predicted by the collisional shear instability would explain why periodic structures observed in the bottomside ionosphere preferably have scale lengths of a few tens of km. Electron density undulations with wavelengths of a few hundreds of km, often observed with the ALTAIR radar could also be explained in terms of the longer wavelength modes ($\lambda \sim 4\pi L$) with

slower growth rates. Another possibility is the action of 100-300 km gravity waves that may reach the lower F region (Vadas, 2007). The amplitudes of these waves and their impact in the ionospheric plasma is the subject of an ongoing theoretical study that is part of the SpreadFEx campaign.

The observations at São Luís suggest that the large-scale wave modulating the bottom-type layer on October 25 was created by the collisional shear instability. A strong vertical shear in the zonal velocity is implied by the westward motion of the layer at lower F region heights. This indicates the appropriate conditions for the collisional shear instability to develop. The spacing between the bottom-type structures is also in agreement with the scale lengths of fastest growing waves predicted by the instability theory (Hysell and Kudeki, 2004b; Kudeki *et al.*, 2007). The scale length also matches previous imaging radar observations made at Jicamarca (Hysell *et al.*, 2004a) and ALTAIR radar observations in Kwajalein (Hysell *et al.*, 2005b, 2006b).

6.10 Summary

In-beam radar images of F region scattering layers using interferometric observations made with the 30 MHz radar in Brazil were presented. The new set of antenna modules added to the system allows the study of spread F structures with resolution of a few kilometers. This paper focused on the analysis of a bottom-type layer detected on October 25 2005 during the SpreadFex campaign. Other interesting features observed in the scattering layers over São Luís will be discussed in future reports.

The finite width of the radar field-of-view makes the bottom-type irregulari-

ties appear as a continuous layer in the RTI maps. The interferometric radar images for October 25 confirmed the observations of *Hysell et al.* (2004a) showing that bottom-type layers are often formed by clusters of scattering irregularities. This indicates the presence of a large-scale plasma wave in the bottomside F region. The plasma wave modulates the bottomside F region, creating regions that are alternately unstable and stable to wind-driven gradient drift instabilities. The images also suggest that the same large-scale wave could have served as a seed wave for GRT instability, leading to a radar plume.

The observations made with the São Luís radar are additional experimental evidence of the presence of large-scale waves in the bottomside F region. While the possibility of gravity waves being responsible for the large-scale wave structure in the radar images cannot be ruled out, the strong shear in the zonal plasma flow and the scale length of the wave structure suggest its generation by the collisional shear instability (*Hysell and Kudeki, 2004b; Kudeki et al., 2007*). Also, periodic structures in bottom-type layers with similar scale lengths were previously observed at other equatorial sites (*Hysell et al., 2004a, 2006b*), suggesting a common and somewhat deterministic mechanism of generation.

Regardless of the origin of these waves, monitoring large-scale horizontal structures in the bottom-type scattering layers provides a useful diagnostic for the forecast of equatorial spread F . First attempts to track these structures using interferometric observations at Jicamarca have failed, mainly because of the narrow field-of-view of the antenna. The observations made in São Luís are encouraging. They indicate that these large-scale structures can be detected with small, low power radar systems. Similar systems could be easily deployed at other observation sites and be used for spread F forecast.

CHAPTER 7

CONCLUSIONS AND FUTURE WORK

This thesis covered different topics related to radar remote sensing of the equatorial F region. Here, a summary of the main results is presented and ideas for future studies are suggested.

7.1 IS RCS at small aspect angles

Recently, advances in the description of the IS spectrum at small aspect angles have been made. These new advances impact the estimation of plasma parameters from IS observations. They also impact the IS RCS calculation and consequently the conversion of backscattered power profiles to density profiles. Accurate density profiles are necessary to validate radio occultation measurements.

A study of the RCS at small aspect angles with application to Jicamarca oblique measurements was presented in Chapter 4. It was shown that magnetic field effects must be taken into account when computing the IS RCS for small aspect angles ($1^\circ < \alpha < 6^\circ$). This is the range of aspect angles of interest for oblique IS radar measurements at Jicamarca. When the magnetic field is taken into account, the RCS becomes a function of aspect angle and differs greatly from the RCS for a unmagnetized plasma. Electron Coulomb collisions, which are known to affect the shape of the IS spectrum, also affect the RCS at a lesser degree for aspect angles greater than 1° .

The approximation $\sigma_T = \frac{4\pi r_e^2}{1+T_e/T_i}$ that is commonly used at other radar sites cannot be applied to observations made at Jicamarca. Power profiles corrected

using the RCS that take into account both magnetic field and electron Coulomb collisions were compared with density profiles obtained simultaneously using the Faraday rotation technique. There is a good agreement between the two profiles, indicating the correctness of the computed RCS values. An approximate expression for the efficiency factor of a magnetized plasma was proposed. It can be used for a quick correction of power profiles measured during oblique IS radar experiments at Jicamarca. A full calculation of the IS spectrum including Coulomb collision effects is recommended if high accuracy is necessary.

7.2 The ion gyroresonance

The ion gyroresonance predicted by the IS theory was studied in Chapter 5. The results from *Woodman (2004)* and *Kudeki and Milla (2006)* allow the calculation of IS spectrum at small aspect angles taking ion-ion collisions into consideration and provide a forward model for inversion of plasma parameters from IS gyroresonance observations.

An experiment was designed for new measurements of the H^+ gyroresonance at Jicamarca. These observations were used in an attempt to obtain parameters from the topside ionosphere, which are scarce and difficult to obtain in the equatorial region. Observations with this experiment were made on October 9-10, 2006, and the H^+ gyroresonance was detected in the ionosphere above 600km during nighttime hours. Measurements can be made with reasonable accuracy, and plasma parameters ($T_e = T_i$ and fraction H^+) can be obtained by fitting theoretical to measured ACFs. The fitting routine takes into consideration IS theory for a magnetized and collisional (Coulomb) plasma. Ionospheric pa-

rameters obtained from fitting the ACFs are in relatively good agreement with predictions made by the IRI empirical model. The measurements and the reasonable values of the estimated parameters also support the validity of recent advances in IS theory.

Although, successful detection of the gyroresonance was possible, the results indicate difficulties in using this experiment as an operational mode for topside studies at Jicamarca. The sensitivity of this experiment is relatively low compared to the measurements made with a long uncoded pulse technique, for instance. Nevertheless, the detection of the gyroresonance can be considered a remarkable achievement given the level of clutter and the number of satellites/space debris that contaminate the measurements.

7.3 Large-scale waves at the onset of ESF

Results from new coherent scatter radar imaging observations made with a small radar in Brazil were presented in Chapter 6. The São Luís radar has been operating since 2001, but only recently has the radar imaging capability been added. In-beam radar images of F region scattering layers were analyzed. The images have coarser range and angular resolution than observations made at Jicamarca. These images, however, have a larger angular coverage than is currently possible at Jicamarca making them particularly suitable for studies of large-scale structures.

On October 25, 2005, a strong bottom-type layer was observed prior to the appearance of topside radar plumes. Radar images show that the bottom-type layer was not continuous but organized in clusters of scatterers in the horizontal

direction. The sequence of images also show that these clusters were, initially, drifting across the radar beam in the westward direction at a speed of about 80 m/s. This is an indication of the vertical shear in the zonal plasma flow, since the ionosphere moves in the eastward direction in the F region peak.

These observations are in agreement with other radar observations made at Jicamarca and ALTAIR. Similar scattering clusters were observed at the onset of spread F using radar imaging. Scanning radar observations made at ALTAIR also detected clusters of bottom-type layers and plasma undulations prior to radar plumes.

Assuming that bottom-type layers are formed by ionospheric irregularities generated by a wind-driven gradient drift instability, the clusters were interpreted as a result of a modulation caused by a plasma wave. These observations serve as additional evidence of the causal relationship between the clusters of irregularities and the initiation of fully developed spread F events. A possible explanation of the existence of these waves in the bottomside equatorial F region was given by *Hysell et al.* (2004a). They hypothesized that waves can be generated via a shear driven plasma instability. A strong shear in the zonal plasma flow in the equatorial region around sunset hours has been theoretically predicted and is commonly observed at Jicamarca.

The observations of October 25, 2005, reinforce a possible causal relationship between bottom-type scattering clusters and radar plumes. Monitoring these clusters could provide a useful diagnostic for spread F forecasts.

7.4 Future work

The following sections describe a number of research topics that merit further study.

7.4.1 Neutral temperatures and densities

In the F region, the rate of energy transferred from electrons to ions ($Q_{e,i}$) equals the energy transferred from the ions to the neutrals ($Q_{i,n}$). Information about the neutral atmosphere at thermospheric altitudes can be obtained from the ion energy equation (e.g. *Aponte, 1998*):

$$\begin{aligned} Q_{e,i} &= Q_{i,n} \\ 4.8 \times 10^{-7} N_e N_i \frac{T_e - T_i}{T_e^{3/2}} &= 1.2 \times 2.1 \times 10^{-15} N_i N_O \sqrt{T_i + T_n} (T_i - T_n) \end{aligned} \quad (7.1)$$

where, N_e , N_i , and N_O are the electron, ion, and atomic oxygen densities and T_e , T_i , T_n are the electron, ion, and neutral temperatures, respectively. *Pingree (1990)* and *Aponte (1998)* showed that is possible to estimate the neutral density and temperature given accurate IS radar measurements of electron and ion temperatures and electron density profiles. Their studies, however, involved double-pulse/Faraday IS measurements using the 6° position at Jicamarca to minimize errors in the estimation of electron and ion temperatures. The recent advances in IS theory (*Sulzer and González, 1999*) allow more accurate estimates of the temperatures using the on-axis position for which the sensitivity of the experiment is maximized. The results of our studies at small aspect angles can

be used to improve the accuracy of the electron density profiles. This motivates new studies of the neutral atmosphere at thermospheric heights using Jicamarca IS observations.

7.4.2 Bottom-type layers

Radar imaging observations of a unique spread F event on October 25, 2005 were presented in Chapter 6. This is the first published result of the radar imaging technique with observations from the São Luís radar in Brazil. It indicates that a small radar can be used for radar imaging studies of equatorial bottom-type layers. A follow-up study would include the analysis of other bottom-type layers observed by the radar. Unfortunately, layers with echoes strong enough for accurate radar imaging studies are not frequently observed. A special case to be investigated is the one where a bottom-type layer is detected but no plume is observed. In this case, it is predicted that the layer should be continuous across the radar beam. The search for such a layer is underway. The study of a number of cases could confirm the potential of small coherent scatter radars to be used for the detection of bottom-type scattering clusters and the causal relationship with bottomside or topside spread F .

Another possible follow-up study would include the analysis of images of radar plumes during the passage of the C/NOFS satellite at lower altitudes over São Luís in addition to observations planned for Jicamarca. The C/NOFS satellite has a 13° inclination orbit with a perigee of 375 km altitude and a number of sensors for in-situ plasma sounding. The generation of small-scale (meters) irregularities in spread F is not completely understood, and a combination of

satellite and radar observations could give useful information about the turbulent state of ionosphere.

7.4.3 Vertical drifts

The São Luís radar is also capable of detecting weaker echoes from the valley region around 150-km. These echoes are referred to as 150-km echoes and have been studied at Jicamarca for many years. Despite their existence being known about for several years, a full explanation for the existence of irregularities in that region remains to be found. The Doppler shift of these echoes, however, correspond to the vertical $\mathbf{E} \times \mathbf{B}$ drift at 150km altitude (*Kudeki and Fawcett, 1993; Chau and Woodman, 2004*). At Jicamarca, over 100 days of measurements are made every year of these echoes, and accurate vertical drifts are estimated from these measurements. Estimates of the vertical drifts from 150-km in Brazil could provide a unique source of accurate vertical drifts for studies of the longitudinal variation of the zonal electric field. We have analyzed a few days of measurements which indicate that the wide beams of the São Luís radar might cause errors in the vertical drift estimation. The Doppler velocity estimated from the spectra correspond to line-of-sight velocities, which in the case of a wide beam implies contributions from both the horizontal (zonal) and vertical components. These errors can be mitigated by using single baseline interferometry.

BIBLIOGRAPHY

- Aarons, J. (1982), Global morphology of ionospheric scintillations, *Proceedings of the IEEE*, 70(4), 360–378.
- Abdu, M. A., P. Muralikrishna, I. S. Batista, and J. H. A. Sobral (1991), Rocket observation of equatorial plasma bubbles over Natal, Brazil using a high-frequency capacitance probe, *J. Geophys. Res.*, 96(A5), 7,689–7,695.
- Abdu, M. A., J. H. A. Sobral, I. S. Batista, V. H. Rios, and C. Medina (1998), Equatorial spread F occurrence statistics in the American longitudes: Diurnal, seasonal and solar cycle variations, *Adv. Space Res.*, 22(6), 851–854.
- Abdu, M. A., J. R. Souza, I. S. Batista, and J. H. A. Sobral (2003), Equatorial spread F statistics and empirical representation for IRI: A regional model for the Brazilian longitude sector, *Adv. Space Res.*, 31, 703–716.
- Aponte, N. (1998), Radar studies of the equatorial F region energy balance, Ph.D. thesis, Cornell Univ., Ithaca, NY.
- Aponte, N., W. E. Swartz, and D. T. Farley (1999), Electron energy balance in the F region above Jicamarca, *J. Geophys. Res.*, 104(A5), 10,041–10,050.
- Aponte, N., M. P. Sulzer, and S. A. González (2001), Correction of the Jicamarca electron-ion temperature ratio problem: Verifying the effect of electron Coulomb collisions on the incoherent scatter spectrum, *J. Geophys. Res.*, 106, 24,785–24,794, doi:10.1029/2001JA000103.
- Aponte, N., M. P. Sulzer, M. J. Nicolls, R. Nikoukar, and S. A. Gonzalez (2007), Molecular ion composition measurements in the F1 region at Arecibo, *J. Geophys. Res.*, 112, A06,322, doi:10.1029/2006JA012028.

- Banks, P. M., and G. Kockarts (1973a), *Aeronomy: Part A*, Academic Press, New York.
- Banks, P. M., and G. Kockarts (1973b), *Aeronomy: Part B*, Academic Press, New York.
- Basu, S., E. MacKenzie, and S. Basu (1988), F region ionosphere: investigation at low latitudes, *Radio Sci.*, 23(3), 363–378.
- Bauer, P. (1975), Theory of waves incoherently scattered, *Phil. Trans. R. Soc. Lon.*, 280, 167–191.
- Baumjohann, W., and R. A. Treumann (1997), *Basic space plasma physics*, Imperial College Press, London.
- Bernstein, I. B. (1958), Waves in a Plasma in a Magnetic Field, *Phys. Rev.*, 109(1), 10–21.
- Beynon, W. J. G., and P. J. S. Williams (1978), Incoherent scatter of radio waves from the ionosphere, *Rep. Prog. Phys.*, 41, 909–955.
- Bilitza, D. (2001), International Reference Ionosphere 2000, *Radio Sci.*, 36(2), 261–275.
- Booker, H. G., and H. W. Wells (1938), Scattering of radio waves by the F region, *Terrs. Magn.*, 43, 249–256.
- Bourdeau, R. E., E. C. Whipple-Jr., J. L. Donley, and S. J. Bauer (1962), Experimental evidence for the presence of helium ions based on Explorer VIII satellite data, *J. Geophys. Res.*, 67, 467–475.
- Bowles, K. L. (1958), Observations of vertical incidence scatter from the ionosphere at 41 Mc/s, *Phys. Rev. Letters*, (1), 454–455.

- Carlson, H. C., and W. E. Gordon (1966), Radar Spectrographic Estimates of Ionic Composition from 225 to 1400 Kilometers for Solar Minimum Winter and Summer Conditions, *J. Geophys. Res.*, 71(23).
- Chau, J. L., and R. F. Woodman (2004), Daytime vertical and zonal velocities from 150-km echoes: Their relevance to F region dynamics, *Geophys. Res. Lett.*, 31, L17,801, doi:10.1029/2004GL020800.
- Chen, F. F. (1984), *Introduction to Plasma Physics and Controlled Fusion*, Plenum Press, New York and London.
- Christensen, A. B., et al. (2003), Initial observations with the Global Ultraviolet Imager (GUVI) in the NASA TIMED satellite mission, *J. Geophys. Res.*, 108(A12), doi:10.1029/2003JA009918.
- Davies, K. (1990), *Ionospheric Radio*, Peter Peregrinus LTD, London, UK.
- de Paula, E. R., and D. L. Hysell (2004a), The São Luís 30 MHz coherent scatter ionospheric radar: System description and results, *Radio Sci.*, 39, doi:10.1029/2003RS002914.
- de Paula, E. R., K. N. Iyer, D. L. Hysell, F. S. Rodrigues, E. A. Kherani, A. C. Jardim, L. F. Rezende, S. G. Dutra, and N. B. Trivedi (2004), Multi-technique investigations of storm-time ionospheric irregularities over the são luís equatorial station in brazil, *Ann. Geophys.*, 22, 3513–3522.
- Dougherty, J. P., and D. T. Farley (1963), A theory of incoherent scattering of radio waves by a plasma, 3, Scattering in a partly ionized gas, *J. Geophys. Res.*, 68, 5473–5486.
- Dougherty, J. P., and D. T. Farley (1960), A theory of incoherent scattering of radio waves by a plasma, *Proc. Roy. Soc.*, A259, 79–99.

- Dungey, J. W. (1956), Convective diffusion in the equatorial F region, *J. Atmos. Terr. Phys.*, 9, 304–310.
- Erickson, P. J., and W. E. Swartz (1994), Mid-Latitude Incoherent Scatter Observations of Helium and Hydrogen Ions, *Geophys. Res. Lett.*, 21(24), 2745–2748.
- Fabry, C. (1928), Remarques sur la diffusion de luminere et des ondes hertzienne par les electrons libres, *Compte Rend. Acad. Sci.*, pp. 187–777.
- Farley, D. T. (1959), A theory of electrostatic fields in a horizontally stratified ionosphere subject to a vertical magnetic field, *J. Geophys. Res.*, 64, 1225–1235.
- Farley, D. T. (1960), A theory of electrostatic fields in the ionosphere at nonpolar geomagnetic latitudes, *J. Geophys. Res.*, 65, 869–879.
- Farley, D. T. (1964), The effect of coulomb collisions on incoherent scattering of radio waves by a plasma, *J. Geophys. Res.*, 69, 197–200.
- Farley, D. T. (1966a), A theory of incoherent scattering of radio waves by a plasma, 4, The effect of unequal ion and electron temperatures, *J. Geophys. Res.*, 71, 4091–4098.
- Farley, D. T. (1966b), Ionospheric temperatures and composition measurements at the magnetic equator, *Ann. Geophys.*, 22, 448–453.
- Farley, D. T. (1967), Proton gyroresonance observed in incoherent scattering from the ionosphere, *Phys. Fluids*, 10(7), 1,584–1,586.
- Farley, D. T. (1969a), Incoherent scatter correlation function measurements, *Radio Sci.*, 4(10), 935–953.
- Farley, D. T. (1969b), Faraday rotation measurements using incoherent scatter, *Radio Sci.*, 4, 143–152.

- Farley, D. T. (1991), Early incoherent scatter observations at Jicamarca, *J. Atmos. Terr. Phys.*, 53(8), 665–675.
- Farley, D. T., and T. Hagfors (2005), Incoherent Scatter Radar: Theory and Practice, *Unpublished Notes*.
- Farley, D. T., and D. L. Hysell (1996), Radar measurements of very small aspect angles in the equatorial ionosphere, *J. Geophys. Res.*, 101(A3), 5,177–5,184.
- Farley, D. T., J. P. Dougherty, and D. W. Barron (1961), A theory of incoherent scattering of radio waves by a plasma, 2, Scattering in a magnetic field, *Proc. Roy. Soc. A.*, 263, 238–258.
- Farley, D. T., H. M. Ierkic, and B. G. Fejer (1981), Radar Interferometry: A new technique for studying plasma turbulence in the ionosphere, *J. Geophys. Res.*, 86, 1,467–1,472.
- Farley, D. T., E. Bonneli, B. G. Fejer, and M. F. Larsen (1986), The prereversal enhancement of the zonal electric field in the equatorial ionosphere, *J. Geophys. Res.*, 81, 13,723–13,728.
- Fejer, B. G. (1981), The equatorial ionospheric electric fields: A review, *J. of Atmos. and Terrest. Phys.*, 43(5), 377–386.
- Fejer, B. G. (1991), Low-latitude electrodynamic plasma drifts: A review, *J. Atmos. Terr. Phys.*, 53, 677–693.
- Fejer, B. G., E. R. de Paula, R. A. Heelis, and W. B. Hanson (1995), Global equatorial ionospheric vertical drifts measured by the AE-E satellite, *J. Geophys. Res.*, 100(A4), 5,769–5,776.

- Fejer, B. G., J. de Souza, A. S. Santos, and A. E. C. Pereira (2005), Climatology of F region zonal plasma drifts over Jicamarca, *J. Geophys. Res.*, *110*(A12310), doi:doi:10.1029/2005JA011324.
- Fejer, J. A. (1961), Scattering of radio waves by an ionized gas in thermal equilibrium in the presence of a uniform magnetic field, *Can. J. Phys.*, *39*(5), 716–740.
- Fritts, D. C., et al. (2007), The Spread F Experiment (SpreadFEx): Program overview and first results, *Earth, Planets and Space*, *submitted*.
- Gentile, L. C., W. J. Burke, and F. J. Rich (2006), A climatology of equatorial plasma bubbles from DMSP 19892004, *Radio Sci.*, *41*(RS5S21), doi:doi:10.1029/2005RS003340.
- Giraud, A., and M. Petit (1978), *Ionospheric techniques and phenomena*, D. Reidel Publishing Company, London.
- González, S. A., and M. P. Sulzer (1996), Detection of He⁺ layering in the topside ionosphere over Arecibo during equinox solar minimum conditions, *Geophys. Res. Lett.*, *23*(18), 2,509–2,512.
- Gordon, W. E. (1958), Incoherent scattering of radio waves by free electrons with applications to space exploration by radar, *Proc. IRE*, *46*, 1,824–1,829.
- Groves, K. M., et al. (1997), Equatorial scintillation and systems support, *Radio Sci.*, *32*(5), 2,047–2,064.
- Haerendel, G., and J. V. Eccles (1992), The role of the equatorial electrojet in the evening ionosphere, *J. Geophys. Res.*, *97*, 1,181–1,197.
- Haerendel, G., J. V. Eccles, and S. Cakir (1992), Theory for modeling the equato-

- rial evening ionosphere and the origin of the shear in horizontal plasma flow, *J. Geophys. Res.*, 97, 1,209–1,223.
- Hagfors, T. (1961), Density fluctuations of a plasma in a magnetic field with applications to the ionosphere, *J. Geophys. Res.*, 66.
- Hagfors, T., and R. A. Brockelman (1971), A theory of collision dominated electron density fluctuations in a plasma with applications to incoherent scattering, *Phys. Fluids*, 14.
- Hanson, W. B. (1962), Upper-atmosphere helium ions, *J. Geophys. Res.*, 67, 183–188.
- Hargreaves, J. K. (1995), *The Solar-Terrestrial Environment: An Introduction to Geospace*, Cambridge University Press, Cambridge.
- Heelis, R. A., P. C. Kendall, R. J. Moffet, D. W. Windle, and H. Rishbet (1974), Electrical coupling of the E and F regions and its effect on F region drifts and winds, *Planet. Space Sci.*, 22, 743–756.
- Heelis, R. A., W. B. Hanson, and G. J. Bailey (1990), Distributions of He⁺ at middle and equatorial latitudes during solar maximum, *J. Geophys. Res.*, 95(A7), 10,313–10,320.
- Hysell, D. L. (1992), On the hierarchy of processes contributing to equatorial spread F, Ph.D. thesis, Cornell Univ., Ithaca, NY.
- Hysell, D. L. (1996b), Radar imaging of equatorial F region irregularities with maximum entropy interferometry, *Radio Sci.*, 31(6), 1,567–1,578.
- Hysell, D. L. (2000a), Incoherent scatter experiments at Jicamarca using alternating codes, *Radio Sci.*, 35(6), 1,425–1,436, doi:10.1029/2000RS002368.

- Hysell, D. L., and J. D. Burcham (1998a), JULIA radar studies of equatorial spread F, *J. of Geophys. Res.*, *103*(A12), 29,155–29,167.
- Hysell, D. L., and J. L. Chau (2006a), Optimal aperture synthesis radar imaging, *Radio Sci.*, *41*, doi:10.1029/2005RS003383.
- Hysell, D. L., and D. T. Farley (1996b), Implications of the small aspect angles of equatorial spread F, *J. Geophys. Res.*, *101*(A3), 5,165–5,176.
- Hysell, D. L., and E. Kudeki (2004b), Collisional shear instability in the equatorial F region ionosphere, *J. of Geophys. Res.*, *109*, doi:10.1029/2004JA010636.
- Hysell, D. L., J. Chun, and J. L. Chau (2004a), Bottom-type scattering layers and equatorial spread F, *Ann. Geophys.*, *22*, 4,061–4,069.
- Hysell, D. L., E. Kudeki, and J. L. Chau (2005a), Possible ionospheric preconditioning by shear flow leading to equatorial spread F, *Ann. Geophys.*, *23*, 2,647–2,655.
- Hysell, D. L., M. F. Larsen, C. M. Swenson, A. Barjatya, , T. F. Wheeler, M. F. Sarango, R. F. Woodman, and J. L. Chau (2005b), Onset conditions for equatorial spread F determined during EQUIS II, *Geophys. Res. Letters*, *32*.
- Hysell, D. L., M. F. Larsen, C. M. Swenson, and T. F. Wheeler (2006c), Shear flow effects at the onset of equatorial spread F, *J. of Geophys. Res.*, *111*(A11317).
- Hysell, D. L., F. S. Rodrigues, J. L. Chau, and J. D. Huba (2008), Full profile incoherent scatter analysis at Jicamarca, *Ann. Geophys.*, *26*, 59–75.
- Hysell, D. L., et al. (2006b), Rocket and radar investigation of background electrodynamics and bottom-type scattering layers at the onset of equatorial spread F, *Ann. Geophys.*, *24*, 1,837–1,400.

- Jacobs, J. A. (1995), The Earth's magnetic field and reversals, *Endeavour*, 19(4), 166–171.
- Jahn, J. M., and J. LaBelle (1997), Rocket measurements of high-altitude spread F irregularities at the magnetic dip equator, *J. Geophys. Res.*, 103(A10), 23,427–23,442.
- Kelley, M. C. (1989), *The Earth's Ionosphere*, Academic Press, San Diego, Calif.
- Kelley, M. C., M. F. Larsen, C. Lahoz, and J. P. McClure (1981), Gravity wave initiation of equatorial spread F - A case study, *J. Geophys. Res.*, 86, 9,087–9,100.
- Kil, H., and R. A. Heelis (1998), Global distribution of density irregularities in the equatorial ionosphere, *J. Geophys. Res.*, 103(A1), 407–418.
- Kintner, P. M., and B. M. Ledvina (2005), The ionosphere, radio navigation, and global navigation satellite systems, *Adv. in Space Res.*, 35, 788–811.
- Kintner, P. M., H. Kil, T. L. Beach, and E. R. de Paula (2001), Fading timescales associated with GPS signals and potential consequences, *Radio Sci.*, 36, 731–744, doi:10.1029/1999RS002310.
- Kintner, P. M., B. M. Ldevina, and E. R. de Paula (2007), GPS and ionospheric scintillations, *Space Weather*, 5, doi:10.1029/2006SW000260.
- Klobuchar, J., P. Doherty, M. B. El-Arini, R. Lejeune, T. Dehel, E. de Paula, , and F.S.Rodrigues (2002), Ionospheric issues for a SBAS in the equatorial region, *Proceedings of the 2002 Ionospheric Effects Symposium*, pp. 152–162.
- Klobuchar, J. A. (1996), Ionospheric effects of GPS, in *Global Positioning System:*

- Theory and Applications*, edited by B.W. Spilker and J.J. Axelrad and P. Enge, Progress in Aeronautics and Astronautics, AIAA.
- Kudeki, E., and S. Bhattacharyya (1999), Postsunset vortex in equatorial F region plasma drifts and implications for bottomside Spread-F, *J. Geophys. Res.*, *28*, 28,163–28,170.
- Kudeki, E., and C. Fawcett (1993), High Resolution Observations of 150 km Echoes at Jicamarca, *Geophys. Res. Lett.*, *20*(18), 1,987–1,990.
- Kudeki, E., and M. Milla (2006), Incoherent scatter spectrum theory for modes propagating perpendicular to the geomagnetic field, *J. Geophys. Res.*, *111*, doi: 10.1029/2005JA011546.
- Kudeki, E., and F. Sürücü (1991), Radar interferometric imaging of field aligned plasma irregularities in the equatorial electrojet, *Geophys. Res. Lett.*, *18*(1), 41–44.
- Kudeki, E., B. G. Fejer, D. T. Farley, and H. M. Ierkić (1981), Interferometer studies of equatorial F region irregularities and drifts, *Geophys. Res. Letters*, *8*(4), 377–380.
- Kudeki, E., S. Bhattacharyya, and R. F. Woodman (1999), A new approach in incoherent scatter F region EB drift measurements at Jicamarca, *J. Geophys. Res.*, *28*, 28,145–28,162.
- Kudeki, E., A. Akguray, M. Milla, J. L. Chau, and D. L. Hysell (2007), Equatorial spread-F initiation: Post-sunset vortex, thermospheric winds, gravity waves, *J. Atmos. Solar-Terres. Phys.*, *69*(17–18), 2416–2427.
- Lei, J., et al. (2007), Comparison of COSMIC ionospheric measurements with

- ground-based observations and model predictions: Preliminary results, *J. Geophys. Res.*, 112(A07308), doi:doi:10.1029/2006JA012240.
- Luhmann, J. G. (1995), Ionospheres, in *Introduction to space physics*, edited by M. G. Kivelson and C. T. Russell, Cambridge University Press.
- Makela, J. J., and M. C. Kelley (2003), Field-aligned 777.4-nm composite airglow images of equatorial plasma depletions, *Geophys. Res. Lett.*, 30(8), doi:10.1029/2003GL017106.
- Maus, S., et al. (2005), The 10th generation international geomagnetic reference field, *Physics of The Earth and Planetary Interiors*, 151(3-4), 320–322.
- Mendillo, M., and J. Baumgardner (1982), Airglow Characteristics of Equatorial Plasma Depletions, *J. Geophys. Res.*, 87(A9), 7,641–7,652.
- Milla, M., and E. Kudeki (2006), F region electron density and Te/Ti measurements using incoherent scatter power data collected at ALTAIR, *Ann. Geophys.*, 24, 1,333–1,342.
- Nicolet, M. (1961), Helium, an important constituent in the lower exosphere, *J. Geophys. Res.*, 66(7), 2,263–2,264.
- Picone, J., A. Hedin, D. Drob, and A. Aikin (2002), NRLMSISE-00 empirical model of the atmosphere: Statistical comparisons and scientific issues, *J. Geophys. Res.*, 107(A12), doi:10.1029/2002JA009430.
- Pingree, J. E. (1990), Incoherent scatter measurements and inferred energy fluxes in the equatorial F region ionosphere, Ph.D. thesis, Cornell Univ., Ithaca, NY.
- Prakash, S. (1999), Production of electric field perturbations by gravity wave

- winds in the E region suitable for initiating equatorial spread F, *J. Geophys. Res.*, *104*, 10,051–10,070, doi:10.1029/1999JA900028.
- Press, W. H., S. A. Teukolsky, W. T. Vetterling, and B. P. Flannery (1992), *Numerical recipes in C*, Cambridge University Press, New York.
- Ratcliffe, J. A. (1959), *The magneto-ionic theory and its applications to the ionosphere*, Cambridge University Press, London.
- Retterer, J. M., D. T. Decker, W. S. Borer, R. E. D. Jr., and B. G. Fejer (2005), Assimilative modeling of the equatorial ionosphere for scintillation forecasting: Modeling with vertical drifts, *J. Geophys. Res.*, *110*(A11307), doi:doi:10.1029/2002JA009613.
- Rishbeth, H. (1971), Polarization fields produced by winds in the equatorial F region, *Planet. Space Sci.*, *19*, 357–369.
- Rishbeth, H., and O. K. Garriot (1969), *Introduction to ionospheric physics*, Academic Press, New York.
- Rodrigues, F. S., and D. L. Hysell (2005), Full-profile analysis of Jicamarca IS radar data, in *Proceedings of the 2005 Coupling, Energetics and Dynamics of Atmospheric Regions (CEDAR) Workshop*, Santa Fe, NM.
- Rodrigues, F. S., E. R. de Paula, M. A. Abdu, A. C. Jardim, K. N. Iyer, P. M. Kintner, and D. L. Hysell (2004b), Equatorial spread F irregularity characteristics over São Luís, Brazil, *Radio Sci.*, *39*, doi:10.1029/2002RS002826.
- Rodrigues, F. S., M. J. Nicolls, and D. L. Hysell (2007a), Improved electron density measurements at Jicamarca, *J. Geophys. Res.*, *112*(A11315), doi:10.1029/2007JA012598.

- Rodrigues, F. S., M. J. Nicolls, R. Woodman, D. L. Hysell, J. L. Chau, and S. A. González (2007b), Ion gyroresonance observations at Jicamarca revisited, *Geophys. Res. Lett.*, *34*(L13107), doi:10.1029/2007GL029680.
- Sahr, J. D., D. M. Gidner, C. Zhou, and F. D. Lind (2001), Passive VHF radar for ionospheric physics, *J. Atmos. Sol. Terr. Phys.*, *63*(2), 117–122.
- Salpeter, E. E. (1961), Plasma density fluctuations in a magnetic field, *Phys. Rev.*, *122*, 1663–1674.
- Schunk, R. W., and A. F. Nagy (2000), *Ionospheres: physics, plasma physics and chemistry*, Cambridge University Press, Cambridge, UK.
- Shume, E. B., D. L. Hysell, and J. L. Chau (2005), Electron density profiles in the equatorial E region ionosphere derived from a bistatic coherent scatter radar experiment in Perú, *Geophys. Res. Lett.*, *32*, doi:10.1029/2004GL021715.
- Sobral, J. H. A., M. A. Abdu, H. Takahashi, M. J. Taylor, E. R. de Paula, C. J. Zamlutti, M. G. de Aquino, and G. L. Borba (2002), Ionospheric plasma bubble climatology over Brazil based on 22 years (1977-1998) of 630nm airglow observations, *J. Atmos. Sol. Terr. Phys.*, *64*(12), 1,517–1,524.
- Sultan, P. J. (1996), Linear theory and modeling of the Rayleigh-Taylor instability leading to the occurrence of equatorial spread F, *J. Geophys. Res.*, *101*(A12), 26,875–26,892.
- Sulzer, M. P., and S. A. González (1999), The effect of electron Coulomb collisions on the incoherent scatter spectrum in the *F* region at Jicamarca, *J. Geophys. Res.*, *104*(A10), 22,535–22,551.
- Swartz, W. E., and D. T. Farley (1979), A theory of incoherent scattering of radio

- waves by a plasma, 5, The use of the Nyquist theorem in quasi-equilibrium situations, *J. Geophys. Res.*, 84(A5), 1930–1932.
- Thomson, J. J. (1906), *Conduction of electricity through gases*, Cambridge University Press, London, England.
- Tsunoda, R. T. (1980), Backscatter measurements of 11 cm equatorial spread F irregularities, *Geophys. Res. Lett.*, 7, 848–850.
- Tsunoda, R. T., R. C. Livingstone, and C. L. Rino (1981), Evidence of a velocity shear in bulk plasma motion associated with the post-sunset rise of the equatorial F layer, *Geophys. Res. Lett.*, 8, 807–810.
- Vadas, S. L. (2007), Horizontal and vertical propagation and dissipation of gravity waves in the thermosphere from lower atmospheric and thermospheric sources, *J. Geophys. Res.*, 112(A06305), doi:10.1029/2006JA011845.
- Vadas, S. L., and D. C. Fritts (2004), Thermospheric responses to gravity waves arising from mesoscale convective complexes, *J. Atmos. Sol. Terr. Phys.*, 66, 781–804.
- Venkatraman, S., R. A. Heelis, and D. L. Hysell (2005), Comparison of topside equatorial parameters derived from DMSP, Jicamarca, and Another Model of the Ionosphere (SAMI2), *J. Geophys. Res.*, 110, doi:10.1029/2004JA010613.
- Von Zahn, U., and W. Meyer (1987), Mesopause Temperatures in Polar Summer, *J. Geophys. Res.*, 94(D12), 14,647–14,651.
- Wang, C., G. Hajj, X. Pi, I. G. Rosen, and B. Wilson (2004), Development of the Global Assimilative Ionospheric Model, *Radio Sci.*, 39(RS1S06).

- Woodman, R. F. (1967), Incoherent scattering of electromagnetic waves by a plasma, Ph.D. thesis, Harvard University, Cambridge, Massachusetts.
- Woodman, R. F. (1971), Inclination of the geomagnetic field measured by an incoherent scatter technique, *J. of Geophys. Res.*, 76, 178–184.
- Woodman, R. F. (2004), On a proper electron collision frequency for a Fokker-Planck collision model with Jicamarca applications, *J. Atmos Solar-Terr. Phys.*, 66(17), 1521–1541.
- Woodman, R. F., and T. Hagfors (1969), Methods for the measurement of vertical ionospheric motions near the magnetic equator by incoherent scattering, *J. Geophys. Res.*, 74, 1205–1212.
- Woodman, R. F., and C. LaHoz (1976), Radar observations of F region equatorial irregularities, *J. of Geophys. Res.*, 81, 5447–5466.
- Yeh, K. C., and C. H. Liu (1982), Radio wave scintillations in the ionosphere, *Proceedings of the IEEE*, 70(4), 324–360.